

Development of a telescope detector for ^{90}Sr detection

Master's Thesis, 15.06.2022

Author:

JUNAID HUSSAIN

Supervisor:

DR. HEIKKI PENTTILÄ



UNIVERSITY OF JYVÄSKYLÄ
DEPARTMENT OF PHYSICS

© 2022 Junaid Hussain

Julkaisu on tekijänoikeussäännösten alainen. Teosta voi lukea ja tulostaa henkilökohtaista käyttöä varten. Käyttö kaupallisiin tarkoituksiin on kielletty. This publication is copyrighted. You may download, display and print it for Your own personal use. Commercial use is prohibited.

Abstract

Hussain, Junaid

Development of a telescope detector for ^{90}Sr detection

Master's Thesis

Department of Physics, University of Jyväskylä, 2022, 149 pages.

Nuclear catastrophes and accidents release harmful fission products containing long-lived (^{79}Se , ^{93}Zr , ^{99}Tc , ^{107}Pd , ^{126}Sn , ^{129}I , and ^{135}Cs) radioisotopes having half-life of hundreds of thousands or millions of years and short-lived (^{85}Kr , ^{90}Sr , ^{106}Ru , ^{134}Cs , ^{137}Cs , ^{147}Pm , ^{151}Sm , and ^{155}Eu). After a few years, ^{137}Cs and ^{90}Sr radioisotopes with a half-life of around 30 years dominate. These dominating radioisotopes are potentially harmful for living creatures. They affect DNA, brain tissues, and even stick with bones. To study the possible radiation damages, one need to prepare a sample which is an expensive, tedious and long awaited process.

As telescope detector system was proposed to solve this sample preparation problem. The thesis aims to develop and test a prototype $\Delta E - E$ type telescope detector system for ^{90}Sr . The detector system is based on the beta energy gating period to distinguish ^{90}Y decay from ^{90}Sr decay. The detector identifies beta particles via $\Delta E - E$ coincidences. The high energy of ^{90}Y beta particles are used to distinguish this decay from other radiations.

The detector system consists pre-cut plastic scintillator of types EJ-200 and EJ-212 of Eljen technology. Two prototypes containing ($85\text{ mm}\times 1\text{ mm} + 75\text{ mm}\times 10\text{ mm}$) and ($35\text{ mm}\times 1\text{ mm} + 25\text{ mm}\times 10\text{ mm}$) were developed, out of which smaller one gave better light collection efficiency. For light collection purposes, two silicon photomultipliers were used for each detector system. The performance of silicon photomultiplier was also critically analyzed by checking the performance parameters. SiPM is a new device used in spectroscopy and will be used more and more in the future.

Keywords: Radioisotopes, plastic scintillator, detector, silicon photomultiplier (SiPM), light collection, energy calibration, efficiency

Preface

I can never, adequately and properly, submit my thankful praises to the Ever All-Gracious, the Ever All-Merciful Allah for providing me Guidance, resources and all the help to accomplish this task, for which I could never imagine, plan and organize.

First of all, I would like to thank the department of physics, University of Jyväskylä, for providing me with an excellent opportunity to fulfill my dream of graduating from a prestigious university. I also greatly acknowledge the financial support the department offered in the form of a generous scholarship for the entire duration of my studies. Furthermore, I want to thank Professor Paul Greenlees and Professor Moore Iain for introducing me to the world of nuclear physics.

I would like to express my sincere gratitude my supervisor Dr. Heikki Penttilä for his guidance throughout my thesis journey and for providing me the opportunity to learn valuable skills through professional and research training. I thank him for his patience, countless meetings, thorough guidance, and full support throughout this learning journey.

I am grateful to my study advisor Dr. Tuomas Grahn for his guidance and support especially, during COVID-19 pandemic period. I would, indeed, remiss if I do not have special thanks and appreciation for my elder brother Dr. Jamshed Iqbal and for my bhabi Farah Naz for their guidance, support, and help during my stay here in Finland. You guys are truly a role models for me.

I would like to dedicate this thesis to my mother for her countless prayers, whom I missed a lot during these two years and to my wife Nabia Tabussum for her love, care, support, and motivation. In the end, I would like to thank my family, friends, and fellow colleagues for providing me immense support and cooperation for the completion of this task.

Jyväskylä June 15, 2022

Junaid Hussain

Contents

Abstract	3
Preface	5
List of Figures	11
List of Tables	17
1 Introduction	19
1.1 About Project and goals	20
1.2 Structure of thesis	21
2 Theoretical knowledge	23
3 Overview of scintillation material based detectors	27
3.1 Inorganic Scintillators	28
3.1.1 Scintillation mechanism of inorganic scintillators	29
3.2 Organic scintillators	31
3.2.1 Scintillation mechanism of organic scintillator	32
3.3 Plastic Scintillators	35
4 Interaction and scintillator response to different radiations	39
4.1 Heavy ions	39
4.2 Electrons	40
4.3 Photons	43
4.3.1 Photoelectric absorption	46
4.3.2 Compton scattering	46
4.3.3 Pair production	48
4.4 Neutrons	49
4.4.1 Thermal neutrons	51

5	Silicon Photomultipliers (SiPM)	53
5.1	P-N Junction	53
5.1.1	P-N Junction under reverse bias condition	54
5.1.2	Avalanche photodiode (APD)	55
5.1.3	Geiger-mode avalanche photodiode or SiPM mode	56
5.2	Structure of a SiPM	59
5.2.1	Equivalent electronic circuit	60
5.2.2	Pulse shape	62
5.3	Terms and performance parameters associated with SiPM	63
5.3.1	Breakdown voltage and overvoltage	63
5.3.2	Photosensitivity	65
5.3.3	Photon detection efficiency	66
5.3.4	Gain	70
5.3.5	Dynamic range and linearity	72
5.3.6	Noise	73
6	General characteristics of detectors	77
6.1	Sensitivity	77
6.2	Response time	77
6.3	Dead time	78
6.4	Pulse shape discrimination	78
6.5	Pulse height distribution	78
6.6	Energy resolution:	79
6.7	Detection efficiency	80
6.7.1	Impact of the radiation type	81
6.7.2	Impact of the detector material	81
6.7.3	Impact of the measurement geometry	83
7	Experimental, materials and methods	85
7.1	Goal of experimental development	85
7.2	Description of telescope detector	85
7.3	Material	88
7.3.1	Plastic scintillators	88
7.3.2	Silicon photomultipliers (SiPM's)	89
7.3.3	Radioactive sources	89

7.3.4	Collimators	90
7.3.5	Degraders	91
7.3.6	Boxes as light shield	91
7.3.7	Voltage Power Supply	92
7.3.8	Data Acquisition and LINUX system	93
7.4	Experimental detector setup	93
8	Development of the telescope detector	97
8.1	Prototype telescope detector	97
8.2	Light collection efficiency	99
8.2.1	Light collection efficiency of 75×10mm EJ-200 scintillator . . .	100
8.2.2	Light collection efficiency of the 25×10 mm EJ-200 scintillator	103
8.2.3	Light collection efficiency of the 85×1 mm EJ-212 ΔE scintillator	104
8.2.4	Light collection efficiency of the 35×1 mm EJ-212 ΔE scintillator	108
8.3	Conclusions from the light collection efficiencies	111
8.4	Telescope detector and its energy calibration	111
8.4.1	Energy calibration of the E detector	112
8.4.2	The energy calibration of the ΔE detector	117
8.5	Two dimensional spectra	121
8.5.1	Telescope efficiency	121
8.5.2	Gamma ray discrimination	125
9	Conclusions and Discussion	129
	References	130
A	First appendix	143
B	Second appendix	145
C	Third appendix	147
D	Fourth appendix	149

List of Figures

1	Figure showing the decay channels of ^{137}Cs . Edited from [14]	23
2	Decay scheme of ^{90}Sr	24
3	Decay scheme of ^{241}Am [16]	25
4	Decay scheme of ^{60}Co	26
5	Conduction and valence band of conductor, semiconductor, and insulator. [23]	30
6	Prompt and delayed scintillation mechanism due to absorption of incoming radiations. [24]	30
7	Delocalized π -electronic cloud in benzene ring [25]	32
8	Scintillation mechanism in organic scintillators. [26]	33
9	Absorption and emission spectra (Stokes shift) of organic scintillator [9]	35
10	Thermal polymerization method for plastic scintillators preparation [28]	36
11	Transfer of energy in plastic scintillators [18]	37
12	Proton and electron penetration range in a two mm aluminum sheet [32].	42
13	Range (mm) of different particles having different energies (MeV) in EJ-200 plastic scintillator [33].	43
14	Response of EJ-200 plastic scintillator to different particles having MeV energy. Adopted from [34].	44
15	Energy dependence of various γ -ray interaction processes in NaI (inorganic scintillator) [9]	45
16	Compton scattering with collision kinematics. Edited from [35].	47
17	Pair production [36].	49
18	Probability of three types of processes due to γ -ray interaction [9]	50
19	(a) p-n junction under no bias condition with barrier potential V_0 . (b) p-n junction under reverse bias having depletion width x_0 and increased barrier potential with a factor of V_b . Hence a total barrier potential is $V_0 + V_b$ [21].	54

20	(a) PN-Junction diode behaviour under different ranges of applied reverse bias voltage (b) Left side figure shows one sided flow of avalanche in APD due to only e^- participation in impact ionization. Right side figure shows the avalanche development in SiPM due to electrons and holes participation in impact ionization. Adopted from [40]	55
21	An internal 1D structure of an APD with electric field strength [41] .	56
22	Figure showing the internal structure of a single avalanche photodiode in 1D and electric field strength. Figure from [43]	57
23	Left: A SiPM contains of up to tens of thousands microcells (tiny SPAD's). Right: A simplified circuit schematics of the SensL SiPM, comprise of 12 microcells with separate quenching resistor and capacitive circuit. Edited from [46] [47]	58
24	6 mm SensL (Micro FJ-60035-TSV) SiPM standard output pulse shape without a capacitive circuit [48]	58
25	6 mm SensL (Micro FJ-60035-TSV) SiPM fast output pulse shape with a capacitive circuit [48]	58
26	Low level light pulse output in a SiPM. Retrived from [48]	59
27	The basic equivalent electronic circuit model of single photon avalanche diode along with a quenching resistor R_Q and a capacitor with capacitance C_D . [43]	61
28	Current output for different phases in a SiPM. Quenching resistor R_Q determine the value of peak current. The rise and the recovery time is dependent on effective capacitance C_D . [54]	62
29	I-V graph showing sudden current increase behaviour above breakdown voltage for different sized microcells. Edited from [49]	64
30	Temperature dependence of breakdown voltage (V) from room temperature ($20\text{ }^{\circ}C$) to liquid nitrogen temperature ($-196\text{ }^{\circ}C$) for J-series (J-60035, $6\times 6\text{ }mm^2$) SensL SiPM. [57]	65
31	A peltier element composed of several blocks of n and p-doped semiconductor material [64]	66
32	Figure illustrating active area, quenching resistor, trenches, and signal AI line	68
33	Photon detection efficiency versus wavelength graph of SensL MicroFC-350035-SMT SiPM for different overvoltages V_{ov} [48]	69

34	Photon detection efficiency versus bias voltage graph at 420 nm for 6 mm SensL MicroFJ-60035-TSV SiPM. Size of microcell is 35 μm [48]	69
35	Gain decreases with increase in temperature in Hamamatsu $1 \times 1 \text{ mm}^2$ SiPM with (50 μm microcell size) at constant bias voltage [77]	71
36	Comparison of temperature coefficients between a high voltage silicon photomultiplier and SensL SiPM [78]	71
37	Gain increases with increase in overvoltage and microcell size (20 μm , 35 μm , 50 μm , and 100 μm) [53]	72
38	The SiPM response for different microcells (1 mm, 3 mm, 6 mm). The response is liner for lower count of photon, or more incident photon with more microcells [48]	73
39	A relationship between incident power and photocurrent for 6 mm SiPM. The response is liner up to 70 % of SiPM range. [48]	73
40	1 mm SiPM's dark count rate (DCR) dependence on over-voltage [53]	74
41	Temperature dependence of dark count rate for 400 pixel SiPM at constant overvoltage (2.5 V). [81]	74
42	Detector resolution definition using FWHM. The value of FWHM is 2.35σ for a Gaussian shape peak with standard deviation σ [9]	79
43	Effect of detector resolution on the gamma ray spectrum of ^{137}Cs . HPGe represents a measurement with a semiconductor detector. Other spectra represent scintillation detectors with different resolution. Figure from [85].	80
44	The electron range dependence on its energy in CsI and in a typical polyvinyltoluene [87] based plastic scintillator	82
45	Schematic arrangement of the telescope detector. See text for details	86
46	SiPM arrangement with scintillators	87
47	Front and back side of SiPM with bias filter circuit schematics	89
48	α , β and γ radioactive sources from JYFL	90
49	The final version of radiation collimator	91
50	Voltage power supply used in this work	92
51	Data acquisition system	93
52	Other material used in this thesis	94
53	Schematic diagram of experimental setup	95

54	Real experimental setup (a): Detector setup in box, (b): Covering box for detector setup, (c): Oscilloscope to observe signal, (d): DAQ setup, (e): LINUX system with GRAIN software, (f): β Spectra on computer screen	95
55	Experimental setup in light shielded box	96
56	Final prototype detector setup. Left: SiPM attached on the back of the E detector. Right: Detector irradiated with radioactive source. Note that the ΔE SiPM is attached on the front face of the detector .	98
57	Measurements with EJ-200 (75 mm \times 10 mm) scintillator with α , β and γ sources. Here d is the distance between radioactive source and scintillator.	99
58	75 \times 10 mm scintillator experimental setup	100
59	Position sensitivity measurements using collimated β for EJ-200 (75 mm \times 10 mm)	101
60	Finding the light collection efficiency by the shape-fitting technique (by stretching the spectra on the top of each other). See text for details.	102
61	Light collection efficiency from 75 \times 10 mm E detector	104
62	Light collection efficiency from 25 \times 10 mm E detector	105
63	Comparison of pulse height from 25 mm and 75 mm diameter scintillator. The measurement positions have the same relative light collection efficiency of 65 % with respect to the 100 % in the middle of each detector.	106
64	Position sensitivity measurements using collimated β for EJ-212 (85 mm \times 1 mm)	107
65	Alpha and beta irradiations on the same spot in the 85 \times 1 mm ΔE scintillator	107
66	Light collection efficiency from 85 \times 1mm ΔE detector	108
67	Light collection efficiency from small 35 \times 1mm ΔE detector	109
68	Position sensitivity measurements using collimated β for EJ-212 35 mm \times 1 mm plastic scintillator	110
69	End point channel determination	113
70	Energy calibration with degraded beta spectrum	115
71	^{137}Cs γ energy spectra	116

72	The position of the Compton edges is determined as the energy where the slope of the edges falls below 75 % of the level of the Compton peak. The corresponding levels and the crossing point are identified. The channel uncertainty comes mostly from the adjustment of the Compton peak height level.	117
73	Energy calibration of the E detector using ^{60}Co and ^{137}Cs Compton edge positions. The origin (energy at channel 0 is zero) is included in the fit.	118
74	Energy calibration with degraded beta spectra and Compton edge . .	119
75	Fit of transmission peak positions.	119
76	Energy calibration of 35×1 mm ΔE detector with transmission peak position	120
77	Two-dimensional matrix of the beta telescope prototype. The source is $^{90}\text{Sr}/^{90}\text{Y}$ without any collimation and located at 5 mm from the detector.	122
78	ΔE energy from the matrix	123
79	Summed up energy of E and ΔE detectors with different thresholds set in the E detector. The graphs are in reality on top of each other in region above 500 keV. They have been slightly offset for clarity. . .	123
80	Two dimensional matrix of non-collimated ^{90}Sr source at 16 mm distance for 30 minutes irradiation.	124
81	Total beta energy spectra extracted from ΔE - E matrices in figure 77 and 80. The number of beta events with $E_{tot} > 700$ keV is shown.	125
82	Two dimensional matrix of ^{137}Cs source at 4 mm distance for 10 minutes. The red rectangular indicates the area of proper beta particle events. The blue line surrounds the area of events with $E_{tot} > 700$ keV.	126
83	Beta ΔE signal projected from ΔE - E matrix shown in figure 77 versus noise ΔE signal projected respectively from figure 82	127

List of Tables

1	Properties of some inorganic scintillators. [21]	29
2	Properties of some organic scintillators [21]	31
3	Technical details of (MicroFC - 60035) $6 \times mm^2$, $35 \mu m$ SiPM. Edited from [51, 52]	60
4	EJ-200 and EJ-212 plastic scintillators properties [34]	88
5	Used radioactive sources with their activity	90
6	The both spectrum and endpoint channels of the spectra shown in figure 69 and the corresponding calculated endpoint energies. See text for calculation and endpoint channel determination details.	113
7	The energies and positions of the Compton edges of ^{137}Cs and ^{60}Co .	116
8	Some of the primary fluor used in plastic scintillators [18]	143
9	Commonly used wavelength shifter in plastic scintillator [18]	144
10	Properties comparison between photomultiplier tube (PMT) and sili- con photomultiplier (SiPM) [96]	147

1 Introduction

Life is full of accidents, but a nuclear accident can seriously affect humans and the environment. Whether it is Chernobyl (Ukraine) disaster (1986) or the recent Fukushima (Japan) accident (2014), they result in the fallout of fission products and harmful radioisotopes. The extent of radioactivity fallout from the Chernobyl accident was about 12×10^{18} Bq. On the other hand, Fukushima accident gave fallout of 2.7 PBq [1] (mostly ^{137}Cs) that is $\sim 10\%$ of Chernobyl disaster. These released fission products consist of short-lived and long-lived radioisotopes with a months or years decay constant. For example, long-lived fission product isotopes ^{79}Se , ^{93}Zr , ^{99}Tc , ^{107}Pd , ^{126}Sn , ^{129}I , and ^{135}Cs usually have half-lives of hundreds of thousands or million years. On the other hand, radioisotopes like ^{85}Kr , ^{90}Sr , ^{106}Ra , ^{134}Cs , ^{137}Cs , ^{147}Pm , ^{151}Sm , and ^{155}Eu have at least a one-year half-life. Both the short-lived and long-lived radioisotopes decay with time, and after a few years, two isotopes, ^{137}Cs and ^{90}Sr , dominate. The other short-lived radioisotopes either decayed or the fission yield is significantly low as compared to ^{137}Cs and ^{90}Sr .

Both the ^{137}Cs and ^{90}Sr radioisotopes are biochemically active, have serious environmental effects[2] [3] and are potentially harmful for biological life. For example, ^{137}Cs is highly soluble in water, and ^{90}Sr damage the DNA structure [4], sticks in bones, tissues, and possibly in the neural system. To study the possible damage on the living creatures of Chernobyl area, the biologists prepare the sample for analysis. This sample preparation [5] is hectic and time consuming process as after the cutting of the biological sample they need to be put for three weeks. This enable the secular equilibrium of ^{90}Y with ^{90}Sr . The samples then analyzed by using different techniques[6] [7] [8] for ^{90}Sr activity.

After getting some energy from incident ionization radiations, any material excites its electrons from its ground state to a higher excited state. When electrons de-excite from a higher to a ground state, energy in the form of a photon is released. This mechanism is called scintillation. Scintillators produce a small amount of light, which is then amplified with the help of a photomultiplier tube (PMT) or silicon photomultiplier (SiPM) to get an electrical signal output [9]. Spinthariscopes were

the first scintillator based detector system used by William Crooks in 1903 [10]. The device was used to observe the α particle scintillation on the Zinc Sulphide (ZnS) through a microscope in darkness. In 1909, Geiger and Marsden also used this detector system to study α particle scattering [11]. In 1910, Rutherford's famous atomic nuclear discovery was also based on ZnS scintillator [12].

Over time, the scintillation observation through the naked eye was replaced by instruments based on gaseous ionization. In 1944, the use of the photomultiplier tube (PMT) in radiation detection entirely changed the scenario. Now, use of the silicon photomultiplier (SiPM) for detection setting new marks. Today, scintillation detectors are widely used in many fields, including nuclear, particle, environmental, medical, etc for the detection of charged particles (α , β), ionization radiations, X-rays etc. A scintillator detector system is usually composed of three components. The first one is a scintillator, which can be any material (gasses, inorganic crystal, organic molecules, glass, liquid, and plastic). In this thesis work, pre-cut EJ-200 and EJ-212 scintillators from Eljen technology were used. The extent of radiation detection and sensitivity depends entirely on the material used. The second component is a photodetector which can be either a photomultiplier tube (PMT) or silicon photomultiplier (SiPM). The third part of a detector system is electronic for the signal processing, and a DAQ (data acquisition) system used for counting and amplifying the signal [13].

The main goal of this thesis work was to develop a prototype detector capable of detecting environmental radioactivities i.e. ^{90}Sr and ^{137}Cs . In addition, the light collection efficiency of SiPM was also tested. There is a lot of study available on the detectors specifically designed for ^{90}Sr with photomultiplier tubes but a limited literature available on the use of silicon photomultiplier. The reason is that SiPM devices are newer ones, hence a limited study on their use for detector system is available.

1.1 About Project and goals

In this thesis work, a prototype ($\Delta E-E$) type telescope detector based on the plastic scintillator and silicon photomultiplier was built and tested. Using the "Beta energy gating" technique, one can distinguish ^{90}Y decays from other types of decay. This telescope type detector system will be based on two scintillators of different dimensions (size and thickness) connected back-to-back having SiPM's. To test the optimal geometry effect of the samples, position and angle measurements were analysed.

1.2 Structure of thesis

This thesis is divided into nine sections. The thesis starts with a brief introduction, followed by background knowledge in section 2. Section 3 will give an overview of the scintillation material-based detectors, including the plastic scintillator. In section 4, the interaction of different types of radiations with matter and the response of plastic scintillator to ^{90}Sr radiation was discussed. The basic construction, working, and parameter affecting the performance of a SiPM are discussed in section 5, followed by the general characteristic of the detector in section 6. The material and experimental setup is discussed in section 7, and section 8 provides the experimental development, light collection efficiencies of prototypes, energy calibration, and two dimensional spectra of detectors. Finally, the last section 9, conclude the discussion.

2 Theoretical knowledge

The two major environmental activities due to nuclear tests in 1945 - 1963 and nuclear accidents such as Chernobyl (1986) and Fukushima (2011), are ^{137}Cs and ^{90}Sr . Both are produced large quantities in fission, and have long enough half-life to remain in the environment for centuries. In the experimental work of this thesis, radioactive sources of these environmental radioactivities were used. In addition, standard radiation sources ^{241}Am and ^{60}Co were used in the measurements.

The decay scheme of ^{137}Cs is given in Figure 1. It decays mostly ($\sim 95\%$) by releasing a β^- into isomeric excited state of ^{137}Ba daughter nucleus and only 5% to the ground state of ^{137}Ba . The excited isomeric state ^{137m}Cs having a half life of 2.55 minutes, releases a 662 keV gamma to reach ground state level with 85% of the ^{137m}Cs decays. Probability of emitting gamma from 662 keV isomeric level is higher, since 662 keV level is populated "only" 95% causes to start with. In addition, about 9.6% probability of internal conversion. The emitted gamma with 662 keV energy is easily detectable as ^{137}Ba ground state is stable.

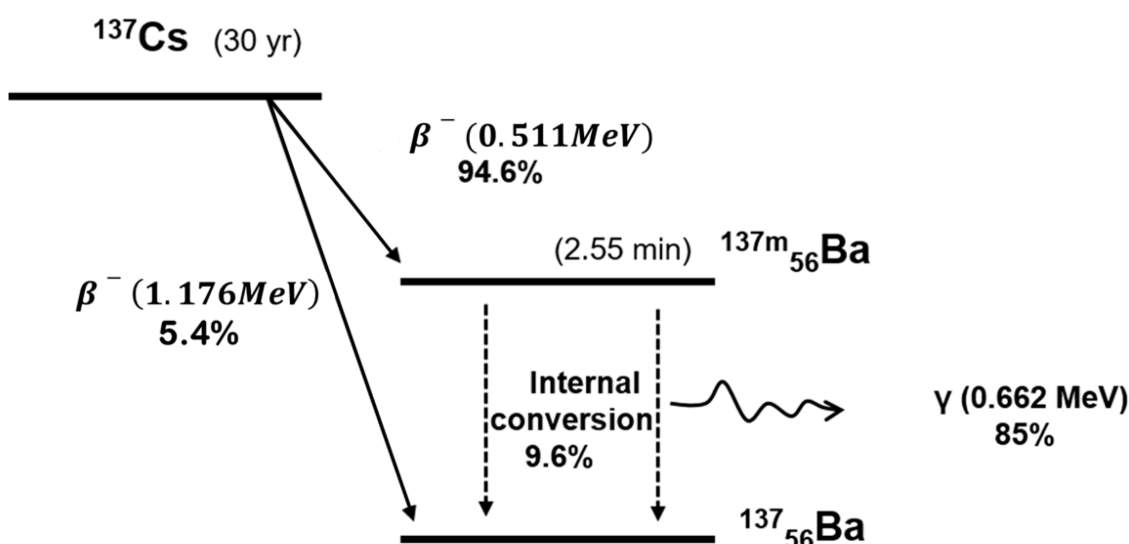


Figure 1. Figure showing the decay channels of ^{137}Cs . Edited from [14]

Figure 2 shows the decay scheme of ^{90}Sr . It is clear from the figure that ^{90}Sr is

a pure beta emitter. This is because ^{90}Sr emits a β from its nucleus and decays to ^{90}Y . This decay takes place between the ground states of ^{90}Sr and ^{90}Y . ^{90}Y further decays to ^{90}Zr by emitting β particles. Practically all ^{90}Y decays lead directly to the ground state of ^{90}Zr . There is a very minor (0.0115 %) branching to the excited state at 1761 keV, which decays via gamma emission to the ground state. The branch involving the gamma ray emission is however so small that for all practical purposes ^{90}Y can be considered as a pure beta emitter as well.

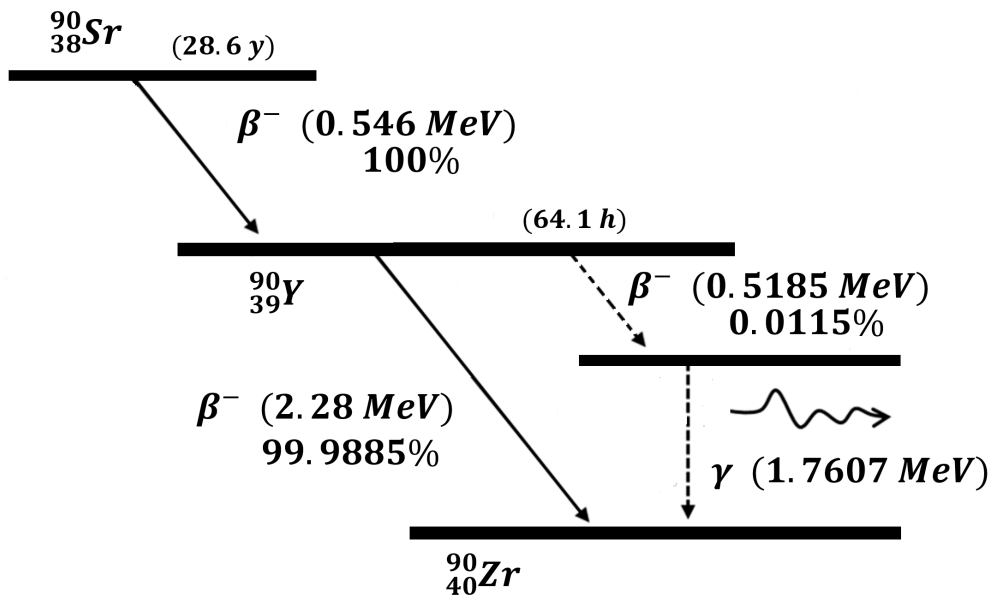


Figure 2. Decay scheme of ^{90}Sr

^{90}Sr have a similar biochemical structure as of calcium and replaces the calcium from bones. That is why it is also called "bone seeker". It enter in living organisms through contaminated water, milk and about 70 - 80 % amount is expelled through body as waste. The remaining radioactive ^{90}Sr sticks with bone, replaces bone marrow, and a little amount in blood and soft tissues. It mainly causes bone cancer, blood cancer, tissue cancer, and leukemia [15].

As mentioned, ^{90}Sr is a pure beta emitter. The daughter nucleus of ^{90}Sr , ^{90}Y , has a half-life of 64 h. The short half-life of ^{90}Y means it is in secular equilibrium with ^{90}Sr in practically any sample, if ^{90}Y is not somehow actively removed from the sample. Yttrium is not water soluble or very volatile, so it can be expected to stay in the sample. This is good for detection, since the geometry of the ^{90}Y beta particles extends to higher energy than most of the other environmental beta emitter.

If the beta decays from an environmental sample are studied with a beta telescope detector, consisting of a thin (plastic) ΔE -detector in front of thicker E-detector, the impact of background radiation can be reduced approving only coincident signals. Assuming a 1 mm thick ΔE -detector, a 1 MeV beta particle leaves about 190 keV in the ΔE -detector and the rest 870 keV in the E- detector. Simultaneous observation of the signals in both detectors is an indication of beta decay, and it will significantly reduce the environmental gamma ray background.

Finally, the decay of ^{90}Y can be distinguished on the basis of the total energy of the beta particle. The beta spectrum of ^{90}Y extends up to 2200 keV; the beta spectrum of ^{90}Sr ends at 546 keV. The beta spectrum of ^{137}Cs extends to 1175 keV but more than 95 % of the electron spectrum is below 660 keV. The beta endpoint of the main beta decay of ^{137}Cs is 510 keV. All in all, in a typical environmental sample containing $^{90}\text{Sr}/^{90}\text{Y}$ in secular equilibrium, all beta events with total energy higher than 700 keV can be assigned to the beta decay of ^{90}Y . That is why the technique can be called beta energy gating. More than 60 % of the ^{90}Y beta decay events have higher energy than 700 keV, which means high intrinsic efficiency for the detection.

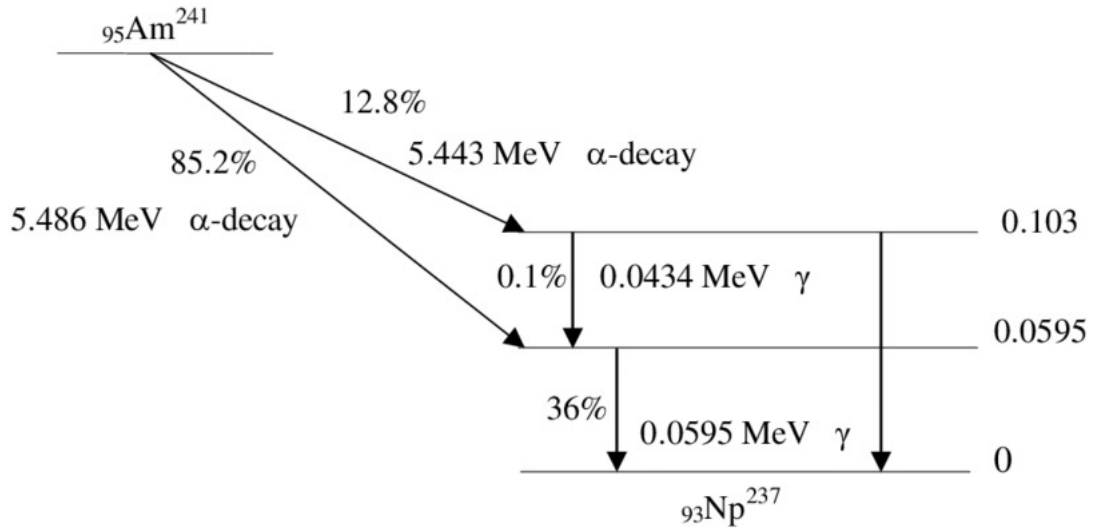


Figure 3. Decay scheme of ^{241}Am [16]

^{241}Am decays into daughter ^{237}Np , α -particles, and γ -rays with different energies. The one of decay equation of ^{241}Am is



It is clear from the figure 3 that ^{241}Am decay mostly via α -decay with 85% and 13% branching ratios having 5.486 MeV and 5.443 MeV energy respectively. In addition, there is also gamma ray branches with keV energies ranges i.e. 59.5489 keV, 26.4 keV, 17.8 keV, and 13.9 keV.

The ^{60}Co isotope has a half-life of 5.272 years and it decays mostly with beta $\approx 99.88\%$ having 0.31 MeV energy to excited state of $^{60*}\text{Ni}$. The other low probability beta branch ($\sim 0.12\%$) decay with 1.48 MeV. The excited states of $^{60*}\text{Ni}$ decays with gammas to ground state of ^{60}Ni with 1.732 MeV and 1.3325 MeV energy respectively, as illustrated in figure 4.

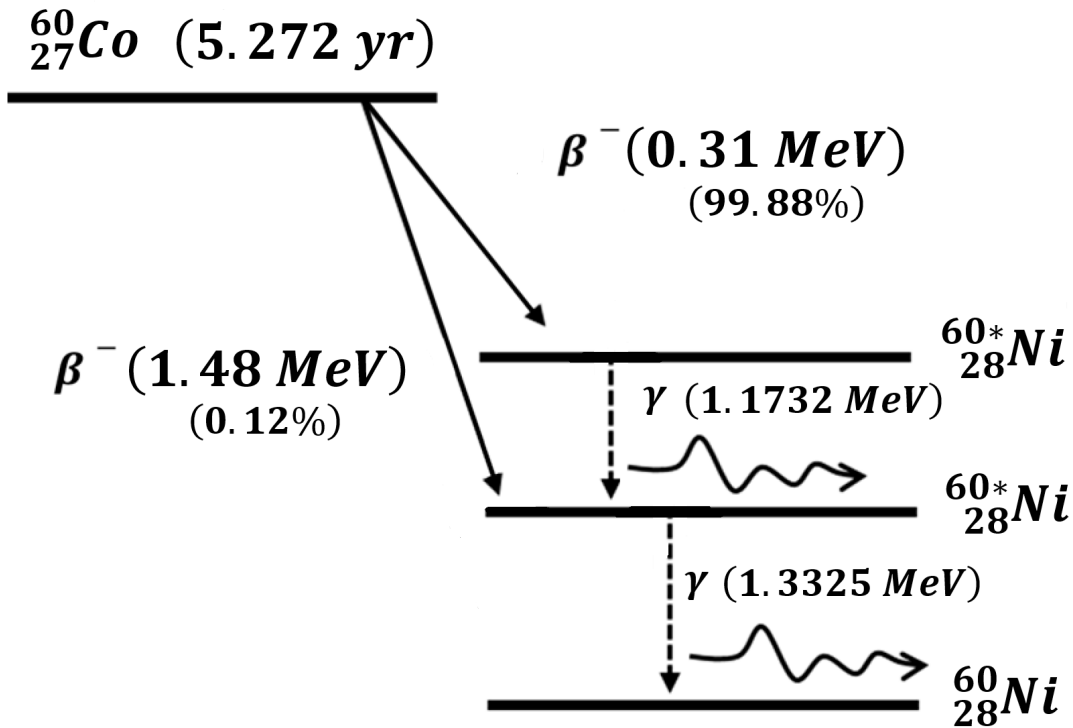


Figure 4. Decay scheme of ^{60}Co

3 Overview of scintillation material based detectors

In this section, a brief overview of scintillation materials used in the spectroscopy of ionising radiations is given. The section starts with the types of scintillation material and their use followed by a description of the properties of an ideal scintillator. In the first part of this section, inorganic scintillators and their scintillation mechanism are described. The second part deals with the organic scintillators and their scintillation mechanism. Finally, the chemistry (production method) and physics (energy transfer) of plastic scintillator used in this thesis has been discussed briefly.

There are two main types of scintillation materials: organic and inorganic. Scintillation detectors based on these materials have different chemical composition, production methods, scintillation mechanism, and operating limitations. Inorganic scintillators are typically crystals composed of elements having high atomic number Z . They have high density (3 - 8 g/cm^3), which help them effectively detect in particular γ -radiation, and short light attenuation length¹[17]. They are expensive, toxic, and the process of crystal growth is difficult. The organic scintillators are hydrocarbon composed elements having low atomic number (Z), low light output, low density (1 - 2 g/cm^3), long light attenuation length and affordable alternative to inorganic scintillators [18]. For β -spectroscopy and fast neutron detection, organic scintillators (due to high hydrogen content) give better results. However, inorganic scintillators are a preferred choice for γ -spectroscopy.

According to [9, 19, 20], an ideal scintillator should meet a few features listed below. A choice of scintillator material in practice is however a compromise, since there is no such scintillation material that could offer all the following desirable characteristics.

1. Show high conversion efficiency for converting incident energy into detectable photons. The suitable emission wavelength for photomultiplier tube (PMT) is

¹Attenuation length (or absorption length) is defined as the distance where the initial intensity of a beam of light or particles has dropped to $1/e$ (≈ 63 %)

near 400 nm and for photodiode/avalanche photodiode it must be near 600 nm. In addition, for a clear identification of full energy events, an ideal scintillator must have a good energy resolution.

2. Be transparent to the wavelengths of its own scintillation light. For this, the overlap between emission and optical absorption band gaps that causes self-absorption need to be minimal (see figure 9).
3. Demonstrate a linear relationship between deposited energy and light yield. Light yield is defined as the number of generated photons as a result of absorbed energy amount. A higher light yield value gives brighter emission which means a better detection performance.
4. Short decay time for fast signaling, reduced dead time and lower afterglow. For a good scintillator, the decay time must be < 10 ns and afterglow typically 0.1 % at 100 ms.
5. Refractive index ~ 1.5 to enhance coupling with photosensors i.e. photomultiplier tubes, silicon photomultipliers, etc. The best light transmission from the scintillator to the sensor is reached, when both have precisely same refractive index.
6. No damage due to chemical and radiation exposure. Some scintillator absorb atmospheric water and require a special packaging to avoid damage. Therefore, an ideal scintillator must also have hygroscopic hardness.

3.1 Inorganic Scintillators

Inorganic scintillators are also called ionic crystals. They are usually crystals of alkali-halides having a small impurity element called an activator. The most commonly used organic scintillators include NaI(Tl) and Cs(Tl). Impurity or activator is written in the brackets. Thallium (Tl) acts as an activator in the above inorganic scintillators. Activators are responsible for luminescence in crystals. They are used in small concentrations. For example in NaI(Tl), Tl concentration is 10^{-3} on a per mole basis [21]. CsF₂, CsI(Tl), CsI(Na), KI(Tl), and LiI(Eu) are other examples of inorganic scintillators [22]. Some inorganic scintillators are also based on non-alkali crystals. A few examples include $Bi_4Ge_3O_{12}$ (commercially known as BGO), BaF₂,

ZnS(As), ZnO(Ga), CaWO₄, and CdWO₄. The most important properties (i.e. wavelength of maximum emission, scintillation efficiency, decay time, and density) of some inorganic scintillators are given in table 1.

Table 1. Properties of some inorganic scintillators. [21]

Properties of Certain Inorganic Scintillators					
Material	Wavelength of Maximum Emission (nm)	Scintillation Efficiency (Relative, %)	Decay Time (μs)	Density (10^3 kg/m³)	
NaI(Tl)	410	100	0.23	3.67	
CaF ₂ (Eu)	435	50	0.94	3.18	
CsI(Na)	420	80	0.63	4.51	
CsI(Tl)	565	45	1.00	4.51	
Bi ₄ Ge ₃ O ₁₂	480	8	0.30	7.13	
CdWO ₄	530	20	0.90	7.90	
⁶ LiI(Eu)	470	30	0.94	3.49	

3.1.1 Scintillation mechanism of inorganic scintillators

The scintillation mechanism of inorganic scintillators is entirely based on the crystal lattice's intrinsic property. Electrons can only be found in discrete energy levels in solids. The lower band in which electrons are tightly bound to a particular atom is called the valence band. The higher band is called conduction band, having electrons free to move in a crystal lattice [9]. Figure 5 shows the conduction and valence bands of solids. Their relative location is different for insulators, semiconductors, and conductors. The intermediate energy region between valence and conduction bands without any allowed quantum states is called band gap or forbidden gap. There is no probability for an electron to be found at these energies. In a pure crystal, when an electron absorbs energy, it moves from the valence to the conduction band, leaving behind a hole. When the electron de-excites and returns to the valence band, it releases a photon by an inefficient process [9]. Inefficient in such a way that the emitted photon wavelength is much shorter than visible due to a high band-gap width (~ 8 eV).

These photons are difficult to detect by photosensors. Therefore, a small impurity of metal is added to the pure crystal to resolve this issue. This doped impurity is known as an activator. This doping aims to create an intermediate state in the crystal structure for an electron to reside. The added activators do not change the entire crystal structure but add a few sites for electrons. For example, in pure NaI crystal,

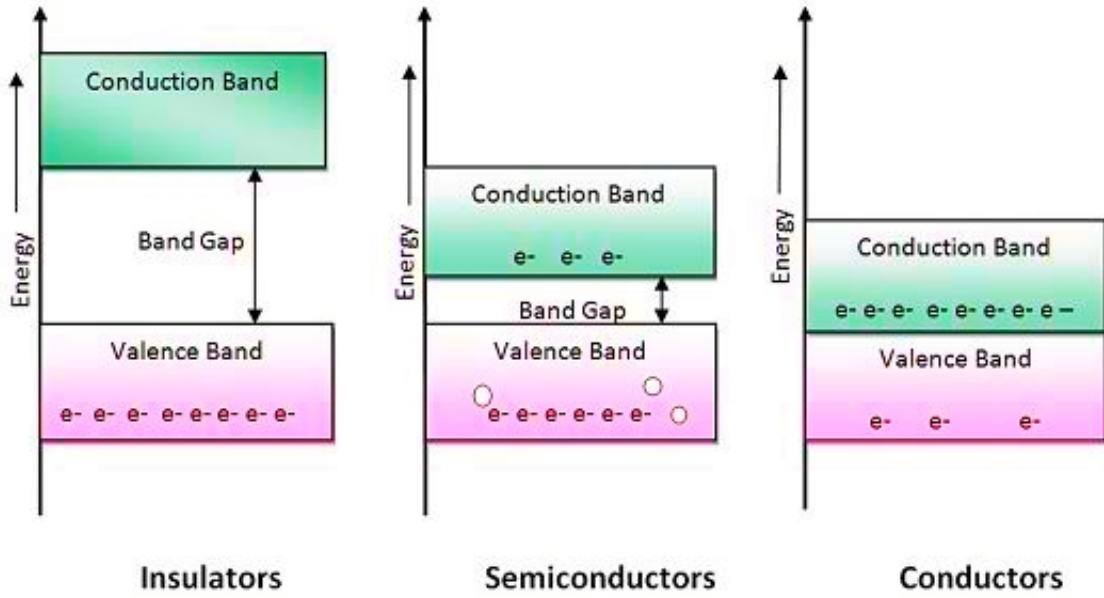


Figure 5. Conduction and valence band of conductor, semiconductor, and insulator. [23]

a trace amount of thallium is added as an activator. The scintillation mechanism of the inorganic scintillator is shown in figure 6. Incident radiations (having energy

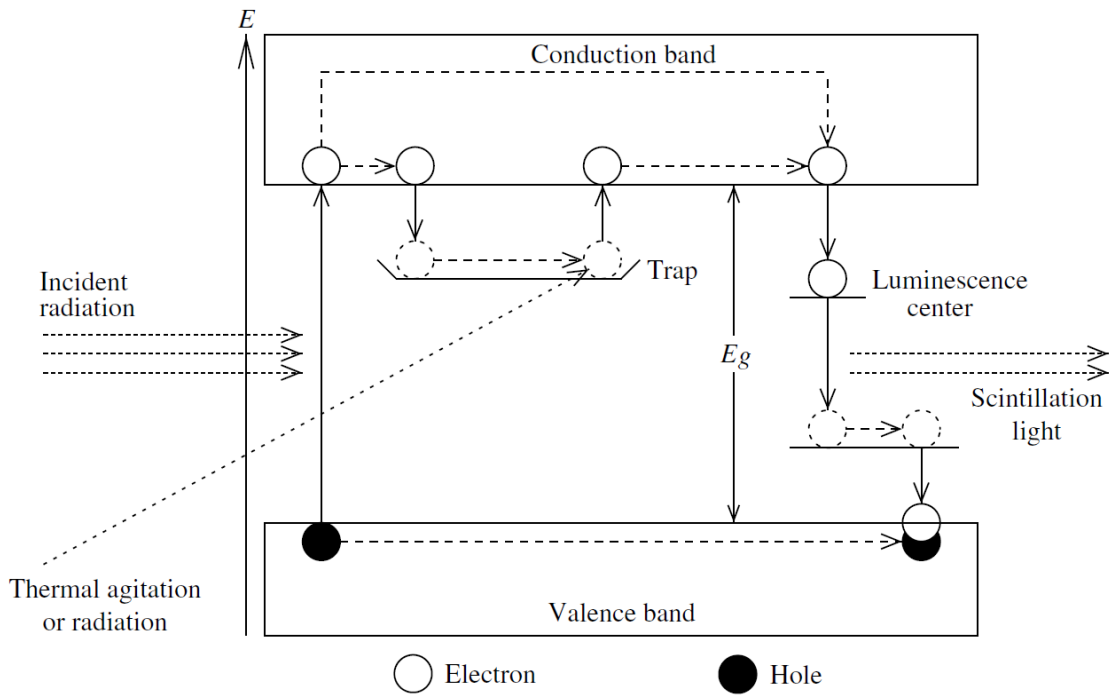


Figure 6. Prompt and delayed scintillation mechanism due to absorption of incoming radiations. [24]

greater than band gap energy) excite the electron, and it moves from the valence to the conduction band leaving behind a hole. When an electron is de-excited, it can quickly reside in these intermediate states (luminescence centers) before coming to the valence band. Intermediate state-assisted emitted photons lie in the visible region. These luminescent intermediate states typically have a half-life of 10^{-7} s. The half-life of the intermediate state decides the light output.

In addition, excited electrons sometimes can be trapped in a metastable energy state. These energy states are formed due to defects and impurities other than the dopant. The metastable state is quantum mechanically so different from the valence band that the electron transition directly to valence band is forbidden. Therefore, the electron stay in the trap state can last from a few nanosecond up to hours. Then, after gaining some energy (due to thermal excitation or other means), these trapped electrons excite back to the conduction band, from where they fall back to the valence band by releasing energy. The energy released in this way is named as phosphorescence or delayed scintillation [24].

3.2 Organic scintillators

Organic scintillators are widely used in radiation and particle detection, since they are easy to use and adapt to any geometry. They are composed by combining two or more aromatic hydrocarbon compounds. The higher concentration compound is

Table 2. Properties of some organic scintillators [21]

Properties of Certain Organic Scintillators				
Material	Wavelength of Maximum Emission (nm)	Relative Scintillation Efficiency (%)	Decay Time (ns)	Density (10^3 kg/m^3)
Anthracene	445	100	~30	1.25
<i>trans</i> -Stilbene	385	~60	4–8	1.16
NE 102	350–450	~65	2	1.06
NE 110	350–450	60	3	1.06
NE 213 (liquid)	350–450	~60	2	0.867
PILOT B	350–450	68	2	1.06
PILOT Y	350–450	64	~3	1.06

named as "solvent", and the smaller concentration one is referred to as "solute". The

solvent act as radiation absorber and solute act as scintillator as shown in figure 11.

Based on the number of compounds, scintillators are classified as unitary, binary, ternary, and so on. A unitary organic scintillator only consists of solvent, and a binary scintillator is composed of a solvent and a solute. Similarly, a ternary organic scintillator is synthesized using a solvent, a primary, and a secondary solute [21]. More solutes can be added to enhance the desired characteristics. Table 2 shows some important properties of the commonly used organic scintillators. Based on their composition, organic scintillators can be further divided into three categories: organic crystals, organic liquids, and plastic scintillators.

3.2.1 Scintillation mechanism of organic scintillator

Organic scintillators contain a benzene ring in their molecular structure. The benzene ring has a delocalized π -electronic cloud above and below the molecular orbital, as shown in figure 7.

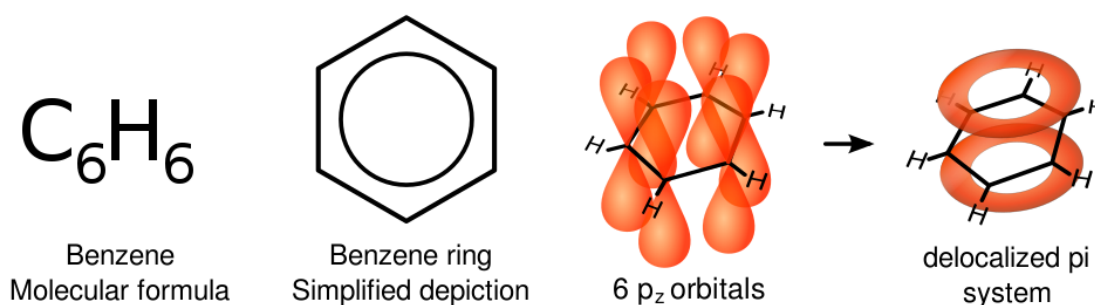


Figure 7. Delocalized π -electronic cloud in benzene ring [25]

The scintillation mechanism in an organic scintillator is based on the molecular transitions. A qualitative uncalibrated energy level diagram of an organic scintillator is expressed in figure 8. Note that for clarity, the energy level spacings are not in scale. The spacing between the S_0 and S_1 states is significantly greater (3 - 4 eV) as compared with the spacing between S_1 and S_2 or S_2 and S_3 (~ 0.16 eV). The spacing may vary slightly depending on the aromatic compound used. Singlet states have vibrational substates denoted as S_{00} , S_{01} , S_{02} , S_{03} , and so on for S_0 state, as S_{10} , S_{11} , S_{12} , S_{13} ... for S_1 state, and so on. The first suffix represent the sub-level. S_{00} is the lowest vibrational state and at room temperature, all the electrons reside in this state of molecule [9]. Electrons excite by absorbing the energy of incident ionising radiation. The de-excitation of an electron in organic molecule can produce

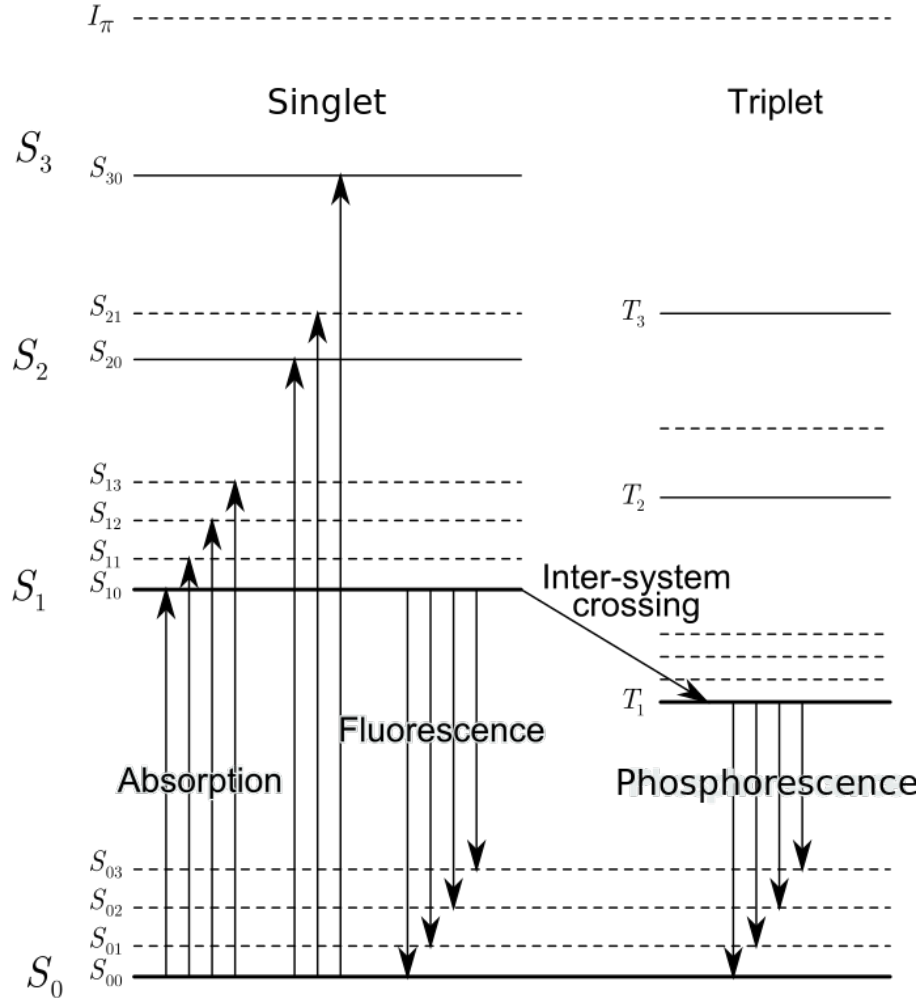


Figure 8. Scintillation mechanism in organic scintillators. [26]

three types of luminescence known as fluorescence, phosphorescence, and delayed fluorescence [26].

Fluorescence: The absorption of incident energy allows electrons to occupy higher (singlet) vibrational states S_1 , S_2 , S_3 . For a molecule, it usually takes $\sim 10^{-12}$ s to reach thermal equilibrium before emission from S_{10} state. The radiative lifetime of S_1 is $\sim 10^{-8}$ s - 10^{-9} s. Vibrational state transition to ground state is a favourable one with release of ultraviolet or visible fluorescent photons [9]. The equation 2 represent the fluorescence emission intensity at a certain time t.

$$I = I_0 e^{-t/\tau} \quad (2)$$

where

I = intensity at time t

I_0 = intensity at $t = 0$

τ = fluorescence mean decay time

Phosphorescence: There exist another scenario in which excited singlet state S_1 first decays to triplet state T_1 through an intersystem crossing. The de-excitation from T_1 to S_0 occur slowly ($\sim 10^{-4}$ s) by emitting longer wavelength than that of fluorescence. This process is called phosphorescence [9].

Delayed fluorescence: The third possibility is delayed fluorescence. The higher triplet states quickly de-excite through a non-radiative emission to a lower level triplet state. The de-excitation of excited triplet state is strongly forbidden and give rise to the long live phosphorescence. Furthermore, due to higher stability of triplet state as compared to singlet state, electron transition take more time to occur ($\sim 10^{-4}$ s). The spectrum of delayed fluorescence is somewhat similar to phosphorescence, but with a longer decay time and does not obey exponential decay. Some molecules from S_1 single excited state transition to T_1 triplet state, through a process called inter-system crossing. From here it de-excite to ground state. This phenomena causes delayed fluorescence [9].

Figure 8 can be used to illustrate why the organic scintillator is transparent to its own fluorescence emission spectrum. Absorbed photon energy, corresponding to length of upward arrows in figure 8, is almost always greater than that of fluorescence transitions corresponding to the length of the arrows pointing downwards. The scintillator emission spectrum is thus separated from its optical absorption spectrum. This separation is known as Stokes shift. The transition between S_{10} and S_{00} states however have same energy in both directions. This produces a small overlap between the emission and optical absorption spectra, introducing some self-absorption. Since fluorescence decay to the vibrational substates of S_0 singlet state is favoured, the overlap is typically insignificant. In general, a high value of Stokes shift results lower probability of scintillation light absorption i.e. smaller value of overlap area. In radiation detection, Stokes shift is used as a tool to measure the scintillator appropriateness [24].

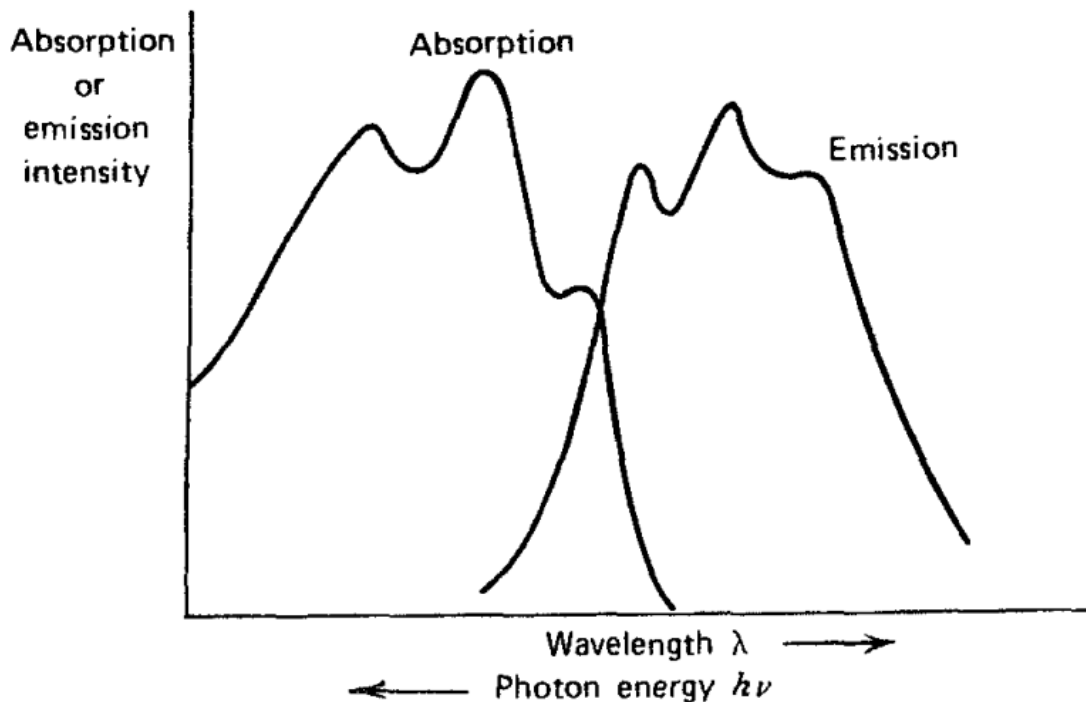


Figure 9. Absorption and emission spectra (Stokes shift) of organic scintillator [9]

3.3 Plastic Scintillators

In this thesis work, Eljen technology's **plastic scintillators** of different dimensions were used. The technical detail of used scintillator is given in table 3. The properties of plastic scintillators are very similar to those of liquid organic scintillators. That is why they are also called solid solutions of organic scintillators. The plastic scintillators do not however need any container. Furthermore, they are inert to water, air and many chemicals. Therefore, they are easier to use in practice than the liquid scintillators. In addition, plastic scintillators are inexpensive, durable, easy to manufacture, have high optical transmission, fast rise and decay time [27]. They are commercially available in different sizes and shapes (cylindrical, rods, flat sheets, etc.). Due to their lower production cost, they find applications in nuclear physics, medical imaging, ionization radiation detection, environmental purposes, and particle identification [9]. They can detect X-rays, ionization radiations, fast neutrons, and charged particles.

The thermal polymerization method is a commonly used preparation method for plastic scintillators as elaborated in figure 10. Plastic scintillator consists of a polymer

base usually vinyltoluene or styrene solvent and one or more solutes [18]. These solutes are also called "fluor". Some of the most commonly used monomer solvents are polystyrene, polyvinyl toluene (PVT), and polyphenylbenzene. Typical solute include P-Terphenyl and PPO (2,5-diphenyloxazole) [22]. The chemical composition with formulas of primary and secondary solutes are shown in table 8 in appendix B.

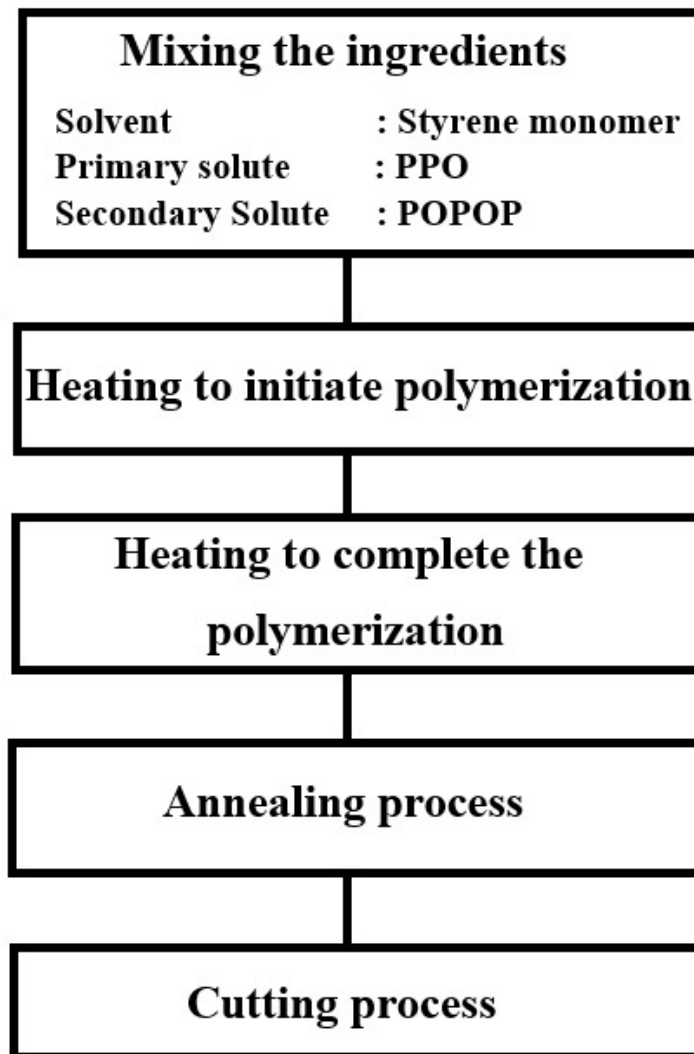


Figure 10. Thermal polymerization method for plastic scintillators preparation [28]

Secondary solute is usually added as wavelength shifter to enhance or to achieve desirable scintillation and optical properties. Composition variation leads to changes in characteristics like optical properties (absorption, transmission, emission), radiation resistance, fast rise, and decay time. For example, a small proportion of solvent

named as POPOP (1,4 - bis benzene) can be added to enhance wavelength shifting properties [22]. However, only 1 % fluor concentration is added to scintillators. The second fluor concentration is typically 0.01 %. Some of the commonly used wavelength shifter in plastic scintillators are given in table 9 in appendix B.

As plastic scintillators are a type of organic scintillators. Therefore, scintillation mechanism is same as of organic scintillator, discussed in section 3.2.1. Figure 11 illustrates the incident energy transfer in the plastic scintillator. Energy transfer from incident radiation excites the molecule. Energy is then transferred from polymer base to primary fluor through a non-radiative process called the Förster mechanism. In this mechanism, energy transfer is due to dipole-dipole interaction between donor and acceptor molecule distance appared by 3 - 6nm [29]. Energy from primary fluor is released in the ultra-violet (UV) region through fluorescence. As photomultipliers are incapable of working in UV region, therefore, a wavelength shifter needs to be added to plastic scintillators. These wavelength shifters absorb the emitted UV energy and convert it into a visible range, which is easily more detectable by silicon photomultipliers (SiPM).

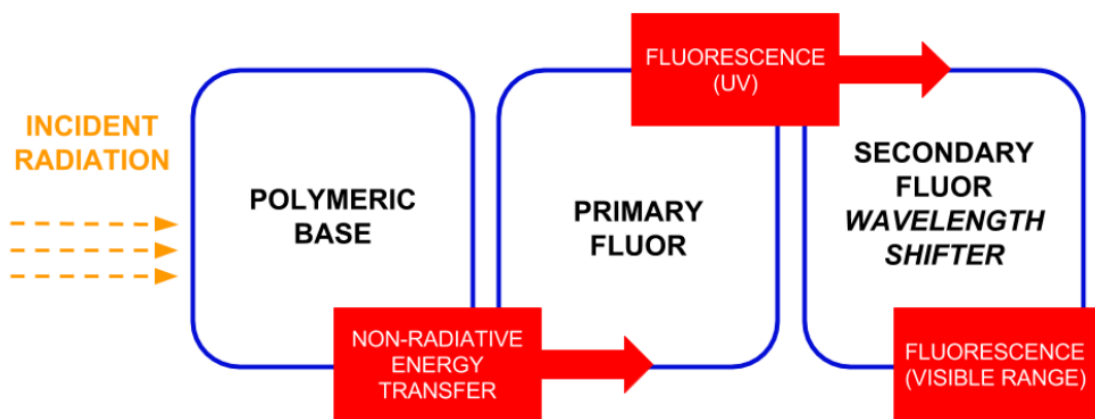


Figure 11. Transfer of energy in plastic scintillators [18]

4 Interaction and scintillator response to different radiations

The interaction mechanism of particles and radiations are different in nature. These interaction mechanism are the basis of designing a detector system. There can be different interaction mechanism depending upon different energy ranges for the same particle. That is why a variety of detection devices exist for radiations and particles. Charged particles interact with matter via excitation and ionisation. Furthermore, bremsstrahlung energy losses must also be taken into account for relativistic particles. Penetration power of neutral particles is high as compared to heavy and charged particles. Due to the interaction of neutral particles with matter charged particles are produced. Photoelectric absorption, Compton scattering and pair production are characteristic interaction processes for photon. In this chapter, the interaction mechanism of heavy particles, electron, and neutral particles i.e. photon and neutron are discussed shortly.

4.1 Heavy ions

Heavy charged particles e.g. α -particles interaction with matter is based on the Coulombic forces. The interaction is similar for all massive charged particles, starting already from protons. When a positive charged particle with kinetic energy E enters the absorbing material it immediately interacts with electrons. As a result of interaction, electron can either be excited to a higher state or completely knocked (ionization) from the atom. Due to a collision with electron, particle loses about $4Em_0/m$ of its kinetic energy, which is $\sim 1/500$ of particles energy per nucleon. Here m_0 stands for electron mass and m for mass of the charged particle.

The ratio between differential energy loss dE to differential path length dx is referred as linear stopping power P of charged particle [9].

$$P = - \frac{dE}{dx} \quad (3)$$

The specific energy loss is the same thing as stopping power and can be expressed by classical approach via Bethe formula

$$-\frac{dE}{dx} = \frac{4\pi e^4 z^2}{m_0 v^2} NB \quad (4)$$

where

$$B = Z \left[\ln \frac{Z m_0 v^2}{I} - \ln(1 - \beta^2) - \beta^2 \right] \quad (5)$$

ν = velocity of the ion

ze = charge of the ion

N = number density of electrons

Z = atomic number of absorbing material

I = average excitation and ionisation potential of the absorber

m_0 = electron rest mass

$\beta = \nu/c$

4.2 Electrons

Electrons interact with absorbing material due to Coulomb field or radiative interaction. As result of interaction, electron loses energy either by ionisation of absorbing material or radiative loss (also known as Bremsstrahlung). Unlike the heavy ions, fast electrons having the same mass as target, lose energy at a slower rate and follow a zig-zag pattern in absorbing material [9]. The collisional loss by fast electrons due to ionisation and excitation can be described by Bethe [30] expression as

$$-\left(\frac{dE}{dx}\right)_c = \frac{2\pi e^4 N Z}{m_0 v^2} \left(\ln \frac{m_0 v^2 E}{2I^2(1 - \beta^2)} - (\ln 2) \left(2\sqrt{1 - \beta^2} - 1 + \beta^2 \right) + (1 - \beta^2) + \frac{1}{8} \left(1 - \sqrt{1 - \beta^2} \right)^2 \right) \quad (6)$$

where

N = number density of electrons

Z = atomic number of absorbing material

e = elementary charge

ν = velocity of primary particle

m_0 = electron rest mass

E = electron energy

I = average excitation and ionisation potential of the absorber

$\beta = \nu/c$

According to classical theory, every charged particle will radiate energy in form of electromagnetic radiations when accelerated or decelerated [9]. Radiative energy loss can be calculated using Seltzer and Berger [31] relation

$$-\left(\frac{dE}{dx}\right)_r = \frac{NEZ(Z+1)e^4}{137m_0^2c^4} \left(4 \ln \frac{2E}{m_0c^2} - \frac{4}{3}\right) \quad (7)$$

Where the symbols are same as for equation 6. The sum of collisional and radiative energy loss is called total linear stopping power of beta particles.

$$\left(\frac{dE}{dx}\right)_c + \left(\frac{dE}{dx}\right)_r = \left(\frac{dE}{dx}\right)_{total} \quad (8)$$

The maximum range of beta particles in different absorber material can be calculated by using empirical formula provided by Katz and Penfold [32]

$$R_{max} [g/cm^2] = \begin{cases} 0.412 E_\beta^{1.265 - 0.0954 \ln(E_\beta)} & \text{if } 0.01 \leq E_\beta \leq 2.5 \text{ MeV} \\ 0.530 E_\beta - 0.106 & \text{if } E_\beta > 2.5 \text{ MeV} \end{cases} \quad (9)$$

In equation 9, E_β represents maximum beta energy expressed in MeV. The probability to stop the beta particles entirely depends on number density of electrons of absorber material. Figure 12 shows the stopping range of α and β particles in aluminum. In our case, the stopping range in EJ-200 scintillator for $^{90}\text{Sr}/^{90}\text{Y}$ beta particles having energies 0.546 MeV and 2.28 MeV can be calculated using equation 9. The calculations (see appendix A) show that in EJ-200 plastic scintillator, 0.546 MeV β particles are completely stopped by a 1.804 mm thick scintillator, leaving their total energy absorbed by the scintillator. The 2.28 MeV beta particles need a 10.7107 mm thick detector to be stopped. The calculated maximum stopping range of β particles calculated from equation 9 is consistent with Eljen technology data sheets as shown in the figure 13.

In addition, low energy electrons show a higher backscattering probability because of their small mass m_e . Backscattering is highly dependent on geometry, energy,

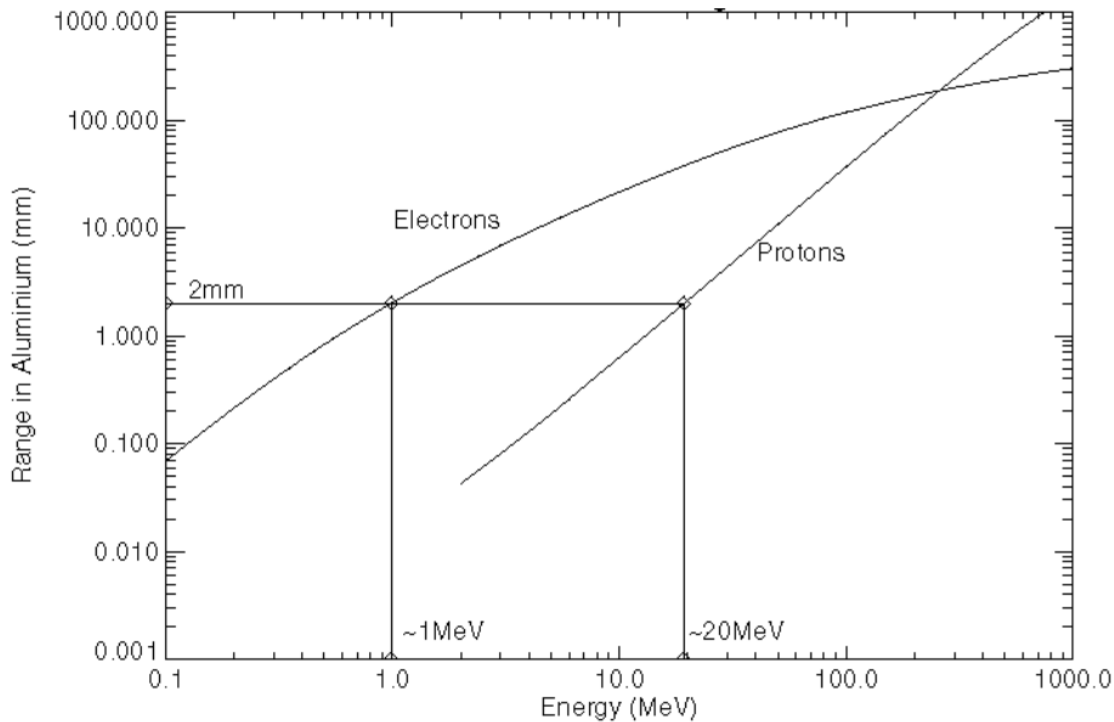


Figure 12. Proton and electron penetration range in a two mm aluminum sheet [32].

and atomic number of absorbing material. For oblique angle of incidence, the backscattering probability increases as compared to perpendicular incidence angle. The ratio between backscattered and incident electrons is known as the backscattering coefficient. Furthermore, backscattering for low energy electrons (< 10 MeV) is higher and increases for material having a high atomic number Z value. For example, an uncollimated β source irradiation on a high Z value absorber material (e.g. NaI) have a 80 % backscattering probability. That is why organic scintillators (used in this work) with lower atomic number Z are suitable for β spectroscopy. Inorganic scintillators with a high atomic number are a preferred choice for high energy beta particles, and electromagnetic radiation. The light yield of electrons is much higher as compared to heavy charged particles having the same energy due to electron interaction mechanism and small mass [22]. Figure 14 illustrates the response of EJ-200 plastic scintillator to alpha, electrons, protons, and carbon. It is clearly seen from the figure that scintillator is more sensitive to electrons.

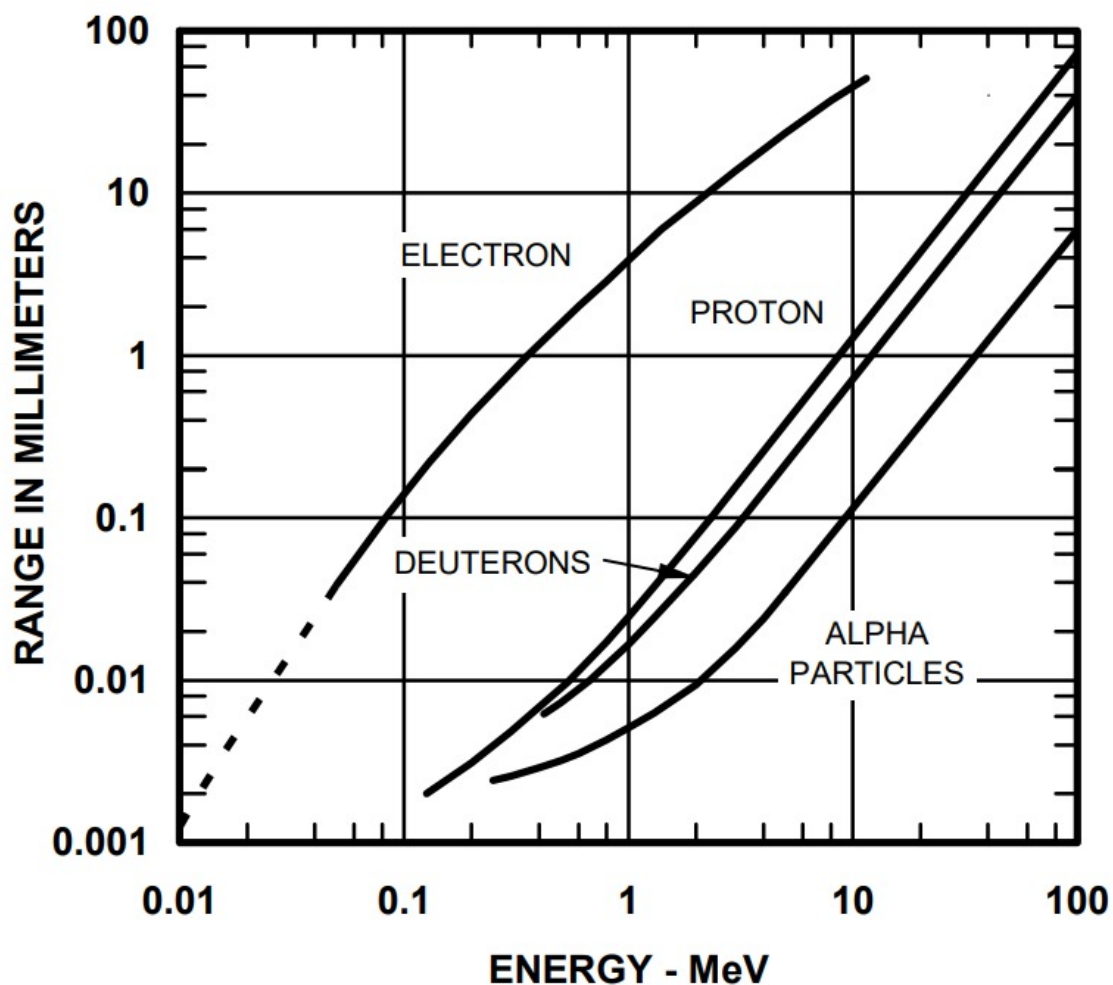


Figure 13. Range (mm) of different particles having different energies (MeV) in EJ-200 plastic scintillator [33].

4.3 Photons

The case of photon (X-rays and γ -rays) interaction with the matter is entirely different than that of α 's and β 's which interact through atomic nucleus Coulomb's field or direct electron to electron interaction. Photon energy is deposited through different mechanisms, either by photoelectric absorption, Compton scattering, or pair production. Gamma rays are more penetrative than α or β particles. Before interaction with matter, the rays travel some distance through the absorber material without any interaction. In figure 15, inorganic scintillation material NaI (used for γ -ray spectroscopy), photoelectron absorption cross-section is illustrated. The attenuation of gamma-ray intensity traveled by a distance x in material is given by

RESPONSE OF EJ-200 PLASTIC SCINTILLATOR
SCINTILLATION LIGHT PRODUCED VS. PARTICLE ENERGY

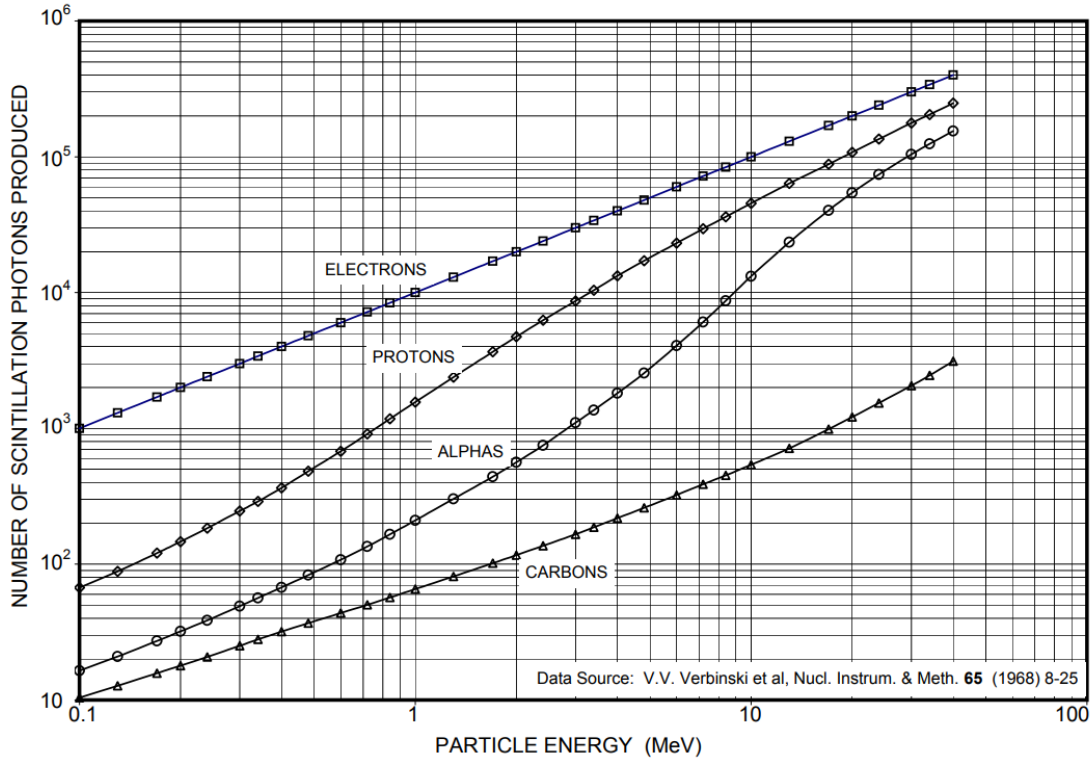


Figure 14. Response of EJ-200 plastic scintillator to different particles having MeV energy. Adopted from [34].

Beer-Lambert law

$$I(x) = I_0 \exp^{-\alpha x} \quad (10)$$

where

I_0 = intensity outside of the material

x = distance in material

α = absorption coefficient (commonly given in cm^{-1}), depends on type of material and energy E of photon; $\alpha = \alpha(E)$

The reduction of the intensity after distance x is

$$I_0 - I_0 \exp^{-\alpha x} = I_0(1 - \exp^{-\alpha x}) \quad (11)$$

Therefore, the fraction F of gamma rays that interacted with the detector is

$$F = (1 - \exp^{-\alpha x}) \quad (12)$$

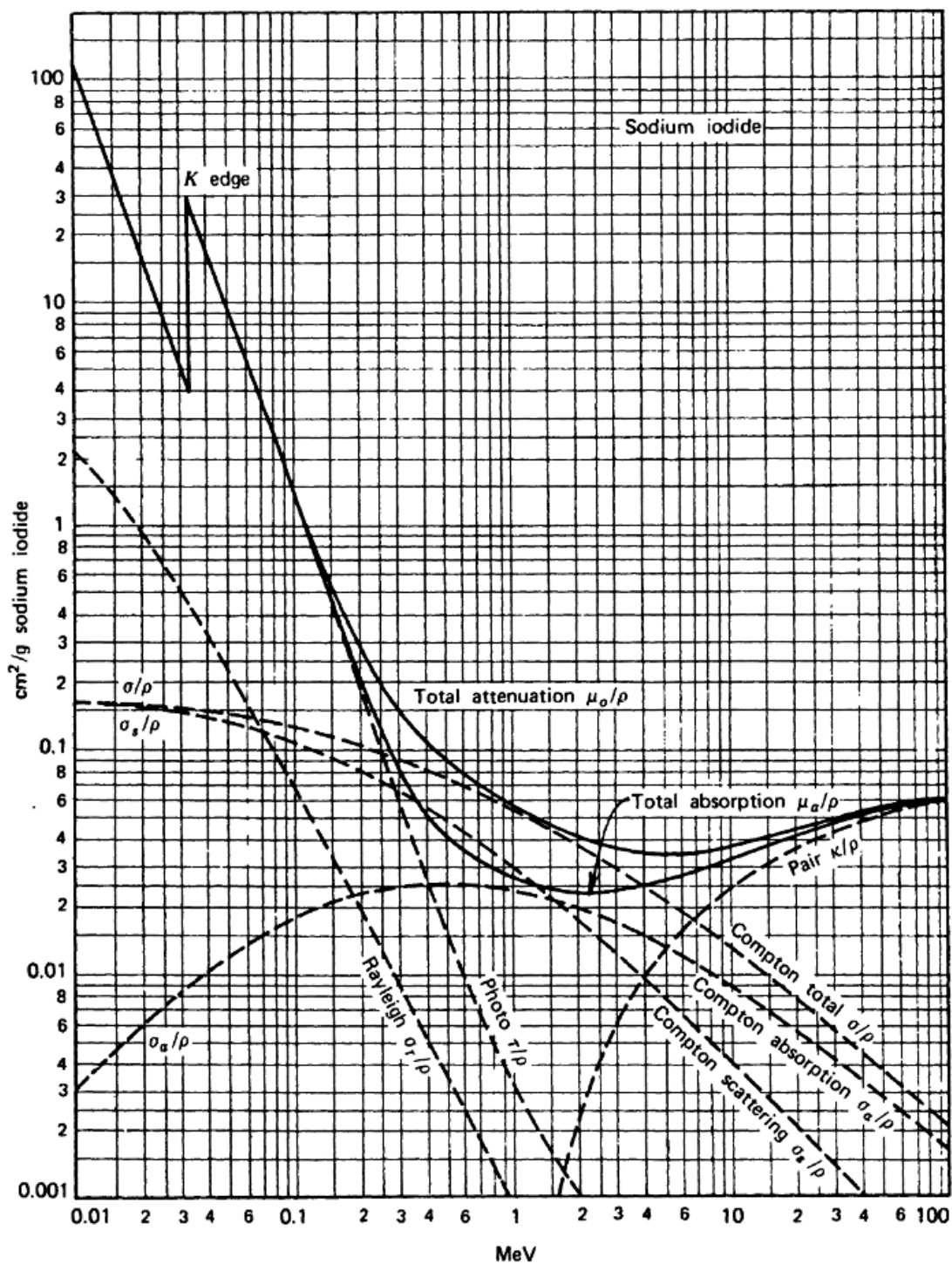


Figure 15. Energy dependence of various γ -ray interaction processes in NaI (inorganic scintillator) [9]

4.3.1 Photoelectric absorption

A process in which an incoming photon interacts with an atom by transferring its energy, results photo-electron emission from the bound shell is known as photoelectric effect. It is worth noticing that in photoelectric effect γ -rays do not interact with free electron but with the atom as a whole. The involvement of the atomic nucleus is required to satisfy the conservation of momentum. For γ -rays with enough energy, most bounded K-shell electron has a higher tendency to be emitted as photoelectron as compared to L and M. The energy E of the photoelectrons is

$$E = h\nu - E_B \quad (13)$$

where

h = Planck's constant

ν = frequency of incident photon

E_B = binding energy of emitted electron

Photoelectric absorption probability relation is given by [9]

$$\tau = constant \cdot \frac{Z^n}{E_\gamma^{3.5}} \quad (14)$$

In above equation 14, Z is the atomic number and the value of n lies between 4 and 5. It is clear from the relation that absorption cross-section is highly dependent on atomic number Z . Absorber material with a higher atomic number Z can enhance the photoelectric effect probability. Therefore, for gamma-ray spectroscopy, inorganic materials with a higher Z is a preferred choice. For low energy γ -rays ($E_\gamma \leq 100$ keV), interaction usually happens via photoelectric effect. For energies above a few hundreds of keV, most of the initial photon energy is transferred to the photo-electron.

4.3.2 Compton scattering

Photon with a little higher energies ($E_\gamma \approx 1$ MeV) undergoes Compton scattering in which an incident photon scatters from quasi-free atomic electron of absorber material, as illustrated in figure 16. Upon collision of a photon with the electron, photon is scattered by making an angle θ_γ and a part of photon energy is transferred to electron, known as recoil electron and hence called Compton electron. In Compton scattering, both the energy and momentum are conserved and from conservation

equations one can derive relation for transferred energy, scattering angle θ_γ and scattered electron energy.

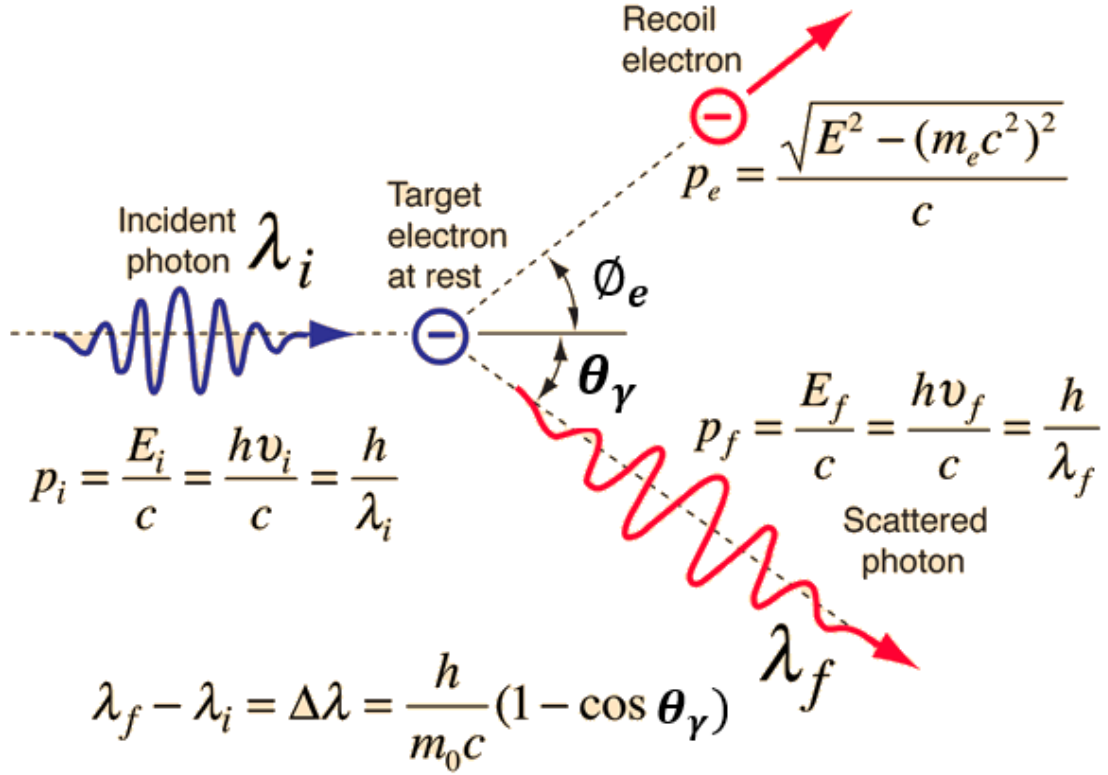


Figure 16. Compton scattering with collision kinematics. Edited from [35].

Consider a photon with initial energy $E_\gamma = h\nu$ and scattering angle θ_γ . A relation showing the scattered photon energy will be

$$E'_\gamma = \frac{h\nu}{1 + \varepsilon(1 - \cos \theta_\gamma)} \quad (15)$$

where

$$\varepsilon = \frac{E_\gamma}{m_e c^2}$$

Here, $m_e c^2$ is the electron rest mass and its value is 0.511 MeV. The energy transferred to scattered electron will be

$$E_{e^-} = E_\gamma \cdot \frac{\frac{E_\gamma}{m_e c^2} (1 - \cos \theta_\gamma)}{1 + \frac{E_\gamma}{m_e c^2} (1 - \cos \theta_\gamma)} \quad (16)$$

or

$$E_{e^-} = E_\gamma \cdot \frac{\varepsilon(1 - \cos \theta_\gamma)}{1 + \varepsilon(1 - \cos \theta_\gamma)} \quad (17)$$

Because of conservation of momentum, total photon energy can not be transferred to the electron but a part of it. In addition, scattering angle of electron ϕ_e can not be greater than $\pi/2$. With an increase in photon scattering angle θ_γ , photon wavelength shift also increases. For a small scattering angle θ_γ , the energy transfer value is small. For $\theta_\gamma = 0$ case, incident and scattered energy are same (i.e. $E_\gamma = E'_\gamma$) and scattered electron energy $E_{e^-} = 0$. In back-scattering case when $\theta_\gamma = \pi = 180^\circ$, the Compton electron energy has maximum value.

$$E'_\gamma = \frac{h\nu}{1 + 2\varepsilon} \quad (18)$$

$$E_{e^-} = E_\gamma \cdot \frac{2\varepsilon}{1 + 2\varepsilon} \quad (19)$$

Compton scattering probability of absorber material depends on number of available scattering targets (i.e. electrons) and is directly proportional to Z . Figure 15 shows the energy dependence for γ -ray absorption in NaI. The probability of Compton scattering decreases with increasing energy. The probability of Compton scattering decreases however slower than that of photoelectric effect, which makes Compton scattering dominant interaction at intermediate energies (figure 18).

4.3.3 Pair production

When high energy photons ($E_\gamma \gg 1$ MeV) is absorbed in the Coulomb field generated by nucleus then an electron-positron pair is generated, as illustrated in figure 17. According to law of conservation of energy

$$h\nu = E_- + E_+ = (m_e c^2 + K_-) + (m_e c^2 + K_+) = K_- + K_+ + 2m_e c^2 \quad (20)$$

where

E_- = total energy of electron

E_+ = total energy of positron

K_- = kinetic energy of electron

K_+ = kinetic energy of positron

Pair production is feasible when γ -rays energy is greater than the rest mass energy

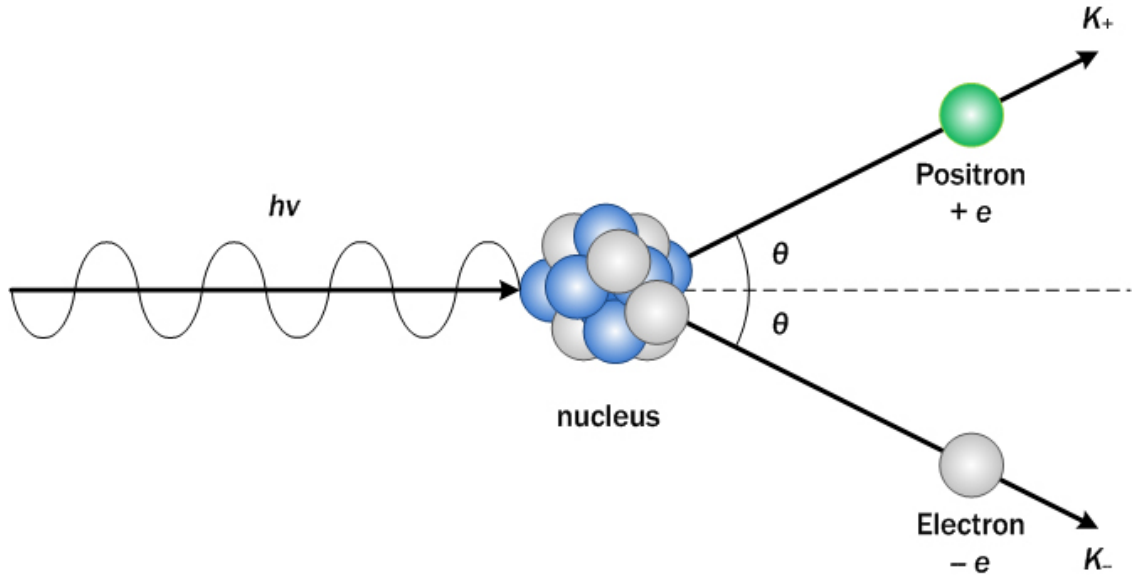


Figure 17. Pair production [36].

$\sim 2m_e c^2 = 1.022$ MeV. The pair production probability remain very low until unless the γ -ray energy value reach to several MeV.

Depending upon the photon energy range and atomic number Z of absorber material, three different possible regions for photon interaction are illustrated in the figure 18. Photoelectric effect is dominant for low energy photons with high atomic number Z of absorber material. For intermediate photon energy range, Compton scattering is dominant one. Pair production becomes feasible for high energy γ -rays [9].

4.4 Neutrons

Neutrons do not have electric charge. Therefore, neutrons interact only via nuclear forces. The probability of nuclear collisions is very low and the penetration power of neutrons is high.

On the basis of their energies, neutrons can be divided into high energy neutrons, fast neutrons, epithermal, thermal or slow, cold or ultra-cold neutrons [22]. Neutron with energies above 20 MeV are high energy neutrons. They are mostly present in outer space region. Fast neutrons have energy between a few hundred keV to tens of MeV. Fast neutrons are usually produced in nuclear fission. Epithermal neutron lie within 100 keV - 0.1 eV range.

Thermal or slow neutrons corresponds to low temperature agitation energy (i.e.

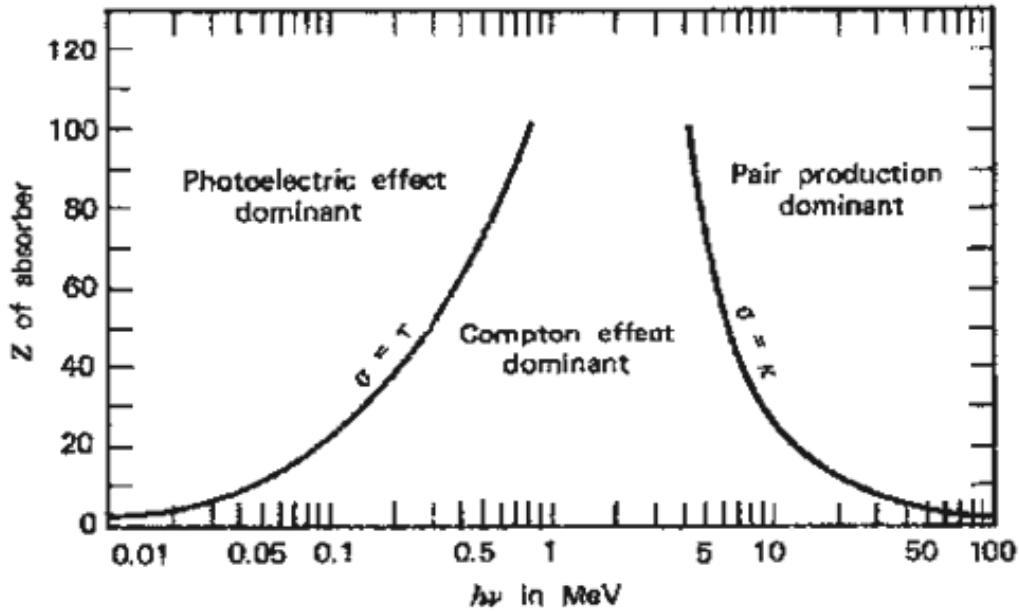


Figure 18. Probability of three types of processes due to γ -ray interaction [9]

$E = kT = 1/40$ eV) carry an energy of hundreds of eV to 0.025 eV. Last but not least, below 0.025 eV energy range neutrons are referred as cold or ultra cold neutrons [22].

Depending on neutrons energy, its interaction with nucleus can be divided into two types: scattering and absorption. In scattering reaction, neutron interaction with nuclei give back the same particles after the collision. This can be expressed as (n, n) reaction i.e.



Scattering can be inelastic or elastic. The interaction in which neutron loses kinetic energy to excite the nucleus is called inelastic scattering. The kinetic energy loss due to collision goes to excite the nucleus and after some time, excited nucleus can return to its ground state with the emission of γ -rays. In elastic scattering, both the total kinetic energy and total momentum of colliding particles remain conserved.

4.4.1 Thermal neutrons

Thermal or slow neutrons have energy from hundreds of eV down to 0.025 eV. This energy corresponds to the average energy of neutrons in thermal equilibrium at 20 °C temperature. Neutrons below this energy (0.025 eV or 0.0253 eV) are referred as cold or ultra cold neutrons. Kinetic energy and momentum can be transferred from one particle to another, but the total of both is conserved in elastic scattering.

Scintillation detectors are used for neutron detection. The interaction process is similar to gamma ray detection. Neutrons collide only on atomic nuclei. When they do, kinetic energy is transferred to the nucleus, which interacts with the detector as a heavy ion (section 4.1). The neutron energy is most effectively moved to a proton, whose mass is almost the same as that of neutron. In a head-on collision all the energy can be transferred to proton. This is why neutron detector materials typically have a high concentration of hydrogen.

All the collision however are not head-on collisions. The neutron energy transfer to the detector material is incomplete. As the result, the response of radiation detectors to neutrons is not very linear. Neutron signals can not be used for neutron energy spectroscopy. The neutron signal can however be distinguished from signals that are produced by gamma rays. The heavy charged particles tend to excite more triplet states in organic scintillators than electrons. The neutron induced signals have thus a stronger delayed fluorescence component that allows identify neutron events. When neutrons are detected with scintillation techniques, their energy is usually determined using time-of flight.

This thesis concentrate on discrimination of beta particles and gamma rays by spectroscopic means. The neutron interactions with matter and detector materials will therefore not discussed deeper.

5 Silicon Photomultipliers (SiPM)

This section starts with a brief introduction to a silicon photomultiplier (SiPM), followed by the structure, pn-junction under reverse bias, and working mode of a SiPM. In addition, terms and performance parameters connected to a SiPM have also been discussed. Primary and correlated noise have also been discussed in the last part of this section.

From the past 85 years, photomultiplier tubes (PMT) have been used for scintillation light signal detection. Traditional photomultipliers have been described in detail in references [9, 22, 37, 38]. Silicon photomultipliers (SiPM's) are more cost-effective modern alternatives of PMT's. Other advantages over PMT include compact size, low bias operating voltage (below 100 V) [39], device stability, fast timing, high gain ($10^5 - 10^6$), good quantum efficiency, single photon detection capability, and magnetic field tolerance. On the other hand, high thermal noise rate (100 kHz - few MHz), after-pulsing, and cross-talk are some disadvantages. A comparison between photomultiplier (PMT) and silicon photomultiplier (SiPM) properties is illustrated in table 10 in appendix C.

5.1 P-N Junction

A photodiode converts light into electricity. An ordinary p-n junction diode is shown in figure 19. A p-type semiconductor contains holes as majority and electrons as minority carriers. A n-type material has electrons as the majority and holes as minority charge carriers. When n-type and p-type semiconductor materials are in contact with each other, a p-n diode has formed. An equilibrium of charge concentration through diffusion of electrons and holes from n to p-type and vice versa will take place. Due to this diffusion of charges p-region will be more negatively charged and n-region will be more positively charged. A potential V_0 will be created in the form of depletion region. In a reverse bias condition, the movement of n and p carriers away from the junction creates a broader depletion region with potential $V_0 + V_b$ [21]. In addition, bias voltage will also generate an electric field across

the depletion region of the diode. When a photon shines on the silicon surface, its energy is transferred to excite electrons from the valence band to the conduction band, creating an electron-hole pair. The movement of the produced charge carriers (electrons and holes) towards electrodes under the influence of the electric field will produce current. The produced photocurrent is proportional to incident light intensity.

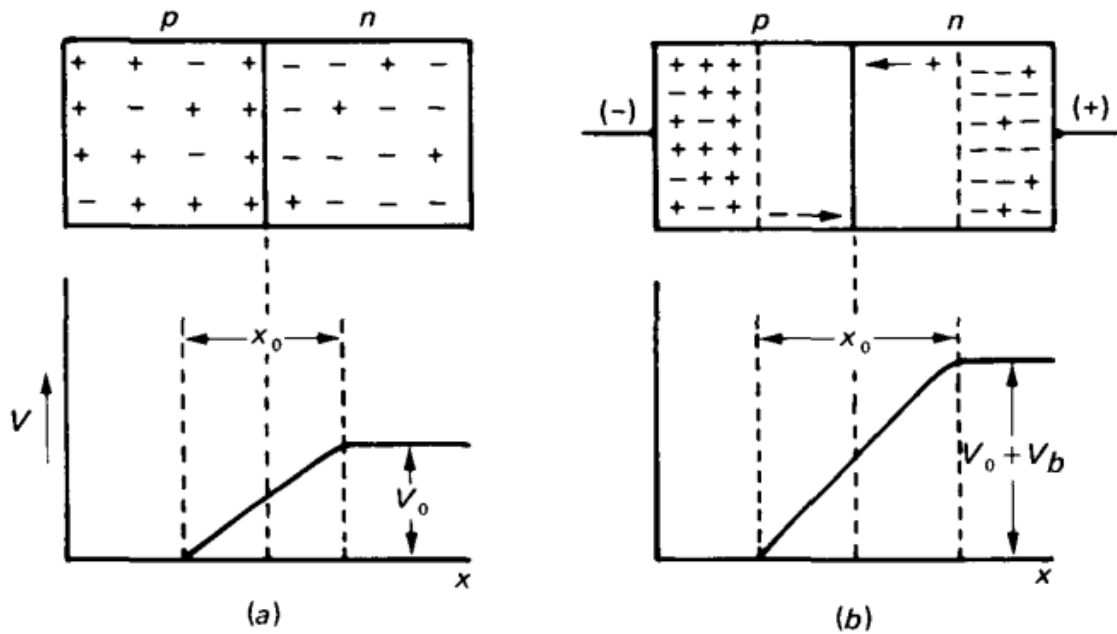


Figure 19. (a) p-n junction under no bias condition with barrier potential V_0 . (b) p-n junction under reverse bias having depletion width x_0 and increased barrier potential with a factor of V_b . Hence a total barrier potential is $V_0 + V_b$ [21].

5.1.1 P-N Junction under reverse bias condition

In reverse bias condition, p-type material is connected to the battery's negative terminal, and n-type is connected with the positive terminal. An ordinary PN-junction diode shows different behavior depending upon the applied reverse bias voltage range, as shown in figure 20a. The diode shows no charge amplification phenomenon in the low reverse bias voltage case. An incident photon only creates one electron-hole pair that is accelerated towards the terminal under the influence of the electric field. Produced current is proportional to the incoming light intensity [40].

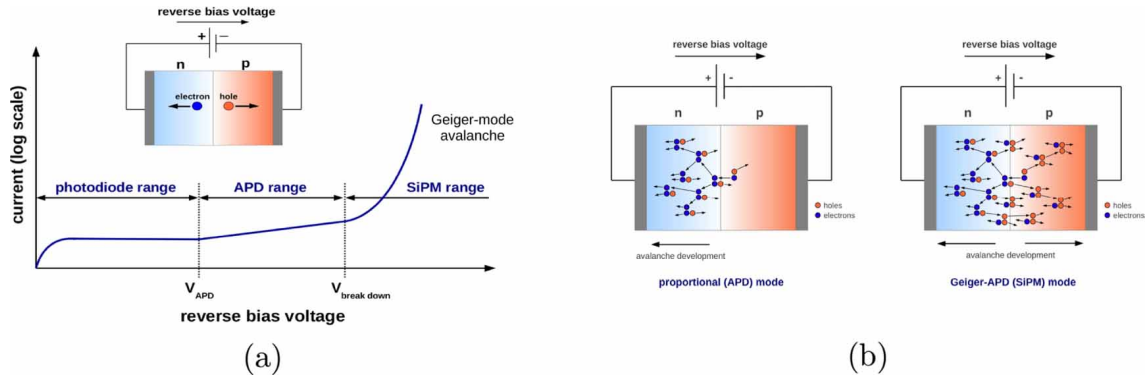


Figure 20. (a) PN-Junction diode behaviour under different ranges of applied reverse bias voltage (b) Left side figure shows one sided flow of avalanche in APD due to only e^- participation in impact ionization. Right side figure shows the avalanche development in SiPM due to electrons and holes participation in impact ionization. Adopted from [40]

5.1.2 Avalanche photodiode (APD)

Photodiode operating in near breakdown region is called avalanche photodiode (APD). An avalanche photodiode consists of P^+ substrate, n-doped guard rings, P^- absorption region, and SiO_2 anti-reflective layer as shown in the figure 21. The function of the guard ring is to provide a uniform electric field.

Under a reverse bias condition below the breakdown limit, e-h pairs are generated by incoming photons through the photoelectric effect. The electric field generated by the reverse bias voltage is strong enough to accelerate and provide enough energy to both the charge carriers (electrons and holes) to generate a secondary electron-hole pairs through impact ionization [41]. Impact ionization is basically the charge generation mechanism which is only feasible when an external electric field provides enough energy to charge carrier for ionization. The number of e-h pairs produced by a charge carrier (e or hole) per unit distance traveled is known as ionization rate α .

The ionization rate value is different for electrons α_n and holes α_p , and α_n is always greater than α_p [42]. Therefore, in an avalanche photodiode, the avalanche is initiated by the electrons and flows in one direction, as illustrated in figure 20b left panel. The gain depends on the applied voltage and diode temperature. APD gain ranges from tens to hundreds and current flow is directly related to detected light intensity. No external circuit is required to stop the avalanche.

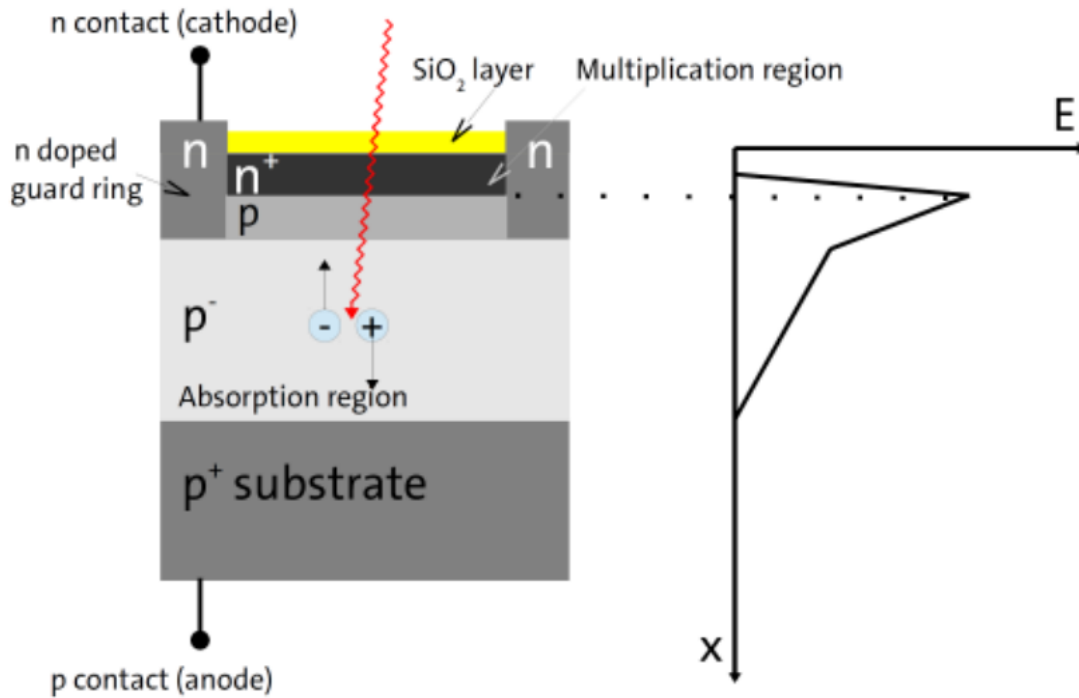


Figure 21. An internal 1D structure of an APD with electric field strength [41]

5.1.3 Geiger-mode avalanche photodiode or SiPM mode

The avalanche photodiode (APD) operated in above breakdown voltage (V_{BD}) region is called Geiger-mode avalanche photodiode (GM-APD) or single photon avalanche diode (SPAD). A silicon photomultiplier (SiPM) discussed in detail in section 5.2 consists of numerous such small SPAD's called microcells. SPAD is designed to operate in Geiger mode. The technical design of SPAD is almost the same as of APD. The only difference is the applied reverse bias voltage value. APD operates below or near the breakdown region, whereas SPAD works typically 10 - 20 % above the breakdown voltage [41]. Figure 22 shows the basic internal structure of a SPAD having a abrupt n+/p junction and a lowly doped (π) layer with an enrichment box (p).

At high temperature, the charge carriers loose more energy due to scattering with crystal lattice. Therefore, a higher electric field is required to accelerate the charge carriers. Reverse bias voltage above the breakdown limit generates a higher electric field (order of a few 10^5 V cm^{-1}) [40]. This high electric field gives enough energy also to holes generate a secondary electron-hole pairs through impact ionization. The

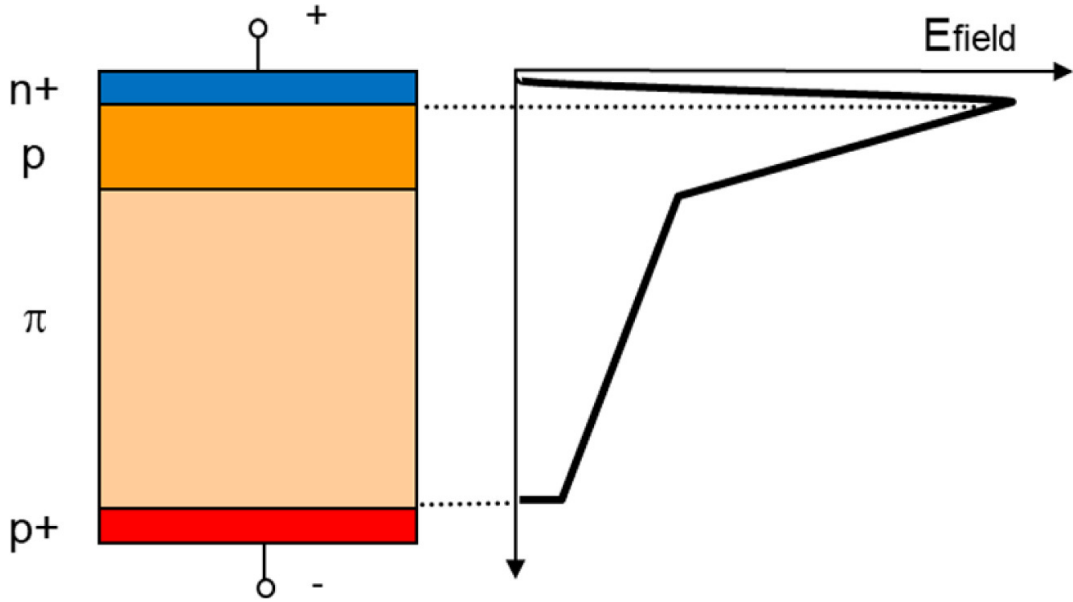


Figure 22. Figure showing the internal structure of a single avalanche photodiode in 1D and electric field strength. Figure from [43]

upper part of SPAD behaves as a multiplication region and the lower part as a drift region. The upper side region (p side) offers a high electric field, and photo-generated electrons in the lower part are being pushed towards the high electric field region [43]. These generated charge carriers create a self-perpetuating ionization avalanche in the depletion region as shown in figure 20b right panel. Therefore, silicon behaves as conductor drawing macroscopic current. This process can be stopped by either by passive quenching or by active quenching. In passive quenching, a resistor R_Q is connected in series with the diode. The voltage provided over the SPAD and the resistor is constant. Voltage over the SPAD, V_{SPAD} depends on the resistance of the diode R_D and the the quenching resistor R_Q as

$$V_{SPAD} = \frac{R_D}{R_D + R_Q} V \quad (22)$$

Normally the resistance of the diode R_D is very large and $V_{SPAD} \approx V$. During the avalanche diodes resistance drops and so does V_{SPAD} . This stabilises the breakdown current and eventually brings $V_{SPAD} < V_{BD}$, when the current stops and the diode reset to detect subsequent photons [44]. Each detected photon results in a cycle of avalanche, quench and reset. In active quenching, a transistor is used instead of a

resistor. The details of active quenching mechanism are described in reference [45].

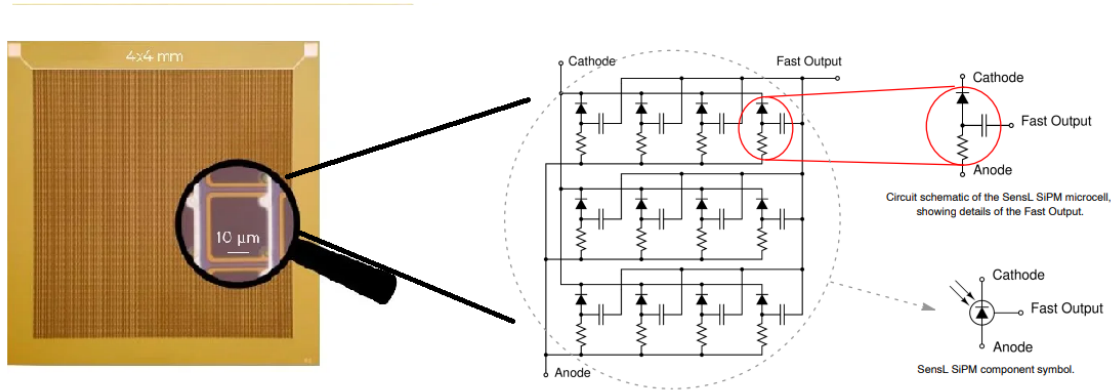


Figure 23. Left: A SiPM contains of up to tens of thousands microcells (tiny SPAD's). Right: A simplified circuit schematics of the SensL SiPM, comprise of 12 microcells with seperate quenching resistor and capacitive circuit. Edited from [46] [47]

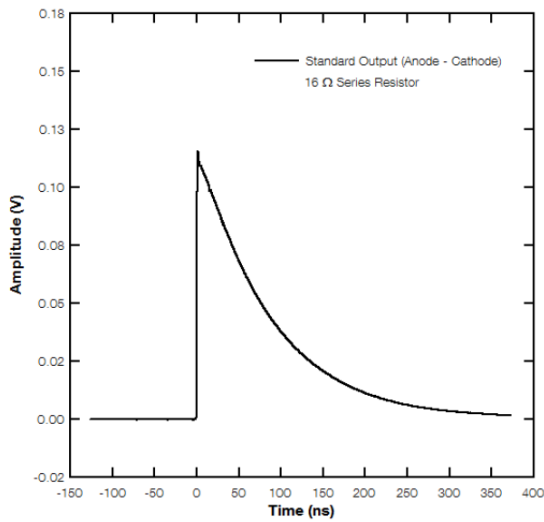


Figure 24. 6 mm SensL (Micro FJ-60035-TSV) SiPM standard output pulse shape without a capacitive circuit [48]

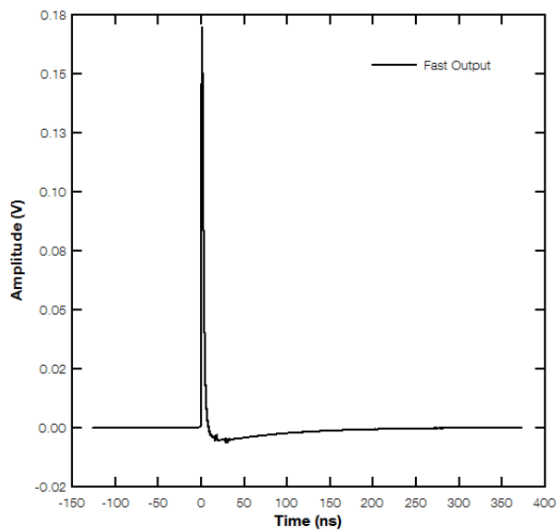


Figure 25. 6 mm SensL (Micro FJ-60035-TSV) SiPM fast output pulse shape with a capacitive circuit [48]

The one issue with a single SPAD is that the signal does not depend on how many photons were absorbed. One can not distinguish the single photon signal and two or more incoming photons signal. A single SPAD sensor is not capable to provide information on the number of the incident photon. To overcome this issue, a device consisting of an array of SPADs connected parallel to same external bias (see figure

23) has been developed. These SPADs have been miniaturised and therefore called microcells [49]. Each microcell is equipped with its own quenching resistor attached in series with the diode. These devices are called by several commercial marketing names [40], but silicon photomultiplier (SiPM) is a commonly understood term. A SiPM can contain from hundreds up to tens of thousands microcells, as shown in figure 23. A capacitive circuit in each microcell is used for fast timing applications. The typical output pulse without and with a capacitive circuit is illustrated in figure 24 and 25 respectively. Each microcell is capable of detecting photons individually.

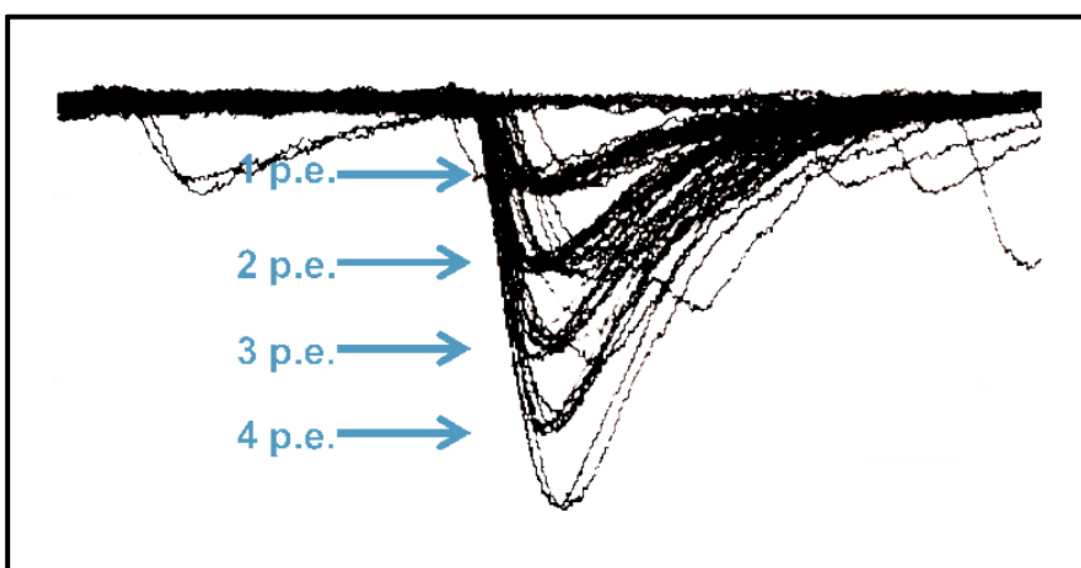


Figure 26. Low level light pulse output in a SiPM. Retrived from [48]

The sum of photocurrents gives information about the magnitude. Figure 26 shows the detected SiPM signals of different (low) number of incoming photons.

5.2 Structure of a SiPM

Silicon photomultiplier (SiPM) is a Geiger-mode avalanche photodiode based photon detector, which is capable of working at room temperature. The SiPM are labeled as solid-state photomultipliers (SSPM), multipixel photon counter (MPPC), single photon avalanche diode (SPAD), multi-pixel avalanche diode (MPAD), depending on the manufacturer [40]. In this work, they are all called as silicon photomultipliers. SiPM consists of an array of pn-junction based microcells connected parallel to each other on a silicon substrate (p or n type) as shown in figure 23. The microcells are

squares whose typical size varies from 10 to 100 μm [50]. The obtained signal is the sum of all the signals of connected microcells.

In this work, two MicroFC-60035 $6 \times 6 \text{ mm}^2$ silicon photomultipliers of Onsemi company were used. The technical specification of the used SiPM product is given in table 3.

Table 3. Technical details of (MicroFC - 60035) $6 \times \text{mm}^2$, 35 μm SiPM. Edited from [51, 52]

Parameter	Value
Breakdown voltage (V_{BD})	(24.2 - 24.7) V
Recommended overvoltage (V_{ov}) range	(1.0 - 5.0) V
Spectral range	(300 - 950) nm
Peak wavelength	420 nm
Minimum operating temperature	- 40 °C
Maximum operating temperature	+ 85 °C
Temperature dependence of V_{BD}	21.5 mV/°C
Temperature dependence of Gain	- 0.8 °C
PDE at λ_p	31 % at $V_{BD} + 2.5 \text{ V}$ 41 % at $V_{BD} + 5.0 \text{ V}$
Gain	3×10^6 for $V_{BD} + 2.5 \text{ V}$
Rise Time	1 ns
Microcell recharge time constant	95 ns
Active area	$6 \times 6 \text{ mm}^2$
Number of microcells	60035 : 18980
Fill factor	64 %
Dark current	(618 - 1750) nA
Dark count rate	(1200 - 3400) kHz
Cross talk	7 %
After pulse	0.2 %

5.2.1 Equivalent electronic circuit

Figure 27 illustrates the equivalent electronic circuit of a single SPAD. The applied voltage is V_{BD} , junction capacitance is denoted by C_D , and R_S represents the space charge resistance of the avalanche region. In addition, there is also a quenching resistor R_Q connected in series [43].

At time $t=0$, the avalanche process has initiated, and resistor R_S discharges the capacitance with V_{BIAS} to V_{BD} . As a result, the current flowing through the circuit i.e. $I_{INT} = (V_{BIAS} - V_{BD})/R_S$ will decrease exponentially. On the other

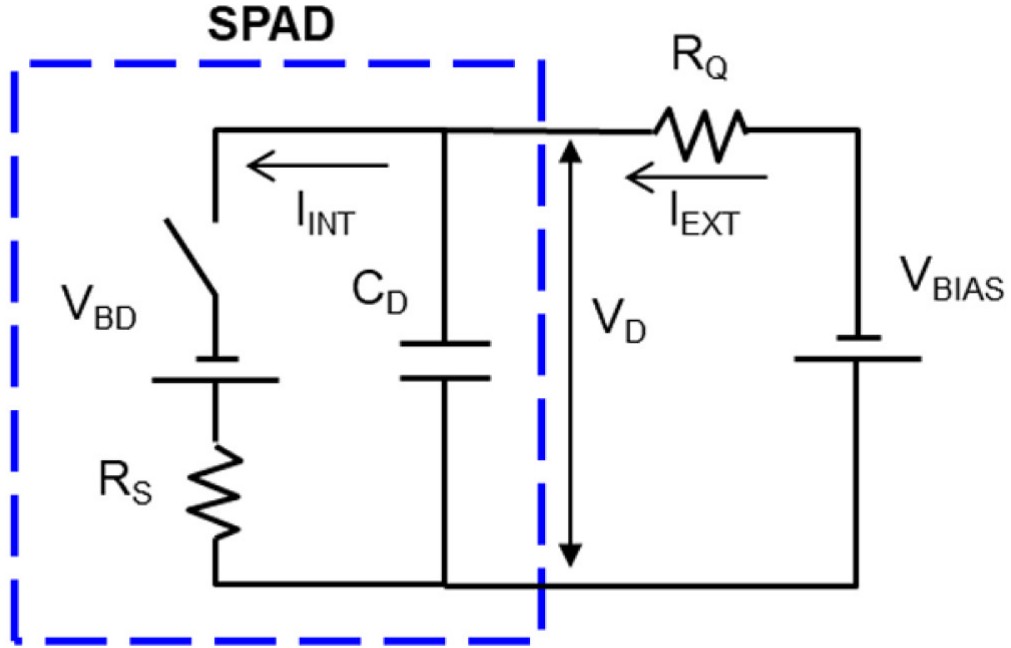


Figure 27. The basic equivalent electronic circuit model of single photon avalanche diode along with a quenching resistor R_Q and a capacitor with capacitance C_D . [43]

hand, external current i.e. $I_{EXT} = C_D R_S$ will increase. At time $t = t_1$, the current reaches its maximum value i.e. $(V_{BIAS} - V_{BD})/R_Q$, and the avalanche process has quenched with probability P_Q . After this, the switch goes to an open state.

The flowing current I_{INT} drops to zero, and the external current I_{EXT} shows an exponential decrease. The junction capacitance C_D will start to recharge until the original bias voltage level has reached with time constant $C_D R_Q$. The quenching probability P_Q and avalanche triggering probability P_T are key elements of a microcell. The first one P_Q will give an insight into the number of carriers enabled to cross the high field region. Photon detection efficiency is dependent on this factor. On the other hand, triggering probability P_T will give information about the produced charge carrier, capable of generating the Geiger discharge. It is directly related to detector efficiency [43].

5.2.2 Pulse shape

For a SiPM, the shape of output pulse is shown in the figure 28. It contains a quick rise time due to the avalanche process, then a slow decay time due to the recharging of the pixel. The pulse rise time depends on total device area and effective capacitance. It ranges from one to hundreds of nanoseconds. For example, the rise time of a 1 mm SiPM is ~ 1 ns, and for 6 mm it is ~ 10 ns [53].

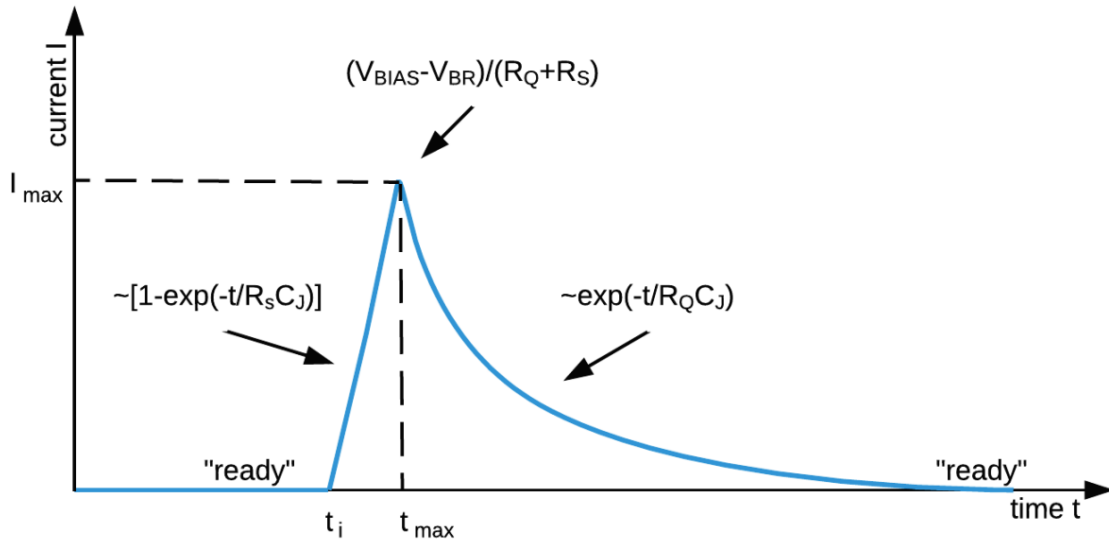


Figure 28. Current output for different phases in a SiPM. Quenching resistor R_Q determine the value of peak current. The rise and the recovery time is dependent on effective capacitance C_D . [54]

The decay time or the recovery time is dependent on device size, and can be determined by the reset period. The reset period of a microcell can be calculated using

$$\tau_{reset} = R_Q \cdot C_D \quad (23)$$

In the above relation, R_Q is the quenching resistor and the effective capacitance of all the microcells is represented by $C_D = C_d + C_q$, where C_d is the depletion region capacitance and C_q is the parasitic quenching capacitance. Quenching resistor R_Q is constant for a given SiPM. Therefore, reset time is a function of effective capacitance C_D that is dependent on the area of a microcell. In other words, different sizes of microcells will give different reset times. For example, a 35 μm SiPM will have a shorter reset time than a 100 μm SiPM.

In the ready state of a microcell, no current i.e. $I(t) = 0$, flows from the cell. At

the time t_i , an avalanche is triggered due to e-h pair production in the depletion region. This avalanche process is quenched by a quenching resistor R_Q and the value of current reaches its maximum point [55]. The maximum current value I_{max} at time t_{max} is given by

$$I_{max} \approx \frac{V_{Bias} - V_{BD}}{R_Q} \quad (24)$$

The maximum current value is dependent on overvoltage V_{ov} and quenching resistor. Equation 25 gives total charge Q due to avalanche process [56]

$$\int_{I(t=0)}^{\infty} I(t) dt = Q = C_D \cdot (V_{Bias} - V_{BD}) \quad (25)$$

After time (t_{max}), current starts to decrease slowly.

5.3 Terms and performance parameters associated with SiPM

5.3.1 Breakdown voltage and overvoltage

The minimum applied reverse bias voltage that generates a Geiger discharge in the depletion region and above which avalanche photodiode operates in Geiger mode is called the breakdown voltage (V_{BD}). Figure 29 shows the current and voltage relation for different dimensions (20 μm , 35 μm , 50 μm , and 100 μm) of microcells [49]. In this graph, the voltage value 27 V is the breakdown voltage point above which a sudden increase of current takes place. The difference between applied bias voltage V_{bias} and breakdown voltage V_{BD} is called overvoltage V_{ov} .

$$V_{ov} = V_{bias} - V_{BD} \quad (26)$$

SiPM diode operating voltage V_{bias} is typically 10 - 25 % higher than the breakdown voltage V_{BD} , as depicted in the figure 29.

Bias voltage and overvoltage are highly temperature-dependent. The dependence between temperature and breakdown voltage is shown in figure 30. The graph shows a linear relationship between the temperature and V_{BD} above -120 °C. Below -120 °C, the linear dependence breaks, the decrease V_{BD} slows down, and the V_{BD} seems to saturate towards $V_{BD} \approx 20.7$ V below -200 °C. The temperature coefficient ~ 21.5 mV/°C of this particular SiPM in the linear region is small as compared to

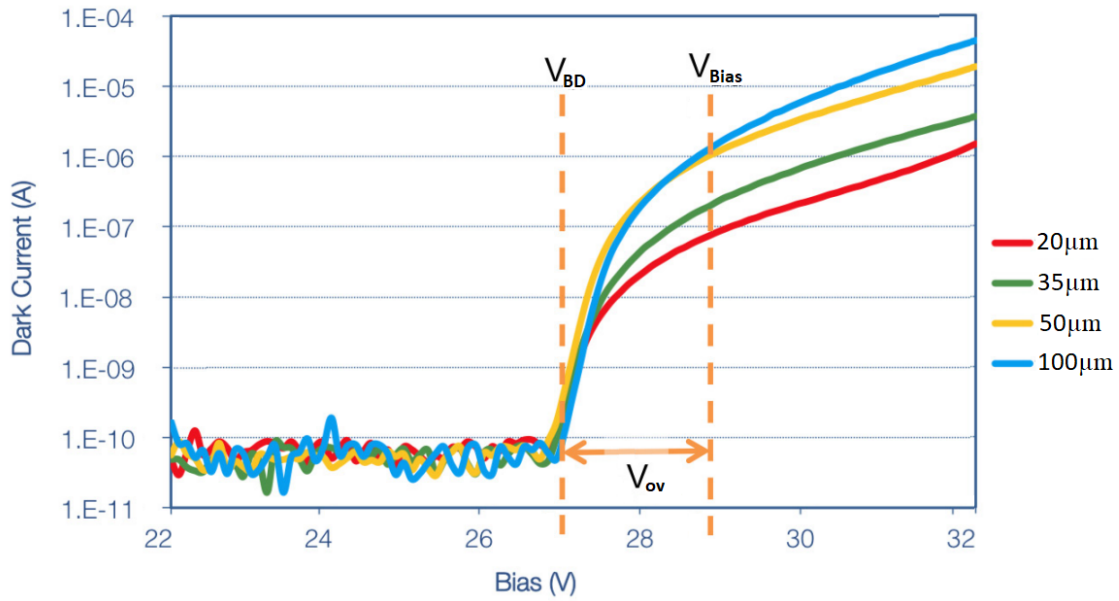


Figure 29. I-V graph showing sudden current increase behaviour above breakdown voltage for different sized microcells. Edited from [49]

some other similar devices [57].

At temperatures above $-120\text{ }^{\circ}\text{C}$, the chances of more energy losses by charge carriers due to crystal lattice scattering. As a result, the charge carriers require more energy to initiate the impact ionization process. This extra energy is provided through a higher electric field strength. Therefore, a higher bias voltage value is required to generate a stronger electric field in the depletion region [58]. An increase in the bias voltage means a higher value of breakdown voltage and lower value of overvoltage. A lower V_{ov} value will ultimately affect the other performance parameters of SiPM. Conversely, a higher V_{ov} value dramatically increase noise factor, hence limiting the bias voltage up to a certain upper limit. Therefore, for a stable operation, the large temperature fluctuations need to be compensated by adjusting bias voltage.

Method for Temperature Compensation: There are many methods to decrease the temperature fluctuation, described in references [59–63]. One of these method to control the temperature fluctuation is to cool the detector by using a peltier element [64]. It operates on the thermoelectric principle or Seebeck effect. In a peltier element, the applied current transfers heat from one side of the element to another. A peltier element is shown in the figure 31.

Another proposed method is to monitor the temperature through a programmable

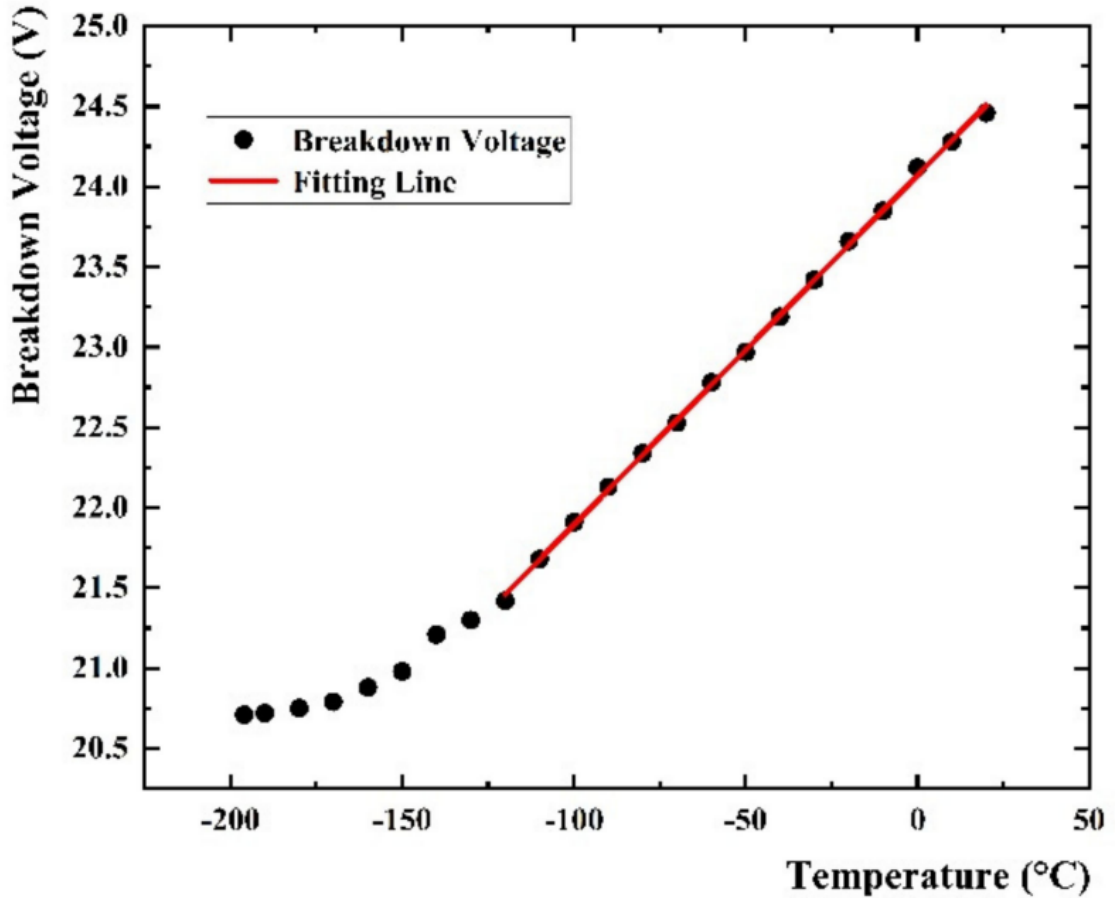


Figure 30. Temperature dependence of breakdown voltage (V) from room temperature (20°C) to liquid nitrogen temperature (-196°C) for J-series (J-60035, $6\times 6\text{ mm}^2$) SensL SiPM. [57]

PC device [59, 60, 65]. In this method, active monitoring of the bias voltage is done through a controllable PC device. The typical range of overvoltage is 2 to 5 V [66]. For a good performance of SiPM, the overvoltage needs to be kept constant.

5.3.2 Photosensitivity

Photosensitivity is defined as the output current of a PMT or SiPM divided by the power of the electromagnetic radiation hitting the photocathode of the PMT or the microcell array of the SiPM. The unit of the photosensitivity is thus A/W. Photosensitivity gives a limited picture of the photomultiplier capability. A single photon can photoemit at most one electron from the photocathode. Similarly, a single photon typically triggers only one avalanche in one microcell. The energy of a 300 nm photon is two times higher than that of a 600 nm photon. It is needed twice

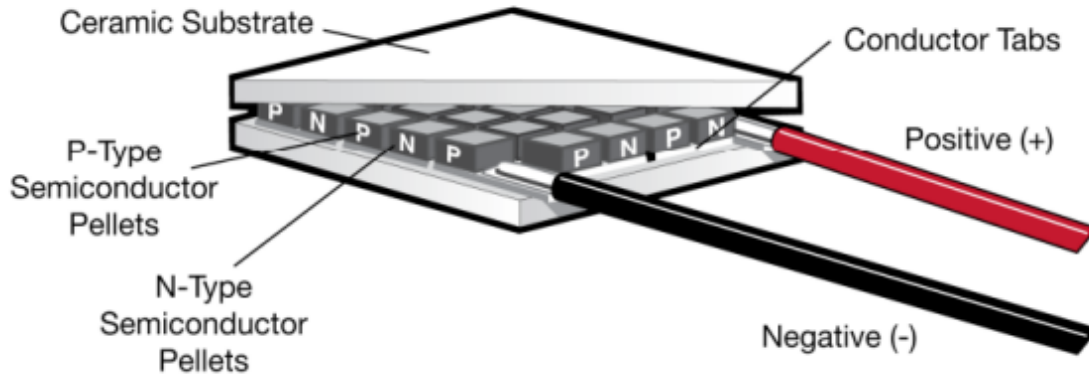


Figure 31. A peltier element composed of several blocks of n and p-doped semiconductor material [64]

as many photons to produce the same power at 700 nm than at 300 nm. To reach the same photosensitivity, 300 nm photons need to be two times more effective to cause photoemission or trigger a microcell avalanche.

In addition, photosensitivity is proportional to gain, so that photosensitivity depends on the applied voltage for both PMT's and SiPM's. For PMT, the intrinsic efficiency is described by the quantum efficiency (QE) of the photocathode defined by

$$QE = \frac{\text{Number of emitted photoelectrons}}{\text{Number of incident photons}} \quad (27)$$

The PMT quantum efficiency can approach $\sim 50\%$ for some wavelengths of incident radiation [67] but never exceed it. This is because the photoelectron has to escape from the cathode material. The probability of a photoelectron excited at the surface at cathode to escape is $\sim 1/2$ [68], and it is lower for the electrons excited deeper in the bulk of the material.

5.3.3 Photon detection efficiency

In SiPM, the efficiency is best described by the photon detection efficiency (PDE). It is related to the detection sensitivity and is defined as the probability of photon detection by a SiPM [40]. The three-factor formula represents the photon detection efficiency

$$PDE(\lambda, V_{ov}) = QE(\lambda) \cdot F_{geo} \cdot P_T(\lambda, V_{ov}) \quad (28)$$

In this formula, $QE(\lambda)$ is the quantum efficiency, F_{geo} is the geometrical fill factor, and triggered avalanche probability is represented by P_T . The PDE consists of several factors: quantum efficiency, effective area of the SiPM, entrance window losses, breakdown possibility and the recovery time [69].

Quantum efficiency for photodiode is defined as the probability of an electron-hole pair production due to the absorption of an incident photon by microcell of SiPM. It is associated with the incident photon's wavelength λ . For example, the quantum efficiency value for a SiPM developed same as for CERN CMS experiment at 500 nm wavelength was more than at 80 % [70].

The quantum efficiency of an APD (and consecutively that of SiPM) is defined differently as

$$QE = \frac{\text{Number of produced electron-hole pairs}}{\text{Number of incident photons}} \quad (29)$$

The quantum efficiency reaches 100 % if the energy of incident photons is higher than the energy gap of ADP material (1.1 eV in silicon).

The effective area or fill factor F_{geo} for any device is defined as the ratio between active area over total area.

$$F_{geo} = \frac{A_{active}}{A_{total}} \quad (30)$$

The device's total area includes dead regions, i.e. quenching resistor, trenches, and the metal layer as illustrated in figure 32. Depending upon the layout design of the device, the fill factor value ranges from (35 - 80) % [71–73]. The small effective area can be compensated by illuminating the device from the back side. In addition, a better layout design and advanced lithography techniques can also enhance a device's fill factor [74].

Entrance window losses in a SiPM arises due to absorption and reflection. With the use of optical pure material and antireflective coating, the transimission efficiency can be enhanced up to 90 %. [69]

The breakdown probability is the probability of self-sustaining avalanche production by the electron-hole pair. It depends on the electrical field strength

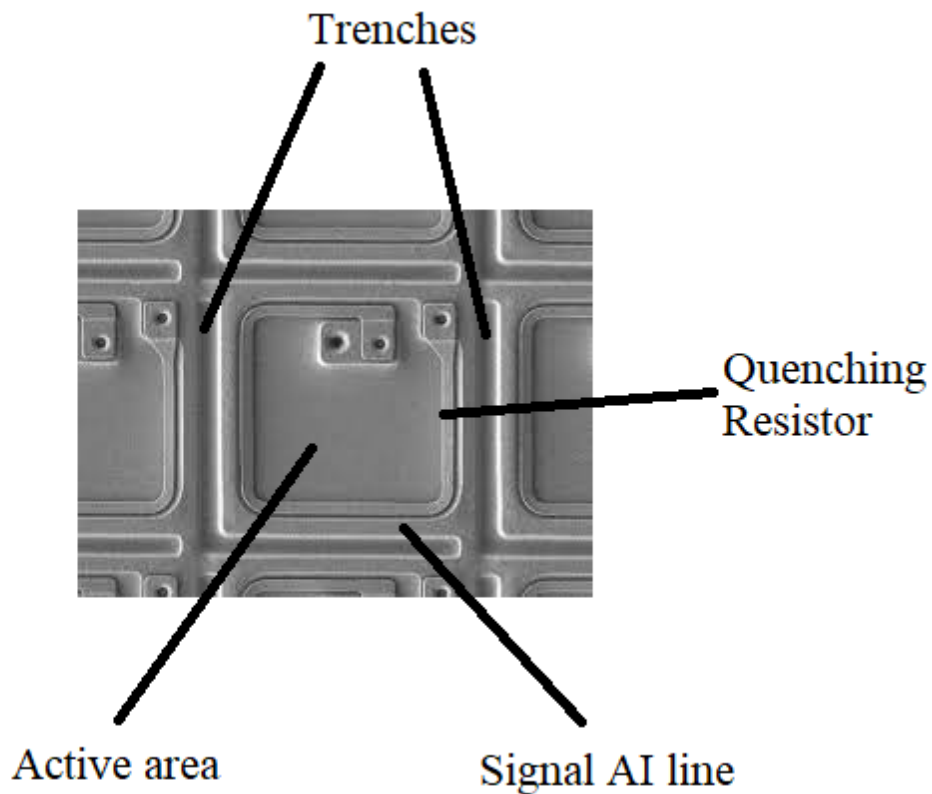


Figure 32. Figure illustrating active area, quenching resistor, trenches, and signal AI line

and wavelength λ of an incoming photon [75]. A higher value of bias voltage i.e., overvoltage V_{ov} produces a stronger electric field, hence increasing the chances of an avalanche. It is common believe that a 100 % breakdown probability can be achieved. The breakdown probability is also dependent on charge carrier type (electron/hole) as both can initiate the avalanche breakdown [69].

The recovery time is the time required for a microcell to again become fully sensitive for subsequent photon detection after a breakdown. This recharge time is usually less than μs . PDE is also dependent on the recovery time. About 0.1 % - 1 % microcell are always in a state of recovery due to background noise and dark current. For low light applications, this decrease in the PDE is negligible. However, for intense

light applications, the case is different as recovery time becomes comparable with consecutive events.[69]

For a given SiPM, geometrical fill factor F_{geo} and quantum efficiency QE are constant. Therefore, photon detection efficiency PDE only can be adjusted by triggered avalanche probability i.e. incoming photon's wavelength and overvoltage. Figure 33, and 34 demonstrate the dependence of photon detection efficiency on wavelength λ and overvoltage V_{ov} . According to figure 33, the maximum achieved value of PDE is around 40 % at $\sim 420 - 450$ nm. But, with the back illuminated SiPM this value can be up to 80 % [69]. In figure 34, an increase in bias voltage result increase in the PDE in almost linear fashion.

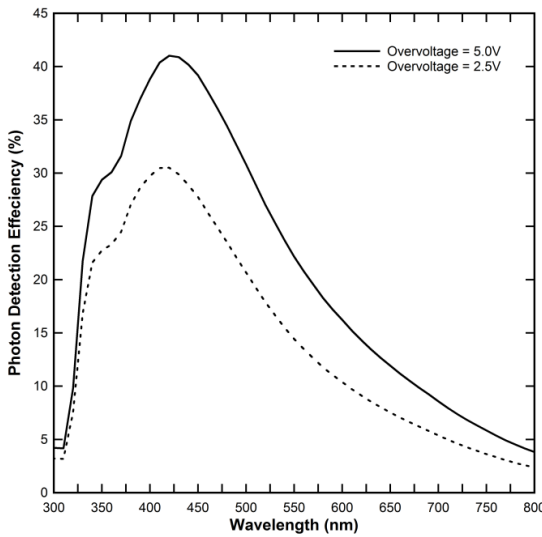


Figure 33. Photon detection efficiency versus wavelength graph of SensL MicroFC-350035-SMT SiPM for different overvoltages V_{ov} [48]

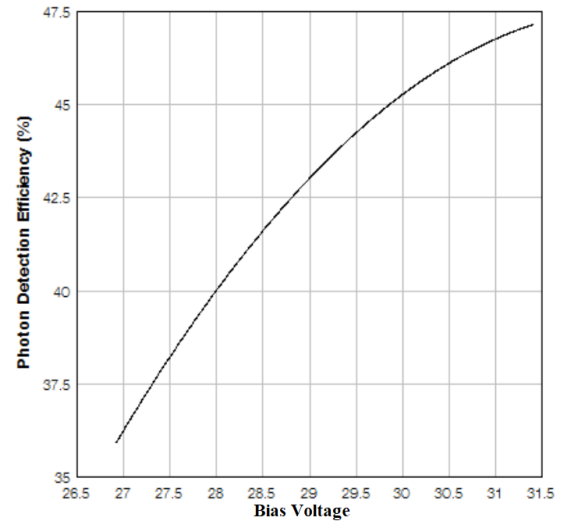


Figure 34. Photon detection efficiency versus bias voltage graph at 420 nm for 6 mm SensL MicroFJ-60035-TSV SiPM. Size of microcell is $35 \mu\text{m}$ [48]

Responsivity R or spectral sensitivity of a sensor generally affect the PDE and is define as the ratio between produced photocurrent to the optical power [48].

$$R = \frac{I_p}{P_{op}} \quad (31)$$

where

I_p = measured photocurrent

P_{op} = incident optical power

The unit of responsivity R is amperes per watt (A/W). Responsivity dependence on wavelength for a 3 mm SiPM is shown in figure 34. In addition, photon detection efficiency can also be calculated using the responsivity R [48]

$$\text{PDE} = \frac{h \cdot c}{\lambda} \cdot \frac{R}{G \cdot e} \cdot \frac{1}{(1 + P_{AP})} \frac{1}{(1 + P_{XT})} \cdot 100\% \quad (32)$$

where

R = responsivity

h = Planck's constant

c = speed of light

λ = incident photon wavelength

G = gain

e = elementary charge

P_{AP} = afterpulse probability

P_{XT} = crosstalk probability

5.3.4 Gain

The incident photon-created avalanche process, generates a fixed amount of charge carriers, called gain of a SiPM. Each SPAD working in Geiger mode results in the same output number no matter the number of charge carriers taking part in the triggering process [58]. The gain value ranges from $10^5 - 10^7$ [76]. The generated charge of each microcell is highly uniform and quantized. The ratio between the total charge generated by the active area of microcells to charge on an electron is named gain G of a SiPM. The equation for gain calculation is

$$G = \frac{\text{Total produced charge}}{\text{Charge on electron}} = \frac{Q_{out}}{e} = \frac{C \cdot V_{ov}}{e} \quad (33)$$

where

Q_{out} = total charge

C = Single microcell capacitance

V_{ov} = overvoltage

e = elementary charge

The gain G is directly related to overvoltage V_{ov} and the size of SiPM's microcell. Overvoltage is a temperature dependent factor as discussed section 5.3.1. Therefore, the gain is directly temperature-dependent. At higher temperatures, the probability of charge carriers (electron or holes) collision with the crystal lattice increases, resulting in loss of energy. Charge carriers need more energy for impact ionization and initiation of the avalanche process. Therefore, at a particular bias voltage, an increase in temperature results decrease in overvoltage V_{ov} . Decrease in gain as illustrated in figure 35.

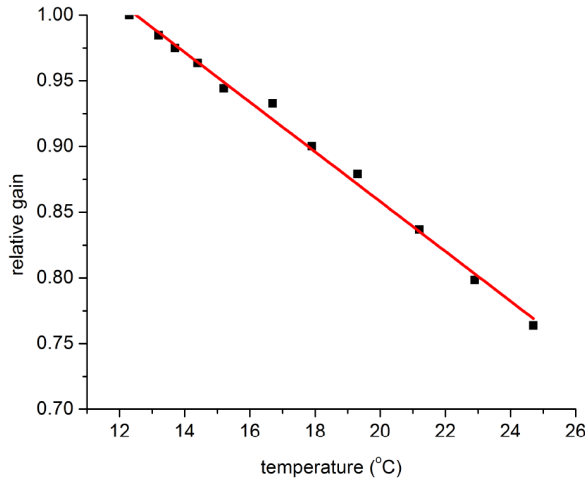


Figure 35. Gain decreases with increase in temperature in Hamamatsu $1 \times 1 \text{ mm}^2$ SiPM with ($50 \mu\text{m}$ microcell size) at constant bias voltage [77]

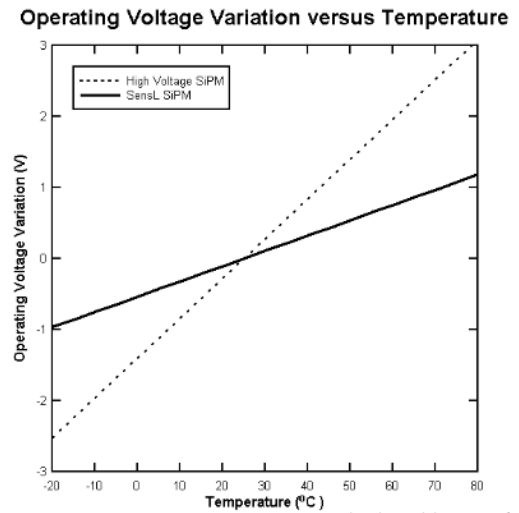


Figure 36. Comparison of temperature coefficients between a high voltage silicon photomultiplier and SensL SiPM [78]

The temperature should be consistent for a constant gain, or the bias voltage needs to be adjusted accordingly. Among the available SiPM's, SensL has a lower breakdown voltage V_{BD} due to a narrow depletion region and doing layer. On the other hand, high voltage SiPM having a high bias voltage are more sensitive than the SensL SiPM, as shown in the figure 36. It shows a temperature variation of $21.5 \text{ mV}/^\circ\text{C}$ [78].

The other two factors in the equation, microcell capacitance and electron charge, show no change under a constant temperature. The effect of overvoltage and microcell size, on the gain is illustrated in figure 37.

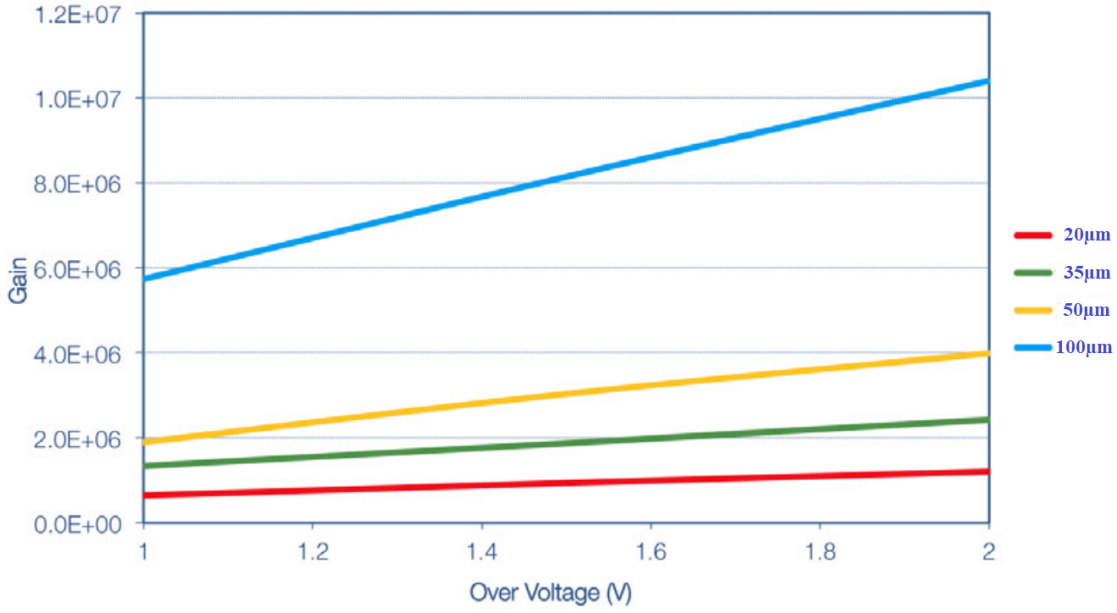


Figure 37. Gain increases with increase in overvoltage and microcell size (20 µm, 35 µm, 50 µm, and 100 µm) [53]

5.3.5 Dynamic range and linearity

Optical signal range over sensor output is called the dynamic range of a given SiPM. The relation of incident photon N_{ph} and number of fired microcells N_{fired} is described by a relation [48]

$$N_{fired}(M, V, \lambda) = M (1 - \exp(-PDE(V, \lambda) \cdot N_{photon} / M)) \quad (34)$$

where

N_{fired} = number of microcells fired

N_{photon} = number of incident photons

M = total number of microcells

PDE = photon detection efficiency

Different sizes microcells (1 mm, 3 mm, 6 mm) SiPM's response is shown in the figure 38. It is clear from the figure that for lower counts of photons, the response is linear. However, for large number of incident photons, the sensor response deviate for the linearity. The reason for this deviation is that more microcells offer a larger dynamic range. In general, a SiPM show linearity up to level about 70 % of SiPM range, as shown in the figure 39 [48].

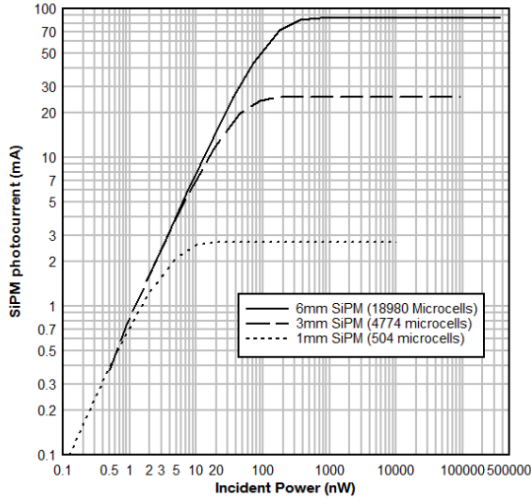


Figure 38. The SiPM response for different microcells (1 mm, 3 mm, 6 mm). The response is linear for lower count of photon, or more incident photon with more microcells [48]

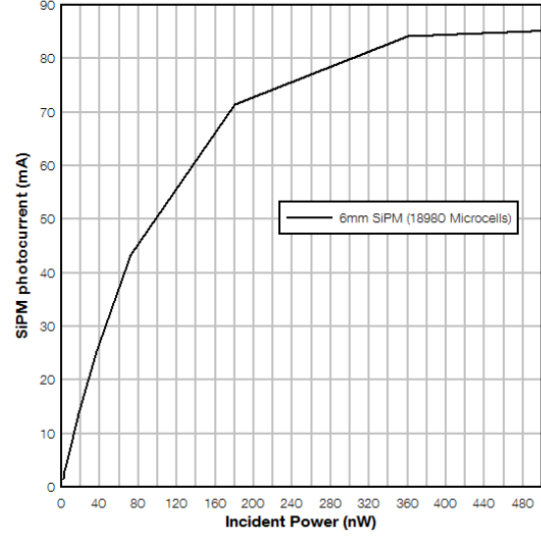


Figure 39. A relationship between incident power and photocurrent for 6 mm SiPM. The response is linear up to 70 % of SiPM range. [48]

5.3.6 Noise

The unwanted and superimposed signals are called noise. The noise in the SiPM arises due to three main phenomena, i.e. dark counts, cross-talk, and after-pulsing. Dark count is classified as primary noise and correlated noise includes cross-talk and after-pulsing. [79]

Dark Counts: In a SiPM, the avalanche process is initiated by two phenomena. In the first scenario, an incoming photon excites electrons to trigger the avalanche process. Apart from that, the thermal excitation of electrons also generates a secondary avalanche. Signals generated in this way are called dark counts. Signals generated by both ways give the same signal profile and are distinguishable. The primary noise source in a SiPM arises due to dark count rate. Therefore, a higher value of dark count rate in SiPM is considered a disadvantage. Photomultiplier tubes dark count rate lies in the kHz range while SiPM lies in the MHz region.

The dark count rate is SiPM's active area, over-voltage and temperature dependent factor. Overvoltage and temperature dependence of dark count rate (DCR) is

described by [80] using the following relation.

$$\text{DCR}(V_{ov}, T) = A \cdot (V_{ov}, V_0) \cdot \left(\frac{T}{298}\right)^{3/2} \cdot e^{-((E/2k_B T) - E/2k_B \cdot 298)} \quad (35)$$

where

V_{ov} = overvoltage

T = absolute temperature in K

A = dark rate to overvoltage ratio at room temperature i.e. 298 K (25 °C)

E = band gap energy of silicon = 1.1 eV

k_B = Boltzman constant = $1.381 \times 10^{-23} \text{ JK}^{-1}$

A higher temperatures mean a higher thermal excitation rate of carriers, resulting a higher probability of secondary avalanche initiation. Hence, dark count rate increases. A lower operating temperature can reduce this problem significantly. For example, a $\sim 10^\circ\text{C}$ raise in temperature can double the dark count rate and a decrease of $\sim 10^\circ\text{C}$ make it half [40]. Over-voltage and temperature dependence is illustrated in figure 40a and 41b, respectively.

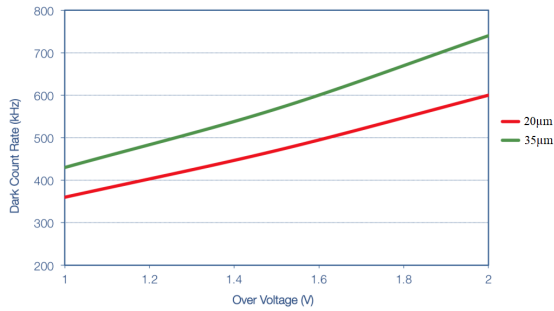


Figure 40. 1 mm SiPM's dark count rate (DCR) dependence on over-voltage [53]

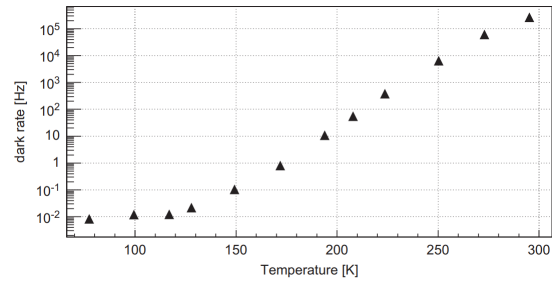


Figure 41. Temperature dependence of dark count rate for 400 pixel SiPM at constant overvoltage (2.5 V). [81]

Cross-Talk: Besides the primary noise, the other noise factor that affects the performance of a SiPM is cross-talk. There might be a chance of secondary photon emission during an avalanche process. These secondary emitted photons initiate an avalanche process in the neighbouring cell. This process is called cross-talking. The extent of cross talk depends on bias voltage, dead spaces between the active area, and pixel size. For a higher bias voltage, the probability of more charge carriers

production increases due to the avalanche process, also increasing the cross-talk rate. On the other hand, the probability of avalanche-generated photons reaching a neighbouring pixel increases with a smaller pixel size [82]. Cross-talk can be reduced by introducing opaque trenches between the microcells. A prominent reduction from the level of 20 % - 30 % can be reduced to 1 % - 2 % [83].

After-Pulse: Another correlated noise type is after-pulsing. Silicon crystal structure contains impurities in it. Charge carrier produced by avalanche can be trapped into it. A time-delayed release of these charges carrier can produce a secondary delayed avalanche. The time delay range vary from nanoseconds to microseconds. The probability $P_{AP}(t)$ for an after pulsing signal occurrence is described by [58] as,

$$P_{AP}(t) = P_t \cdot \frac{\exp(-t/\tau_t)}{\tau_t} \cdot P_T \quad (36)$$

where

P_t = trap capture probability

τ_t = trap lifetime

P_T = avalanche triggering probability

For a shorter time period t , the generated signal will be smaller than the 1 p.e. signal (signal generated by one absorbed photon). But, for a larger delay time t , same height signal (1 p.e.) can be produced resulting a fake signal. There are several factors that increase the probability of after-pulsing signals. A large number of available charge carriers or more defects/traps due to production malfunction will increase the probability of after-pulsing. Similarly, a bigger cell area will offer more trap spaces to charge carriers. In addition, a higher overvoltage, greater capacitance from bigger cell size, and extended trap time due to cold temperature will also boost up the after-pulsing.

6 General characteristics of detectors

The performance of a detector system is governed by several parameters such as energy resolution, timing, detection efficiency, pulse-shape discrimination, quantum efficiency, dead time etc. Some of these parameters are discussed in this section.

6.1 Sensitivity

Sensitivity is one of the important parameters of any detector. It tells about the capability of a detector to produce a usable signal for studied radiation types and energies. No single detector is capable of detecting all types of radiation. Instead, every detector is sensitive to a certain radiation type and usually has a certain detection limit. Above that limit, the detector does not work, produces an unusable signal, or decreases the detection efficiency. The detection sensitivity of a detector for different types of radiation is dependent on many factors [22].

- Mass of the detector
- Reaction cross section
- Sensitive area protective material
- Defects responsible for noise

6.2 Response time

Response time is another important parameter of a detector. It is defined as the time taken by a detector after absorption of incident radiation. A detector is considered to have a good timing if output signal formation is quick with a sharp pulse. The duration of signal is the period in which a second signal can not be registered due to insensitivity of detector or pile pile up effect. This limits the detector count rate and contribute to the dead time of detector [22].

6.3 Dead time

Many detectors are not capable of detecting a new event immediately after a radiation detection. This may be because there is a certain reset time of the detector (or data acquisition), or because the signals are too close to each other to be distinguished. The time the detector system is incapable to detect an event, is called dead time. Dead time is usually expressed as percentage of true time. There exist always a probability of a true event loss due to random nature of radioactive decay. For a high counting rate, the dead time loss can be severe and accurate measurement require some correction factor [9].

6.4 Pulse shape discrimination

No detector can detect all types of radiation simultaneously. However, a detector is preferably capable of effectively discriminating between α , β , and γ radiations. This discrimination is usually based on the shape of signal. In comparison with glass and inorganic crystalline solids, plastic scintillators are more sensitive to heavy charged particles even with $Z = 1$. However, the sensitivity of each detector system is different and depends on the material used. For example, amber is the least sensitive plastic detector capable of detecting fission fragments with $Z > 30$. On the other hand, the most sensitive plastic detector is PADC (polyallyldiglycol carbonate), also known as CR-39 [84].

6.5 Pulse height distribution

For a radiation detector operating in pulse mode, each radiation encounter generate a pulse height which gave information about generated charge. The performance or information about incident radiation of the detector is retrieved from pulse amplitude distribution. Pulse amplitude information is provided by differential pulse height distribution. The pulse height distribution is given as $\frac{dN}{dH}$, the differential which is essentially the density of pulse height. In practice, the pulse height distribution is produced by dividing the "binning" detected pulse heights to finite channels with equal width ΔH and counting them. There should always be a sufficient amount of channels that the spectrum shape can be followed.

6.6 Energy resolution:

The capability of a detector to distinguish between two closely related energies is called energy resolution. The most common definition of resolution is based on the full width at half maximum (FWHM) of the peak (see figure 42). FWHM resolution is defined as the ratio of FWHM to the number of channel of peak centroid H_0 [9].

$$R = \frac{\text{FWHM}}{H_0} \quad (37)$$

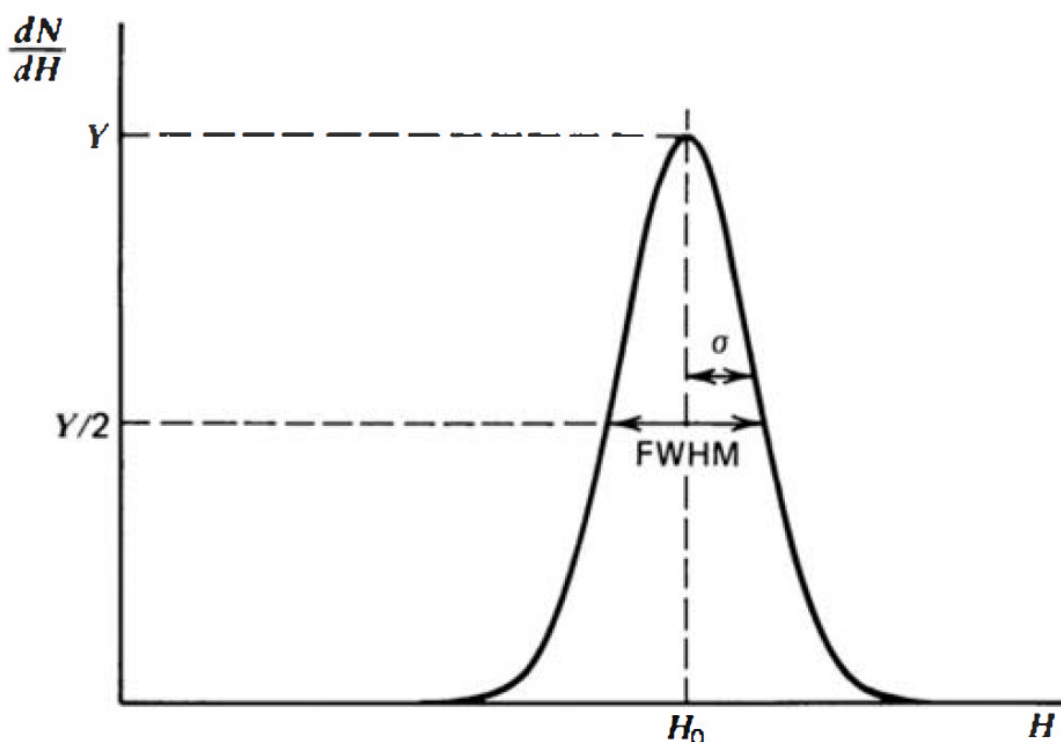


Figure 42. Detector resolution definition using FWHM. The value of FWHM is 2.35σ for a Gaussian shape peak with standard deviation σ [9]

The choice of FWHM resolution as a favoured measure of resolution comes from the simple fact that if two peaks lie closer than FWHM to each other, there is no valley between the peaks. If they are located further than FWHM from each other, there is a valley between the peaks. A sharp energy resolution peak, gives better sensitivity and detection capability to distinguish between nearly lying energies of radiations as illustrated in figure 43. Being a ratio, energy resolution is dimensionless and expressed in terms of percentage. For scintillation detectors used in gamma spectroscopy, the energy resolution ranges 3 - 4 % [9]. For semiconductor detectors

the resolution is significantly better ($< 1.0\%$).

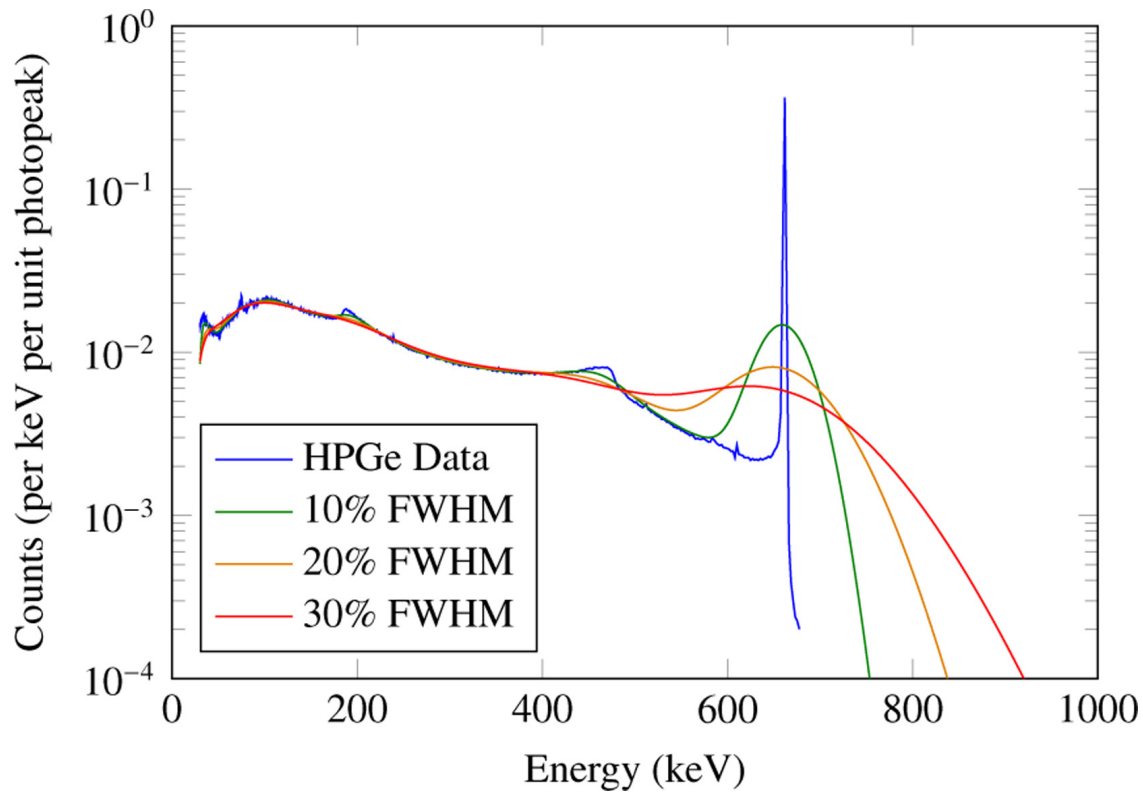


Figure 43. Effect of detector resolution on the gamma ray spectrum of ^{137}Cs . HPGe represents a measurement with a semiconductor detector. Other spectra represent scintillation detectors with different resolution. Figure from [85].

6.7 Detection efficiency

The detection efficiency of a detector is a measure of response to different radiation types and energies. The efficiency of ionising radiation detectors depends on

- The type of the radiation (charged particle such as alpha, beta or heavy ion; gamma ray; or neutron)
- The properties of the detector material
- The geometry of the measurement, which includes the size and distance of the detector from the source of radiation, as well as the spatial distribution of the source (point-like, areal, or voluminous)

6.7.1 Impact of the radiation type

The response of the detector to charged particles is the most straightforward. A charged particle moving through detector material causes ionisation (gas filled detectors) or electronic excitations (scintillation and semiconductor detectors). The amount of ionisation, molecular excitations or electron-hole pairs is almost linearly proportional to the amount of energy transferred to the detector material. The intrinsic efficiency of the detector to charged particles is 100 %: every particle hitting the detector produces a signal.

Detection of gamma rays or neutrons requires more complicated interaction. Neither gamma rays nor neutrons do not ionise material nor excite electrons. Instead, their interaction with detector material produces energetic charged particles that produce ionisation and excitations. The neutrons interact only in nuclear collisions. The most efficient energy transfer to charged particle is received in a head-on collision with a proton. The moving proton then interacts with the detector material. The interaction of the gamma rays is even more complicated.

The gamma photon can cause photoelectric effect. It can Compton scatter from an electron. Very energetic gamma photon can trigger a formation of electron-antielectron pair. In each case, it is a moving electron (or antielectron) that interacts with the detector. It is therefore possible that a gamma ray or neutron goes through the detector without interacting it: the detectors intrinsic efficiency is thus less than 100 %. In addition, the detector signal response to the initial energy of the neutrons or the gamma photons is not linear, because the energy transfer to the charged particle strongly depends on the initial energy of the neutrons or gammas as well as the details of the interaction process.

6.7.2 Impact of the detector material

Radiation detection is based on the energy transfer of the detected radiation to the detector material. Thus, light (low Z , small A) detector materials favor the observation of neutrons. High electron density favors the detection of gamma rays and charged particles. High electron density is associated to the high density in general. Therefore, the inorganic scintillators, in particular such as BGO, are most appropriate to gamma ray detection. Neutrons are best detected with scintillation materials with a high concentration of hydrogen, which typically means organic

scintillators. An additional requirement is the pulse shape discrimination to be able to distinguish between neutrons and gamma rays, which are typically emitted from the same radiation sources.

Many of the neutron discrimination capable scintillation materials are derivatives of trans-stilbene ($C_{14}H_{12}$, trans-1,2-diphenylethylene), why they tend to be both highly flammable and highly carcinogenic. The best choice for a detection material for alpha and beta detection mostly depends on whether alpha-beta discrimination is needed. If only counting is required, thin organic plastic scintillators are often the most affordable and flexible solution. The stopping power of organic scintillators for electrons [86] is sufficient to keep the required detector thickness for calorimetric measurements reasonably small at electron energies up to a few MeV (see figure 44).

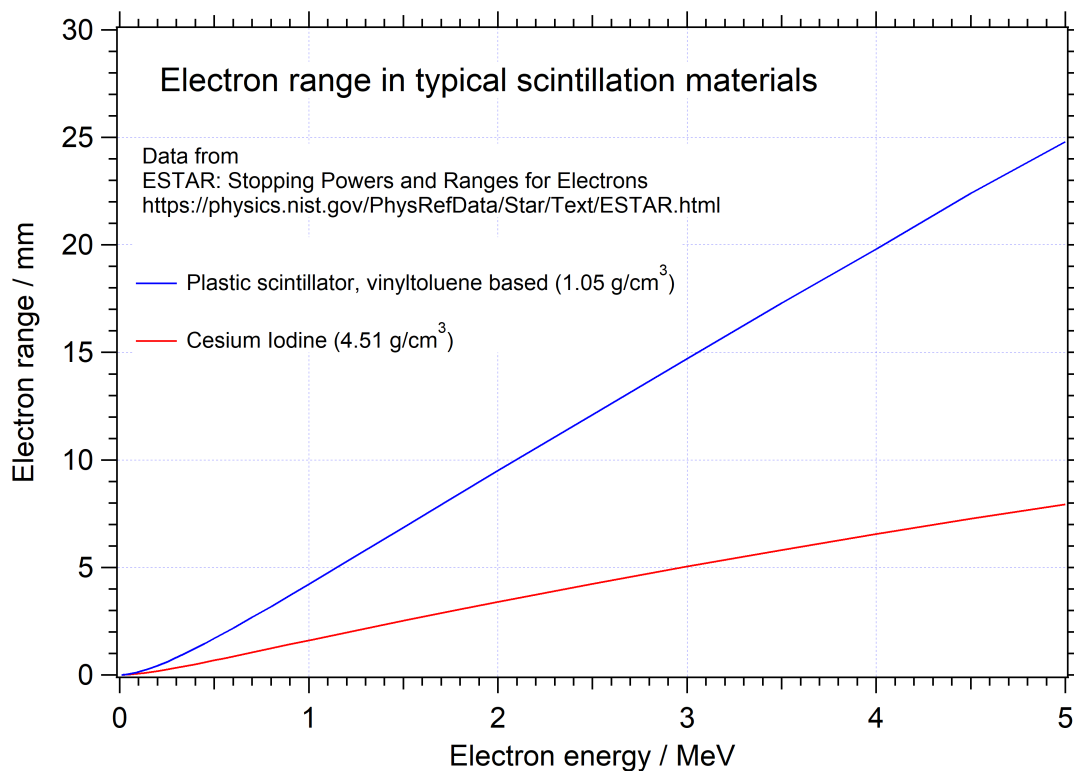


Figure 44. The electron range dependence on its energy in CsI and in a typical polyvinyltoluene [87] based plastic scintillator

6.7.3 Impact of the measurement geometry

The largest effect to the radiation detection efficiency is due to the geometry: position of the detector with respect to the source of radiation. This is called geometrical efficiency. All the absorbing material, including the possible casing of the detector (vacuum case of a germanium detector, window of a gas-filled detector) and the body of a voluminous radiation source (eg. a contaminated land vole) can be considered as a part of the measurement geometry and thus influences on the geometrical efficiency.

In addition to the geometrical efficiency ϵ_{geo} , every detector has an intrinsic efficiency ϵ_{int} . Together these two contribute to the absolute or total efficiency ϵ_{tot} .

The geometrical efficiency describes, which fraction of ionising radiation quanta impinges the active part of the detector. If possible, it is advantageous to make the measurement in a pointlike source geometry, where the geometry can be approximated by the solid angle in which the source "sees" the detector. More mathematically, solid angle of the detector is the area two-dimensional projection of the detector on surface of the source-centered sphere, divided by the area of this sphere. A thin areal source can be considered to consist of many point-like sources. For a uniform areal source the geometrical efficiency can in principle be calculated analytically by integration. For non-uniform and/or voluminous sources accurate determination of the geometrical efficiency requires Monte Carlo simulation. This is also because in addition to the detector, the radiation interacts with the absorbing material as well.

According to Knol [9], **intrinsic efficiency** ϵ_{int} of a detector is defined as the ratio of recorded pulses to the number of radiation quanta incident on detector.

$$\epsilon_{int} = \frac{\text{No. of recorded pulses}}{\text{No. of radiation quanta incident on detector}} \quad (38)$$

The intrinsic efficiency depends on physical parameters (distance, angle, thickness), extent of radiation energy (i.e. type), and detector material.

On the other hand, the **absolute or total detector efficiency** ϵ_{tot} is defined as the ratio between the number of recorded events to total number of events generated by a radioactive source.

$$\epsilon_{tot} = \frac{\text{No. of event recorded}}{\text{No. of events emitted by source}} \quad (39)$$

The absolute efficiency of a detector is dependent on the detector properties and

counting geometry (distance, angle). The product of intrinsic and geometrical efficiency will give the total efficiency. The absolute or total efficiency of the detector can be written as

$$\epsilon_{tot} = \epsilon_{int} \cdot \epsilon_{geo} \quad (40)$$

7 Experimental, materials and methods

The section starts with an overview of telescope detector purpose, followed by some details about detector system, used material in this thesis. In the second section, a detailed description of experimental detector setup will be provided.

7.1 Goal of experimental development

In this thesis work, a prototype (ΔE -E) type telescope detector based on plastic scintillators and silicon photomultipliers was built and tested. Using the “ β -energy gating” technique, one can distinguish ^{90}Y decays from other types of decay. In addition, the performance of silicon photomultipliers (SiPM) was also tested.

The main goals of this work were:

- To build a prototype detector system that will allow on-site testing and will reduce the sampling time for researchers
- To investigate the suitable plastic scintillator for detector system
- To be able to distinguish between γ rays and β particles
- To critically analyze the performance of silicon photomultiplier (SiPM)

7.2 Description of telescope detector

The goal of the development work was to construct a telescope detector consisting of ΔE and E detectors operating in coincidence mode. Figure 45 shows the schematic arrangement of the telescope detector.

An electron from the beta decay passes the ΔE detector causing scintillation. Beta electron is eventually stopped in the E detector, producing scintillations with the remaining of its energy. These scintillation pulses are literally simultaneous. In contrast, a γ ray from the sample usually passes through the ΔE detector without interaction and leaves energy only in the E detector. Also, a gamma ray entering the telescope detector elsewhere than the studied source, interacts more likely with

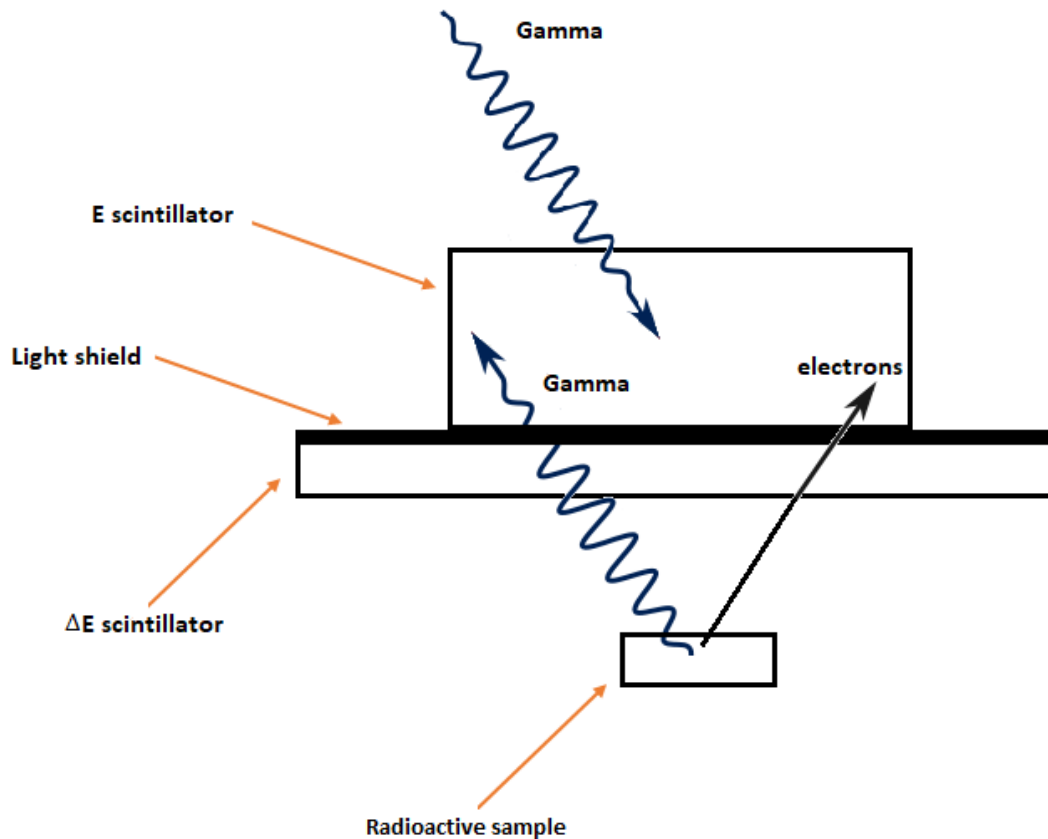


Figure 45. Schematic arrangement of the telescope detector. See text for details

the E detector, without generating a coincident signal in ΔE detector. Coincident signals in both ΔE and E detectors indicate a beta particle from the source.

It is however worth of noticing that a more detailed analysis shows that gamma ray can in some circumstances produce a coincident event. The most typical gamma ray from the sample is 662 keV gamma from ^{137}Cs . The developed telescope is meant to detect ^{90}Sr in environmental samples. Both ^{137}Cs and ^{90}Sr are nuclear fission products, thus sample containing ^{90}Sr usually contain ^{137}Cs as well. The most common interaction between 662 keV gamma ray and any material is Compton scattering, as illustrated in figure 18.

Compton scattering of a gamma ray produces a Compton electron and a scattered gamma ray. If scattering takes place sufficiently close to the surface between the scintillators, the scattered electron can be detected in both ΔE and E detectors. Another possibility is that after the Compton scattering in the ΔE detector, the scattered gamma ray is detected with the E detector. The amount of 662 keV gamma

rays that interact with the ΔE detector depends on the thickness Δx of the detector. The attenuation of gamma ray intensity follows Beer-Lambert law just as described earlier in equation 10. The reduction of the intensity and the fraction F of γ -rays that interact with the detector is given by equation 11 and 12 respectively. For gamma rays that move perpendicular through the ΔE detector, Δx is the thickness of the detector. For gamma going through ΔE in an angle, Δx is more.

In any case, detection of ^{90}Sr is not only based on the discrimination of gamma rays but also "beta energy gating". The beta spectrum of ^{90}Y , the child of ^{90}Sr , extends up to 2 MeV. Energy threshold of the events around 0.5 - 0.6 MeV removes the most of the few false events.

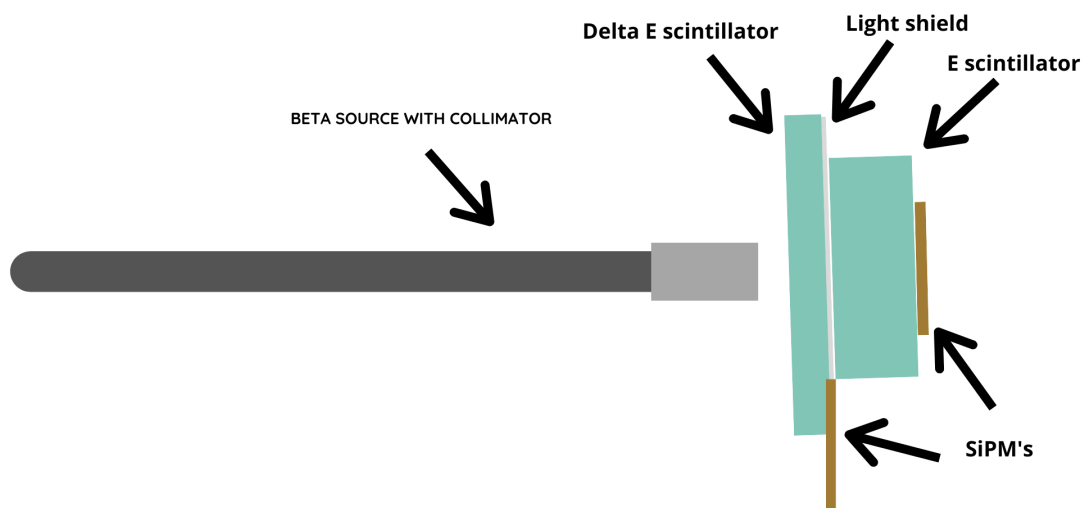


Figure 46. SiPM arrangement with scintillators

From the geometry of the telescope detector, it is obvious that the silicon photomultiplier of the E detector needs to be attached behind the detector. An obvious choice is to attach the SiPM in the middle of E detector to guarantee most equal light collection all over the detector. The geometry dictates that the SiPM from the ΔE detector needs to be attached at the side of the detector, as shown in the figure 46. The first research questions were thus:

- How uniform the light collection from the detector is?
- How large the possible differences are?
- Is there a way to minimize them?

7.3 Material

The detail of used material is as follows.

7.3.1 Plastic scintillators

Precut plastic scintillators were ordered from the Scionix Holland [88] for constructing the prototype of the β telescope. Two types of Eljen's plastic scintillators [89] were employed: EJ-200 for the E detector (thick detector) and EJ-212 for the ΔE detector (thin detector). The properties and dimensions of the scintillators are given in the table 4. As seen from the table, the properties of EJ-200 and EJ-212 are quite similar. The use of the two different scintillators is thus not obvious but merely follows the recommendation of the Scionix Holland representative.

Table 4. EJ-200 and EJ-212 plastic scintillators properties [34]

Properties	EJ-200	EJ-212
Polymer base	Polyvinyltoluene	Polyvinyltoluene
Refractive index	1.58	1.58
Temperature range	-20°C to 60°C	-20°C to 60°C
Light output (% Anthracene)	64	65
Rise Time (ns)	0.9	0.9
Decay Time (ns)	2.1	2.4
Pulse width, FWHM (ns)	2.5	2.7
Density (g/cm^3)	1.023	1.023
Light Attenuation length (cm)	380	250
Wavelength of max. emission (nm)	425	423
Scintillation efficiency (Photons/1 MeV e^-)	10,000	10,000
Ordered scintillator dimensions (Diameter \times Thickness)	75 mm \times 10 mm 25 mm \times 10 mm	85 mm \times 1 mm 35 mm \times 1 mm

7.3.2 Silicon photomultipliers (SiPM's)

Silicon photomultipliers (SiPM's) are devices that convert weak light signals to measurable electrical signals. They are pretty sensitive and are widely used in nuclear and particle physics experiments. The basic construction, working principle, and parameters affecting the performance of a SiPM is discussed in detail in section 5. In addition, the electronic board and circuit schematics of used SiPM is illustrated in figure 47. A total of two SiPM's were used for each detector system. One was attached to thicker and one with a thinner scintillator.

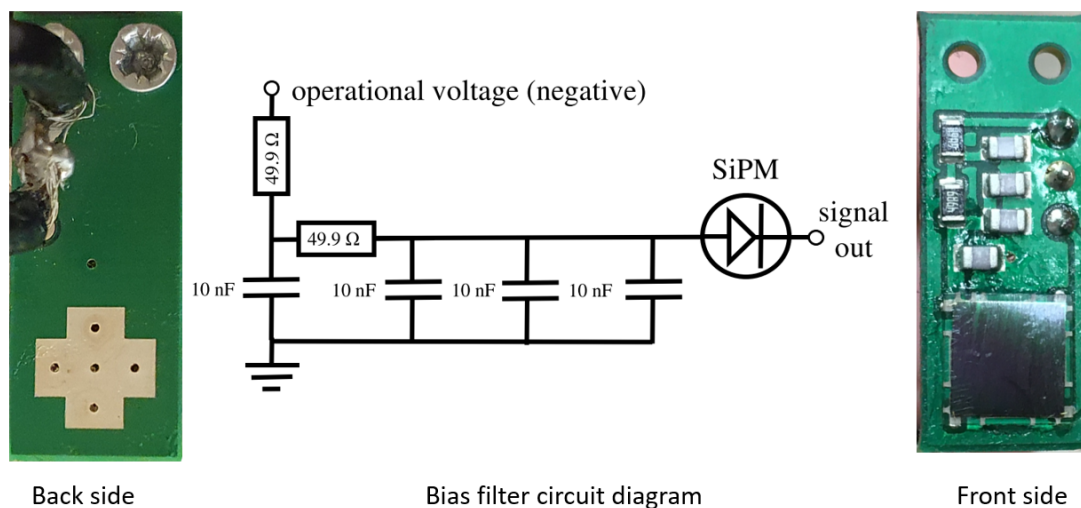


Figure 47. Front and back side of SiPM with bias filter circuit schematics

7.3.3 Radioactive sources

The test involved use of radioactive sources to produce the scintillation. Three radioactive sources ^{241}Am , ^{90}Sr , ^{137}Cs from the Accelerator Laboratory of the University of Jyväskylä (JYFL) were used for α , β , and γ radiations as shown in the figure 48. In addition, for energy calibration purposes, few reading with ^{60}Co radioactive source were also taken. The detail of used radioactive sources is given in table 5



Figure 48. α , β and γ radioactive sources from JYFL

Table 5. Used radioactive sources with their activity

Source	JYFL code	Activity (Bq)	Ref. date	Description
^{241}Am	JYFL-103	3,70E+04	1.1.1989	Point source; α emitter
^{90}Sr	JYFL-103	3,70E+04	1.1.1989	Point source; β emitter
^{137}Cs	JYFL-103	3,70E+05	1.1.1989	Point source; γ emitter
^{60}Co	JYFL-019	1,20E+04	30.3.2006	Point source on 25 mm diameter disc; γ emitter

7.3.4 Collimators

A radioactive source emits particles or photons isotropically. To be able to study light collection from a particular location in the detector, the radiation need to be localised sharply to this region. A device used to narrow down a beam of particles (radiations) is called a collimator. The first collimator used in tests was a piece of aluminum with a hole. This collimator was sufficient as such, but it was very difficult to align properly with the essentially point-like radiation source. Since a set of radiation sources (JYFL-103) had threads for attaching to the storage shielding, a new collimator utilising these threads was designed and produced in the department's mechanical workshop. The newly designed collimator was quite handy, as it can be put onto the radioactive source. The used collimator can be seen in figure 49

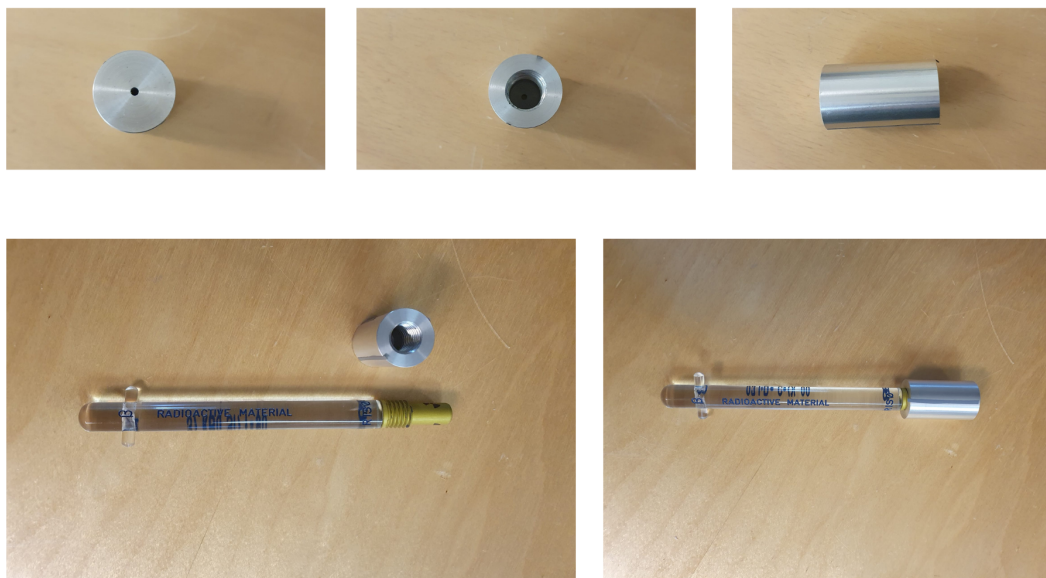


Figure 49. The final version of radiation collimator

7.3.5 Degraders

Plastic sheets of 1 mm of thickness were also used in this thesis work as energy degraders. The ultimate goal in the project is to be able to quantitatively measure the beta activity of a voluminous source. Degraders were used to mimic the slowing down of β particles travelling through matter, and also change the ^{90}Y spectrum for detector energy calibration purposes.

7.3.6 Boxes as light shield

In order to avoid any external light to enter the light-sensitive SiPM's, two plastic boxes were used. The primary shield was a plastic box in which the experimental setup was placed, as shown in figure 54a. The connection cables for signals were punch through the box. Since, specially the cable feed-through from the first box were not necessarily fully light tight, the primary shield was covered by a larger black plastic container put on the top of it. The used boxes are shown in figure 52.

7.3.7 Voltage Power Supply

BK Precision 9174 dual channel DC power supply was used to regulate the power supply, as shown in figure 50. A complete product description of the power supply can be found in reference [90]. The scintillators are quite sensitive, therefore the voltage reading must be less than 30 V. One must be careful while using the power supply. The experimental apparatus box must be closed before switching the power supply **ON** and must be turned **OFF** before opening the box.



Figure 50. Voltage power supply used in this work

7.3.8 Data Acquisition and LINUX system

Data acquisition system containing preamplifier, amplifier, and STUK DAQ system was used to collect the data as shown in the figure 51. This data was then transferred to another operating system. A LINUX based operated system with Grain software was used to analyze the collected data.

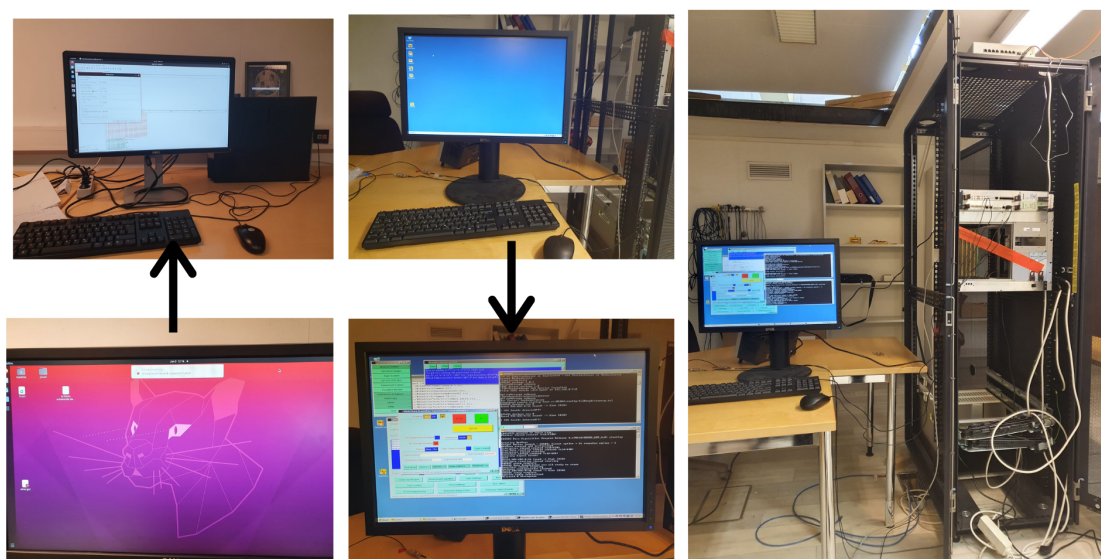


Figure 51. Data acquisition system

Other used material include oscilloscope (for signal analysis), aluminum sheets to cover the scintillators, optical couplant, methanol and ethanol for scintillator cleaning purposes. The used material in this research are shown in the figure 52.

7.4 Experimental detector setup

Basically, the experimental setup consists of scintillators, silicon photomultipliers, and data acquisition system. During the course of the detection setup development, various arrangements to hold the detector and radiation sources were employed. Schematic and actual detector and measurement setup is shown in figure 53, and 54. The detector system was mounted on a hand-made made of polystyrene foam (packaging foam) as shown in figure 55. Two SiPM's were used in this work. Thicker

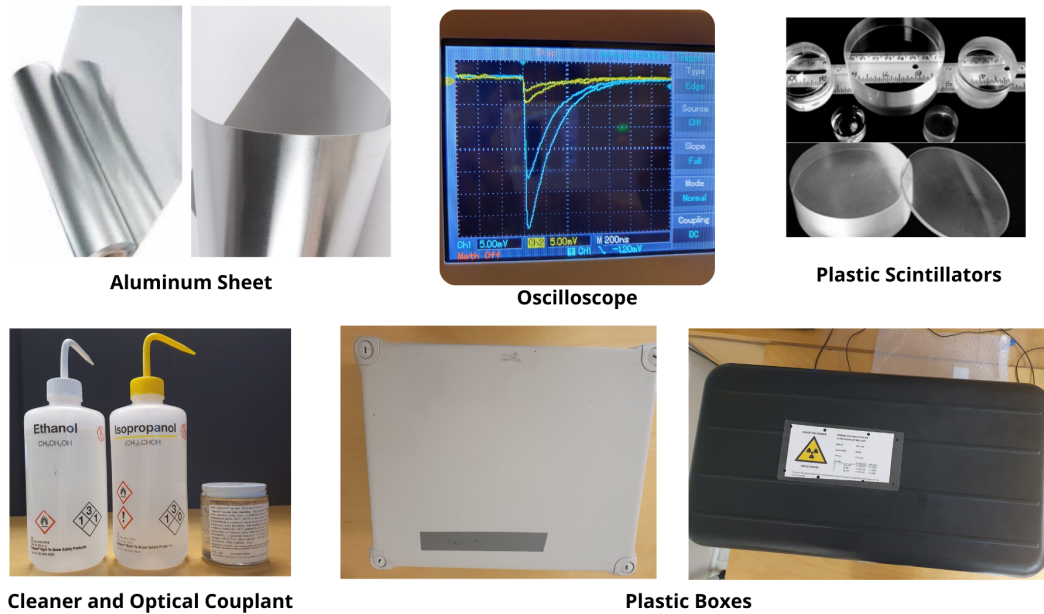


Figure 52. Other material used in this thesis

scintillator SiPM was used at the middle point, while the other SiPM (for thinner scintillator) was used at the corner. Position sensitivity measurements were taken using different scintillators. In the progress of development, the results were more refined and closer to the targeted goal.

In order to ensure the accuracy, position and angle sensitivity measurements were assisted by using a scale and protractor in the experimental setup. An iron stand was used to keep the radio source mounted onto a fixed position. As the SiPM's are light-sensitive, therefore in order to avoid light contact, the experimental setup was placed in a closed box as light shield. In addition, an extra box was also placed above. The readings were taken with and without the collimated radioactive sources (α , β , and γ). In the last few measurements, data were also taken using plastic degraders (1 mm each) in the front of the radioactive sources.

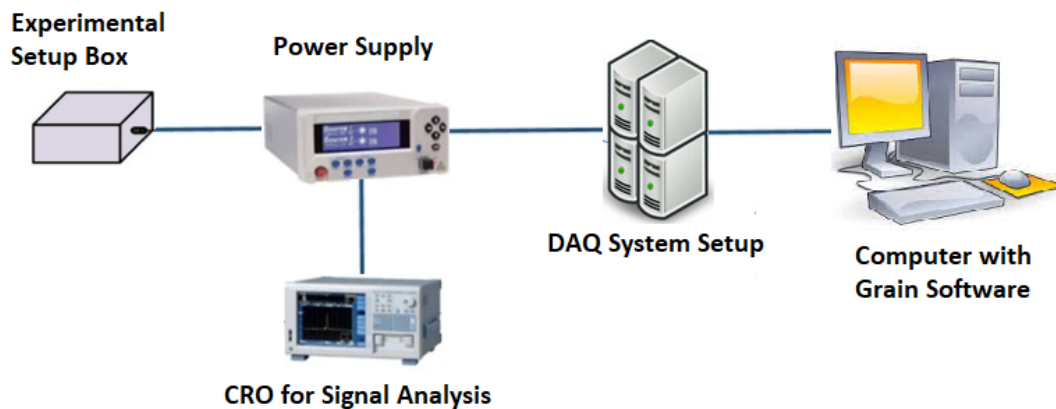


Figure 53. Schematic diagram of experimental setup

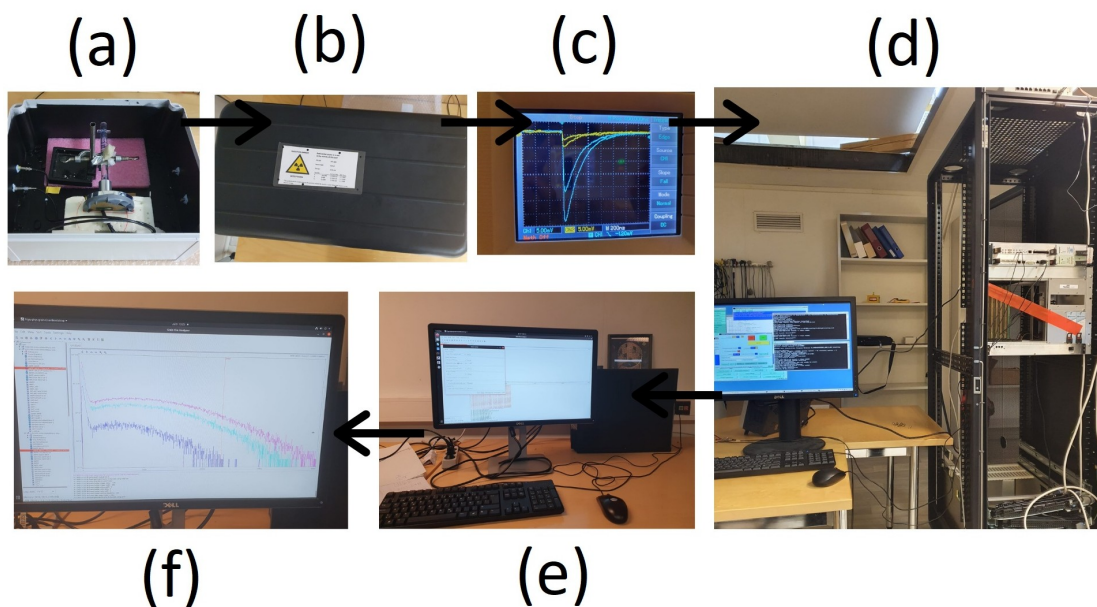


Figure 54. Real experimental setup (a): Detector setup in box, (b): Covering box for detector setup, (c): Oscilloscope to observe signal, (d): DAQ setup, (e): LINUX system with GRAIN software, (f): β Spectra on computer screen

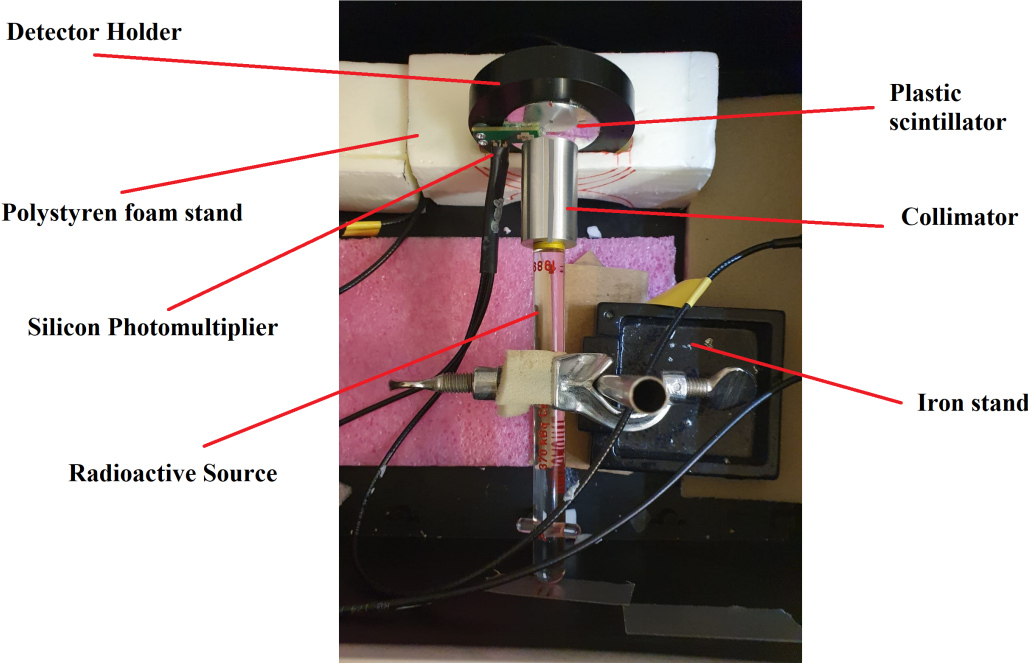


Figure 55. Experimental setup in light shielded box

8 Development of the telescope detector

Before building the actual telescope detector, the light collection efficiency of each scintillator was tested separately. The main scintillator was the thicker one, which was irradiated for alpha and beta sources with and without the collimator. Position and angle response measurements were taken to check the effect of geometry of the sample. The angle measurements were also utilised for the energy calibration of the thin ΔE detector. Firstly, the scintillators were tested using α , β , and γ sources without the collimator, as shown in the figure 57. Tests were continued with the collimated β source that allowed aiming the beta particles on a specific point of the detector. Tight collimator also allowed to specify angle at which beta particles hit the detector.

8.1 Prototype telescope detector

The first research question was, how uniform the light collection from the detector was? It is not obvious that the scintillation light produced at different places in the detector is collected to the SiPM with equal efficiency. In particular, the ΔE detector was expected to show this effect, since SiPM must be positioned close to the edge of the detector as shown in figure 46. In the E detector, SiPM was always positioned in the center.

The scintillator detectors were prepared by covering them with a reflecting polymer foil. This foil is better than 98 % reflective 3M Enhanced Specular Reflector, layered polymer film, whose most common application is as back reflector of LCD displays [91]. The 3M foil helps keeping the photons in scintillator, until they find their way to SiPM. In the beginning, the SiPM was attached to $6 \times 6 \text{ mm}^2$ opening cut in the 3M polymer foil just by the adhesion of the optical grease that also provided a surfaceless optical contact between the scintillator and the SiPM. It turned however out that the weight of signal cables were enough to twist the optical connections loose. After that, more secure ways to clamp the SiPM's to the detector were adopted. Ultimately, the SiPM electronic board was attached with a screw to a detector holder

made of PMMA (polymethyl methacrylate) plastic as illustrated in figure 56.

Figure 57 shows the pulse height spectrum of uncollimated ^{241}Am (α), $^{90}\text{Sr}/^{90}\text{Y}$ (β) and ^{137}Cs (γ) sources (JYFL-103) of 75mm x 10mm EJ-200 scintillator plastic. The beta spectrum of ^{90}Y extends to 2.28 MeV. The beta electrons generate directly

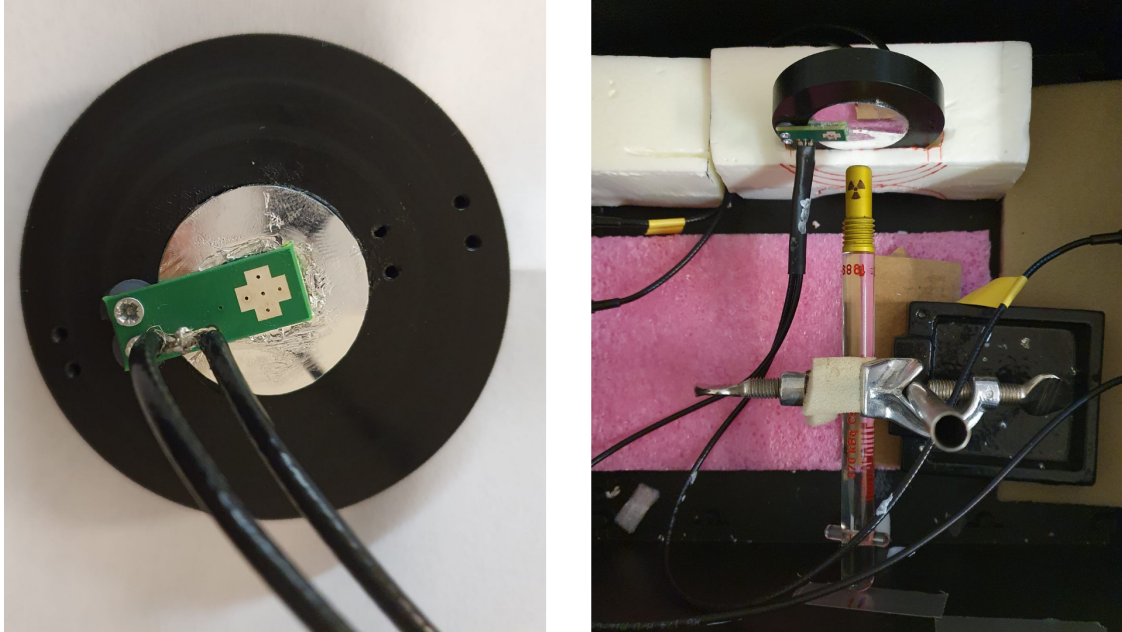


Figure 56. Final prototype detector setup. Left: SiPM attached on the back of the E detector. Right: Detector irradiated with radioactive source. Note that the ΔE SiPM is attached on the front face of the detector

scintillating excitations with the highest efficiency (figure 14). 2 MeV electrons will produce 20,000 scintillations in the plastic. The gamma rays are not directly producing any scintillations but transfer energy to the Compton electrons. The high energy edge of the gamma spectrum corresponds to the ~ 480 keV Compton edge of ^{137}Cs . 662 keV γ -ray will produce ~ 5000 scintillations. The ^{241}Am α -particle energy is 5.485 MeV and 5.442 MeV (the strongest lines). The scintillation response to alpha particles of EJ-200 is lower than that of electrons (see Figure 14). ~ 5.5 MeV particles will produce only ~ 3000 scintillation photons in the plastic. In general, the position of α , β , γ spectra in figure 57 seems to correspond to this light output.

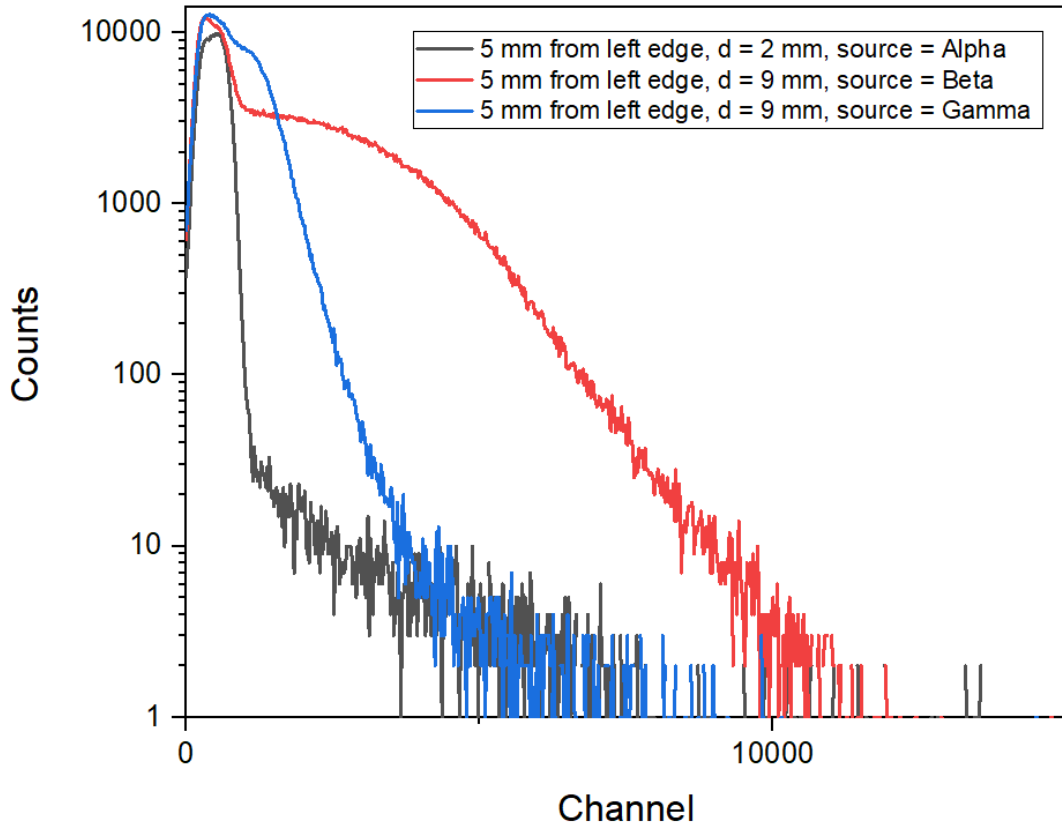


Figure 57. Measurements with EJ-200 (75 mm \times 10 mm) scintillator with α , β and γ sources. Here d is the distance between radioactive source and scintillator.

8.2 Light collection efficiency

The light collection efficiency was tested with α and β sources. The radiation was pointed to the certain location by collimating the radiation as illustrated in figure 58. In principle, the use of alpha source has certain advances. The alpha particles have short range in the plastic. The place of interaction is well defined. The range of α -particles is however so short that they did not penetrate the 3M polymer foil. Small holes were punched in the reflective foil to allow α particles enter the detector. Furthermore, as discussed above, the light production in the Eljen plastic scintillator per MeV is lower with α particles than with electrons. In practice, the weakest alpha signals were so close to noise that their usefulness for analysis was limited. It might have also been that the data acquisition was not properly adjusted to the alpha induced scintillation pulses. With the beta sources, sufficient data could however be collected. 1 MeV electron passing perpendicularly 1 mm thick ΔE detector leaves

~ 0.2 MeV which corresponds to ~ 2000 scintillation photons, as clear from figure 14.

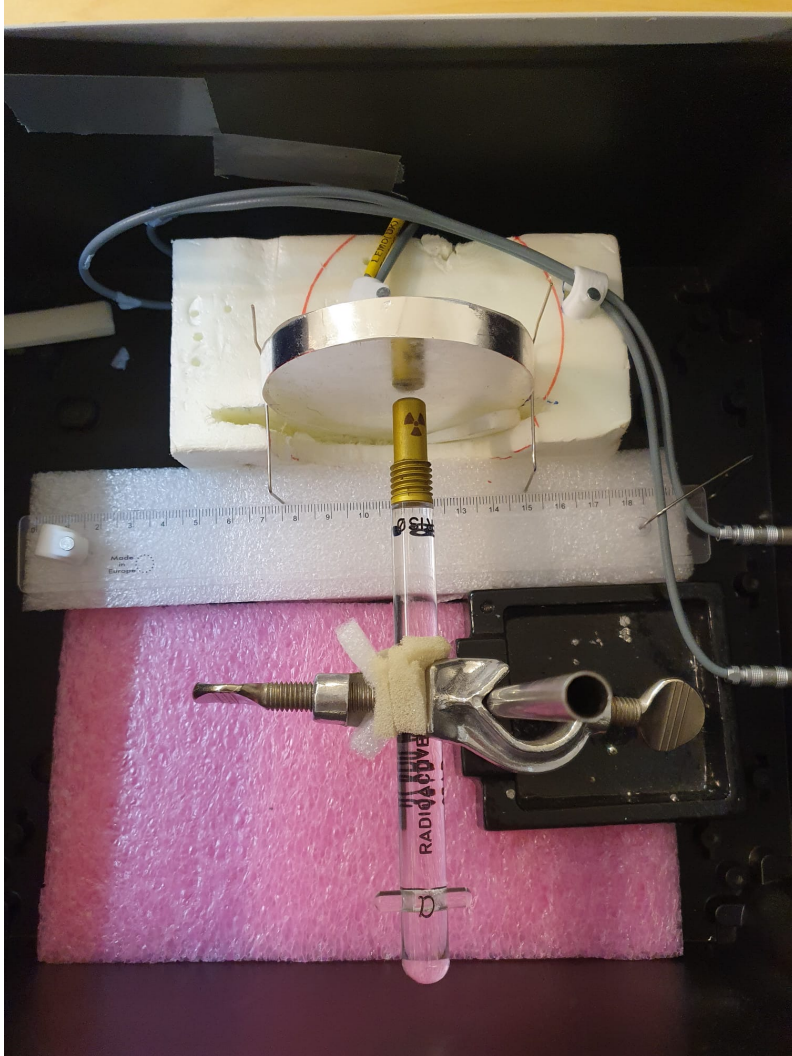


Figure 58. 75×10 mm scintillator experimental setup

8.2.1 Light collection efficiency of 75×10mm EJ-200 scintillator

Figure 59 shows the pulse height distributions of collimated beta radiations at different locations on the detector. The SiPM was attached at the center of the back face of the scintillator. The detector was irradiated along its diameter at 5, 15, 25 and 35 mm front the detector edge on both sides of the SiPM, whose position was in the center 37.5 mm from both edges as shown in figure 58. The first observation is that the detected signal height distribution from symmetric irradiations (e.g. at

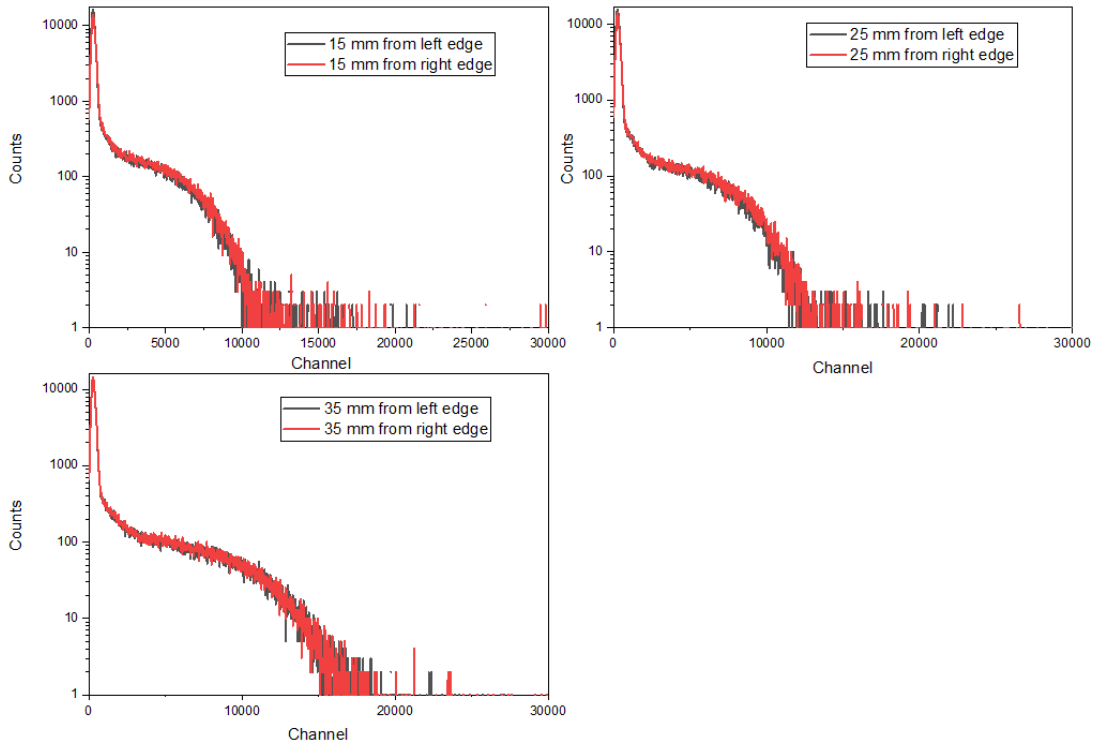


Figure 59. Position sensitivity measurements using collimated β for EJ-200 (75 mm \times 10 mm)

15 mm from the left edge and at 15 mm from the right edge) are almost identical as depicted in figure 59. With small effort it is seen also that in each case the shape of the spectrum is similar. This is in fact what to expect. The beta spectrum of $^{90}\text{Sr}/^{90}\text{Y}$ source is the same in every irradiation. Every irradiation produces the same distribution of scintillation counts. The light collection from a certain point is expected to be a constant. The height of every detected pulse is lowered by a certain factor, but the shape of their distribution remains the same. This is shown in the figure 60. In the top panel, the pulse height spectra from irradiations at 5, 15, 25, and 35 mm from the detector are shown. Since it is seen from the figure 59 that spectra of symmetric position irradiations are identical, they have been added up to increase the counting statistics.

In the central panel the spectra have been adjusted firstly by stretching them in the x-direction and scaling in the y-direction. The lowest panel is the same as the central panel but to reduce the staggering of data points, it uses a sliding average, producing a smoothed "interpolation" through the data. The maximal light collection is observed at 35 mm from edges, which position is already in front

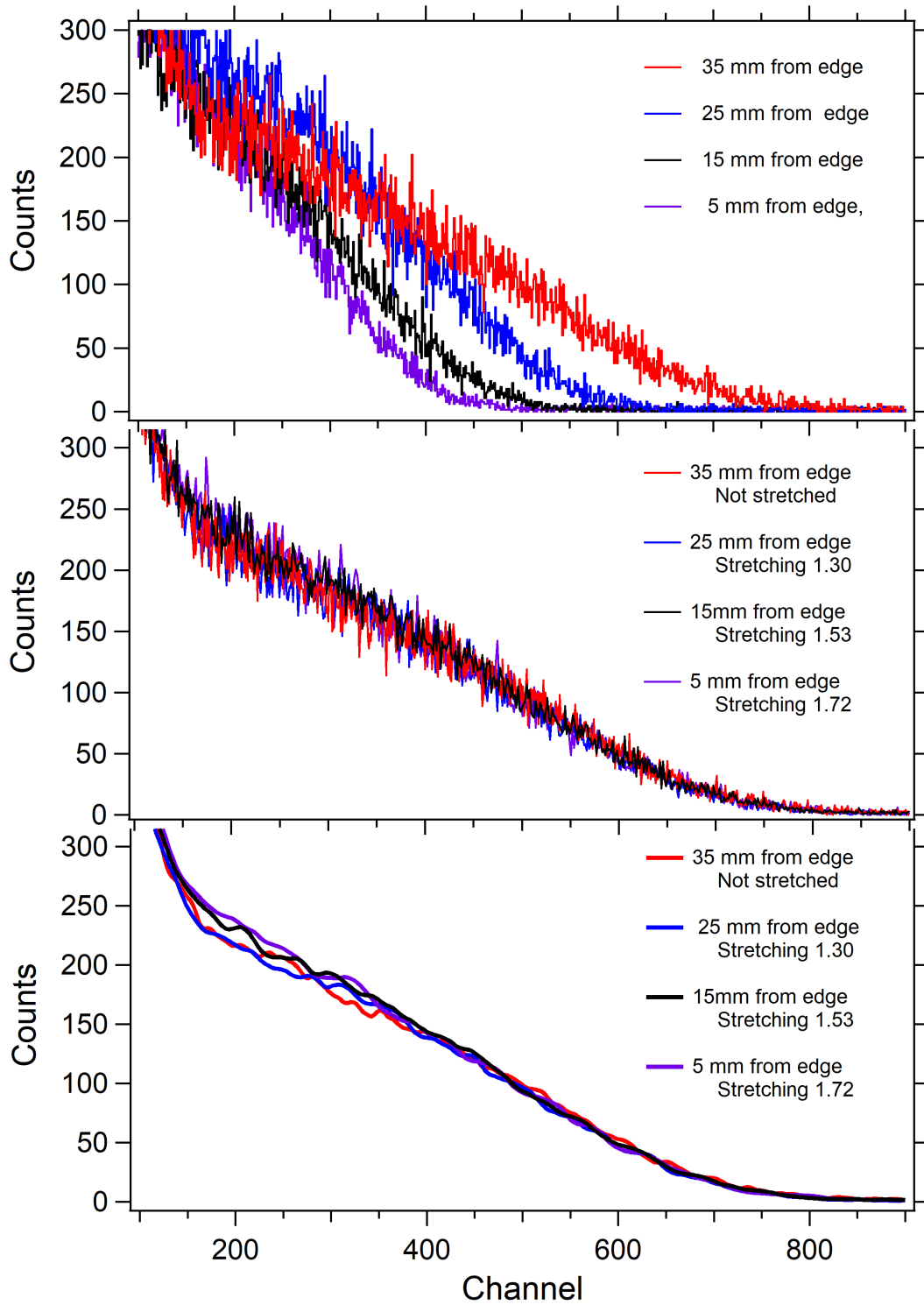


Figure 60. Finding the light collection efficiency by the shape-fitting technique (by stretching the spectra on the top of each other). See text for details.

of the SiPM. The absolute light collection from this point is not known, expect that it is less than 100 %. In the stretching the other beta spectra, this was however used as a normalisation. The light collection efficiency with respect to 35 mm from the edge is the inverse of the stretching factor needed to match the shapes. A similar technique quoted as shape-fitting technique, has been in fact used in the past to determine the beta endpoint energies [92].

The inverse of the stretching factors are shown in figure 61. The reference point in the figure is moved to the center of the detector so that zero is put at 37.5 mm from the edges. The data points are reflected on the both sides of center of the scintillator. The fitted curve with its 1σ (68 %) confidence bands on the data points is also shown. The fitting function is a Lorentzian on the top of constant background without no other particular basis than it fits better than e.g. a Gaussian shape. The fit can be considered a smooth interpolation through the data points.

8.2.2 Light collection efficiency of the 25×10 mm EJ-200 scintillator

The light collection efficiency of smaller 25 mm diameter EJ-200 detector was studied in a similar way as the 75 mm detector. The beta particles from $^{90}\text{Sr}/^{90}\text{Y}$ source were directed at 5 and 10 mm from the edges, as well as at the center of the scintillator, 12.5 mm from the edges. The shape fitting analysis was performed in a similar manner as for the 75 mm diameter scintillator. The results are shown in figure 62.

The light collection of the 25 mm scintillator is not quite as symmetric with respect to the detector edges as that of 75 mm diameter scintillator. The data points can however nicely fitted using the same fitting function. It might be that the SiPM has not been precisely in the center in these measurements, which however can not be checked any more.

Somewhat surprisingly, the light collection efficiency "peak" is narrower than in the 75 mm scintillator, and the relative light collection efficiency falls to 60 % at the edges of both scintillator. There is however indication, displayed in figure 63 that the absolute light collection efficiency of the small detector would be significantly higher than that of the large one. Figure 63 displays the same $^{90}\text{Sr}/^{90}\text{Y}$ spectra of beta particles impinged close to the edge of the detector. Both positions have 65 % relative light collection efficiency, as compared to the center of the detector. Although there can be small differences in the signal amplification and in the transparency of the surface between the scintillator and the SiPM, the average pulse height from 25 mm

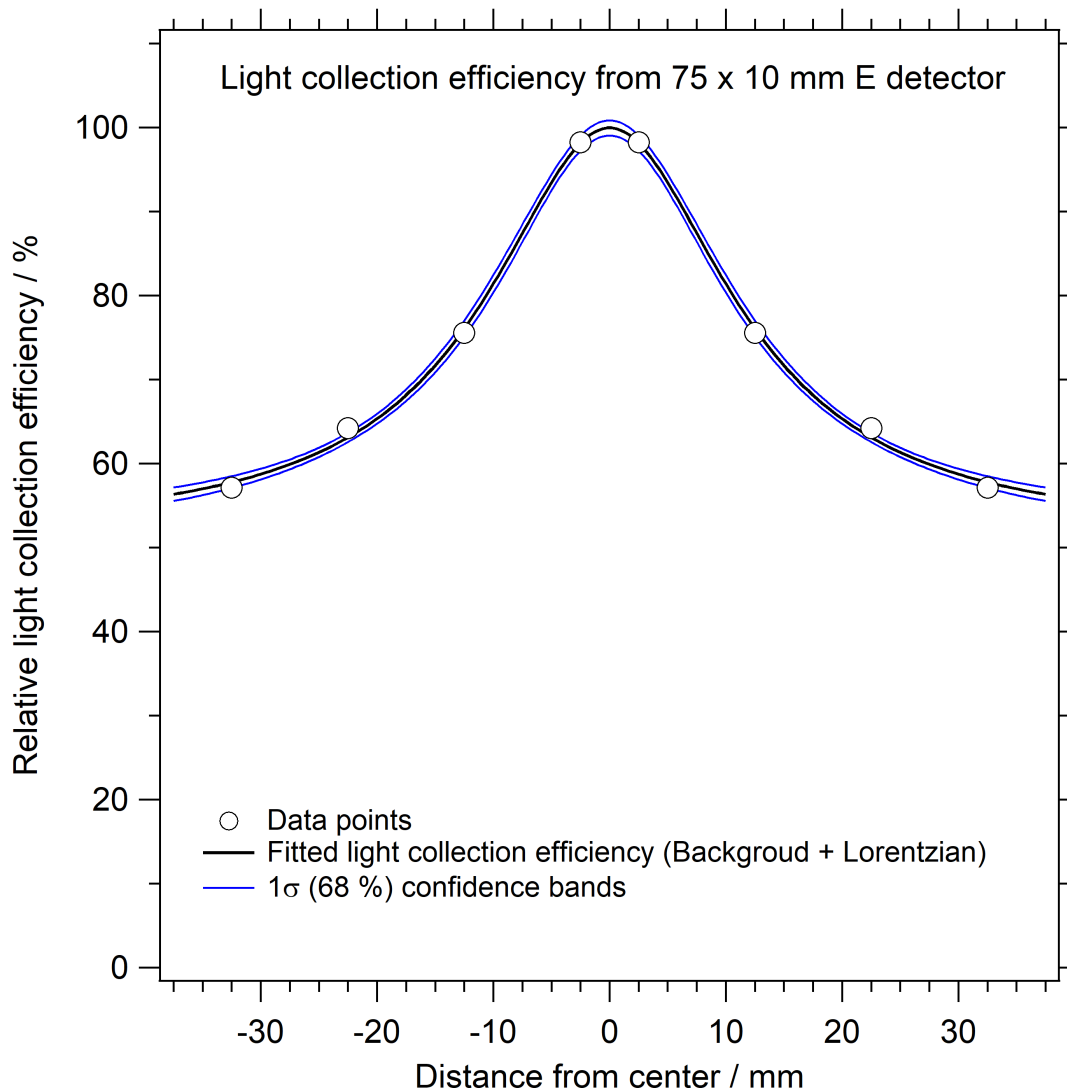


Figure 61. Light collection efficiency from 75×10 mm E detector

scintillator is about three times higher. It is very plausible it is due to much more effective overall scintillation light collection from the small scintillator.

8.2.3 Light collection efficiency of the 85×1 mm EJ-212 ΔE scintillator

The light collection efficiency of the 1 mm thick ΔE detector sheet was investigated in principle in the same manner as that of the thicker scintillator. The detector was radiated along its diameter at 5, 10, 15, 25, 35 mm from both edges, and at the center 42.5 mm from the edges.

1 mm of plastic is enough to entirely stop ^{241}Am alphas. Exposing the detector to ^{241}Am alphas should produce ~ 3000 scintillations per α -particle. The beta particles

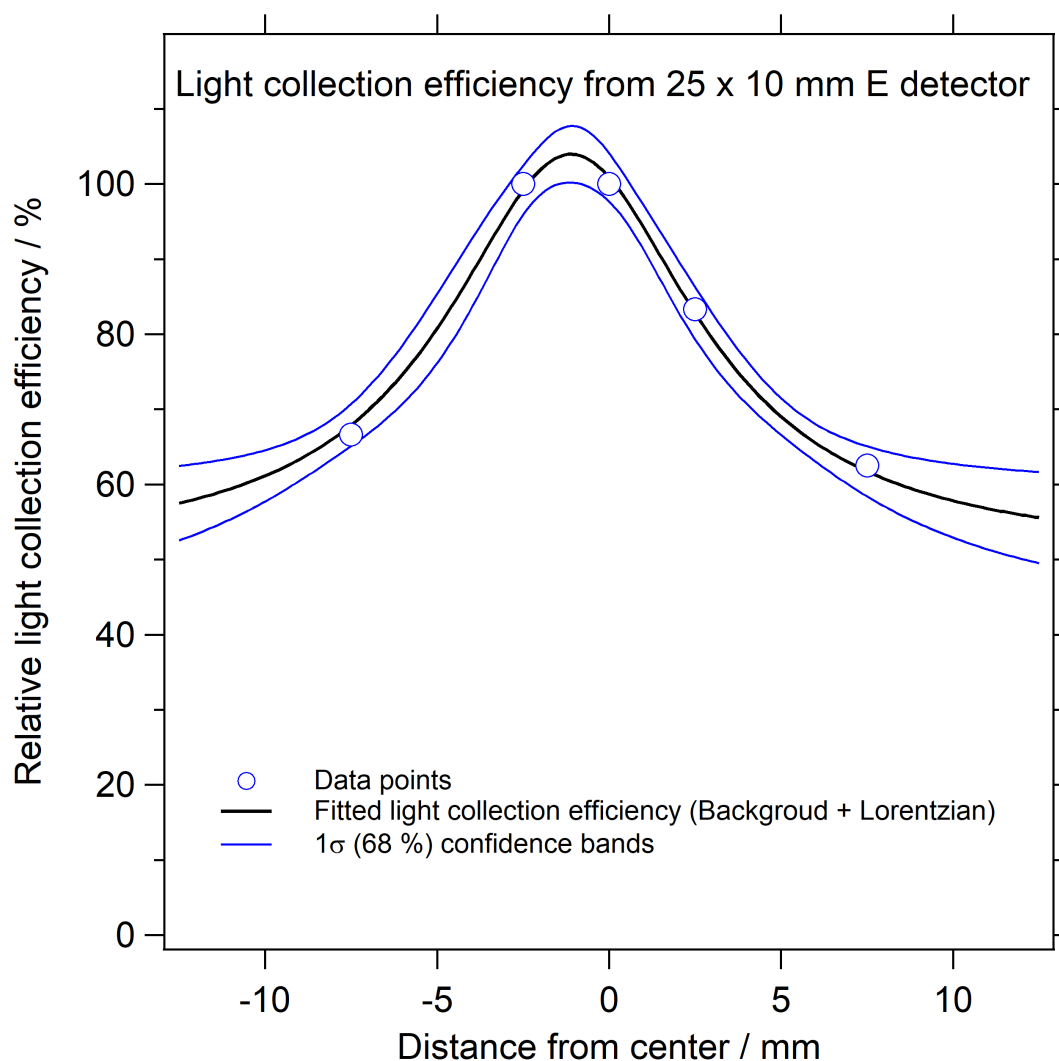


Figure 62. Light collection efficiency from 25 \times 10 mm E detector

instead mostly penetrate 1 mm scintillator. The energy left in 1 mm of scintillator material depends on the beta particle energy. Initially 1 MeV betas leave ~ 0.2 MeV to the scintillator. The energy of the betas from $^{90}\text{Sr}/^{90}\text{Y}$ source however ranges from 0 to 2.28 MeV. Combining the knowledge of the initial shape of the beta spectrum and the energy transfer to the detector it is possible to mimic the actual shape of the electron transmission peak. The penetrating beta particles are expected to leave minimum 0.2 MeV in the detector. This means ~ 2000 scintillation photons per a beta particle. The average is higher since all the betas do not go straight through the detector. The collimation allows some small angle at which the betas can hit the detector, making the trajectory longer and increasing the deposited energy. In addition, the less energetic betas leave more than 0.2 MeV to the detector, generating

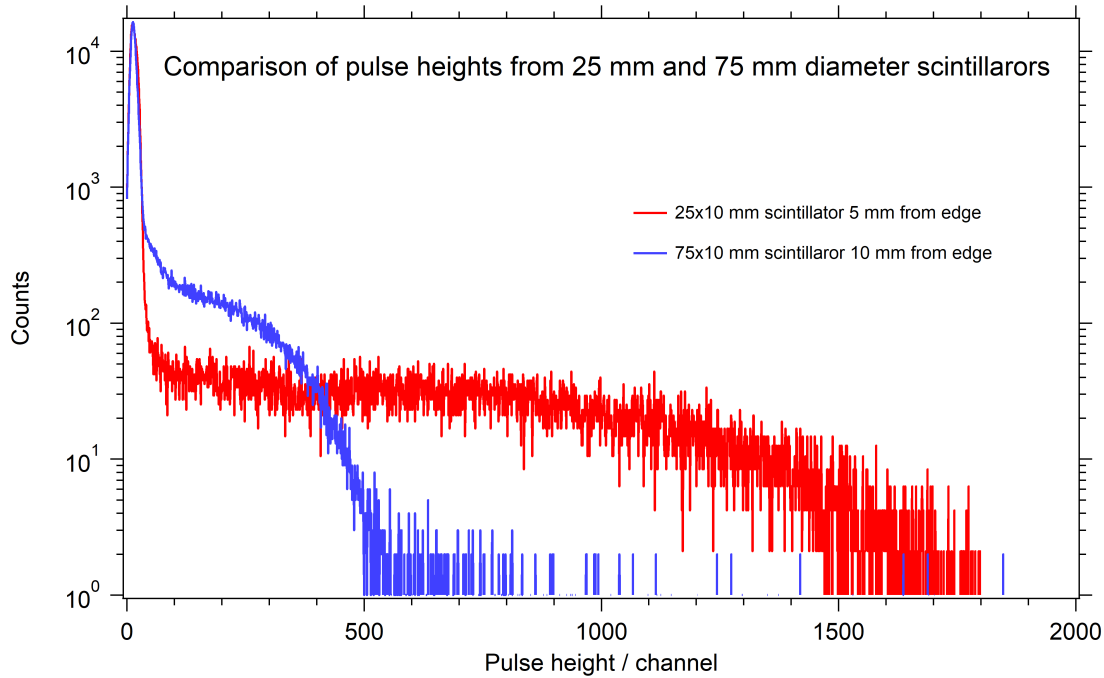


Figure 63. Comparison of pulse height from 25 mm and 75 mm diameter scintillator. The measurement positions have the same relative light collection efficiency of 65 % with respect to the 100 % in the middle of each detector.

the high energy tail of the peak. However, the low energy edge of the transmission peak should locate around 0.2 MeV.

Figure 64 shows the recorded transmission beta spectra at 5, 15, 25, 35, 50, 60, 70 and 80 mm from the "left" edge of the detector: the SiPM was attached on the "left" side of the detector. The height of the scintillation pulses is distinguishable from the noise only for the "left" side of the detector. In addition, a clear transmission peak is seen only for the two radiations closest to the SiPM. The light collection efficiency for 25 and 35 mm radiations was deduced from the tail of these spectra. This should be compared to the pulse height distributions of the 35×1 mm ΔE scintillator (see figure 68): every spectrum has a distinguishable transmission peak. Based on the previous discussion, the location of the low energy edge of the beta transmission peak at 5 mm from the detector edge should be ~ 0.2 MeV and correspond initially to 2000 photons. The ^{241}Am alpha particles implanted in the same location should produce ~ 3000 photons. However, the entire alpha spectrum was below the low energy edge of the beta transmission peak, as seen in figure 65.

The light collection efficiency from the 85×1 mm EJ-212 scintillator is summarised in figure 66. Meaningful data points could be collected only on the SiPM side of the

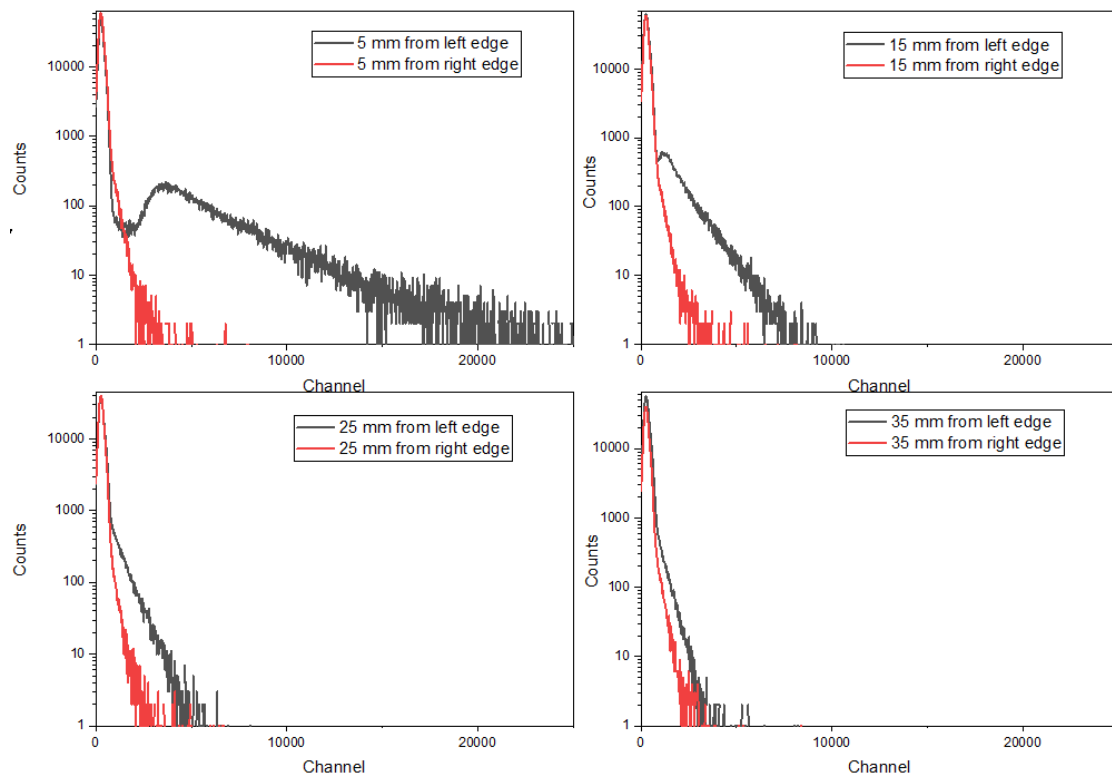


Figure 64. Position sensitivity measurements using collimated β for EJ-212 ($85 \text{ mm} \times 1 \text{ mm}$)

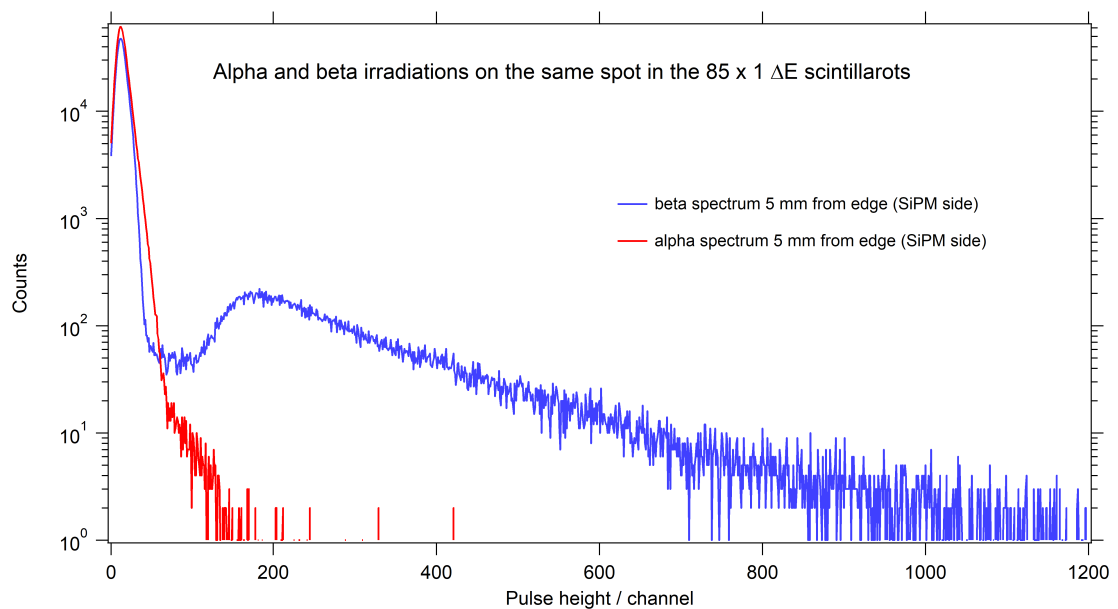


Figure 65. Alpha and beta irradiations on the same spot in the $85 \times 1 \text{ mm}$ ΔE scintillator

scintillator sheet. The data points can clearly not be fitted with a single exponential. An exponential on the top of constant collection efficiency and fit of two exponentials were found to be able to fit the data points equally well. Extrapolation to the other side of the scintillation sheet gives slightly different result depending on the fitting function. The data on the 35×1 mm scintillator (section 8.2.4) supports single exponential and a constant being the more reliable model. Even so, the light collection efficiency from the other left of the scintillator is only 15 % that of vicinity of SiPM.

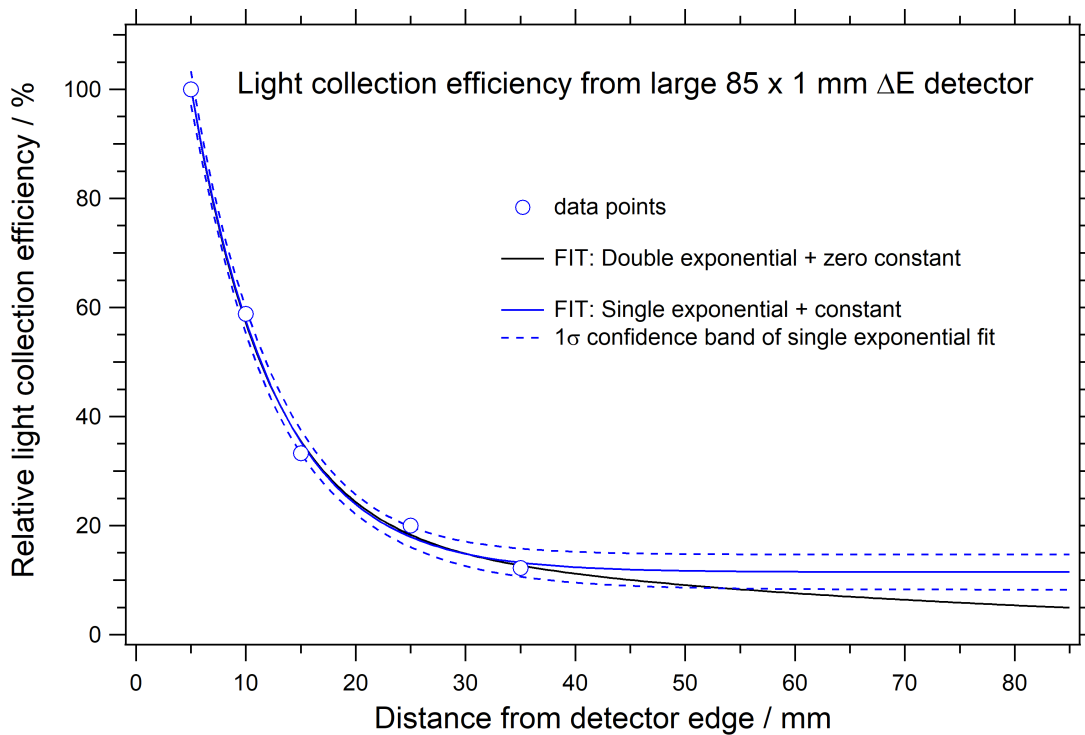


Figure 66. Light collection efficiency from 85×1 mm ΔE detector

8.2.4 Light collection efficiency of the 35×1 mm EJ-212 ΔE scintillator

The pulse height spectra from the beta irradiation on different positions i.e. 5, 10, 15, 17.5, 20, 25, and 30 mm from the SiPM side edge diameter of the 35×1 mm scintillator sheet are shown in figure 68. Unlike in the case of 85×1 mm sheet, all the pulse height spectra show a distinguished transmission peak. This allows to analyse the light collection efficiency in three ways.

1. Assuming that the transmission peak shape is constant and making a similar shape stretching as for the thick E detector

2. Determining the centroid (center of gravity) of the transmission peak
3. Determining the transmission peak maximum position

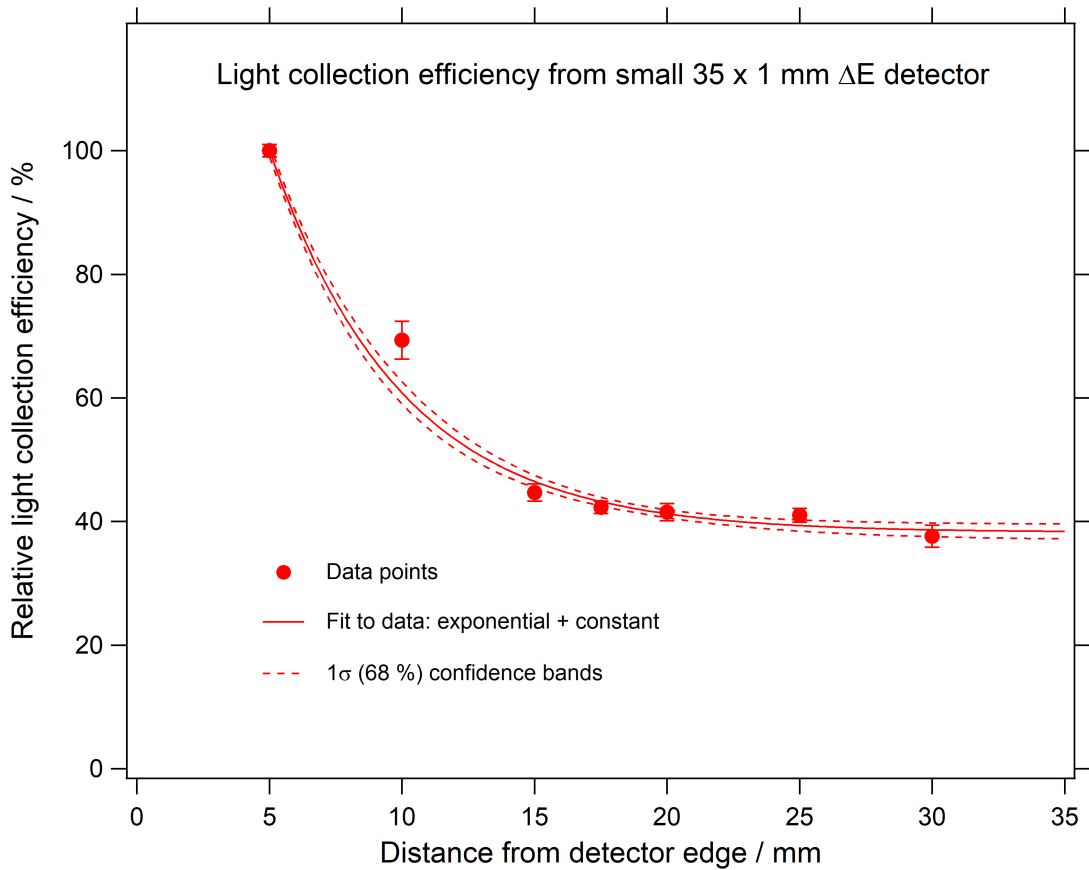


Figure 67. Light collection efficiency from small 35×1 mm ΔE detector

It turned out that all these techniques give almost identical light collection efficiencies. Method 1 and 2 gave almost perfect arrangement, the transmission peak maximum position giving systematically 5 % higher values. The average efficiencies of all techniques were used for analysis. Light collection efficiencies are shown in figure 67. The data points are best fitted with a single exponential and a constant. For this basis this would be the more accurate fit for the 85×1 mm ΔE short light collection as well.

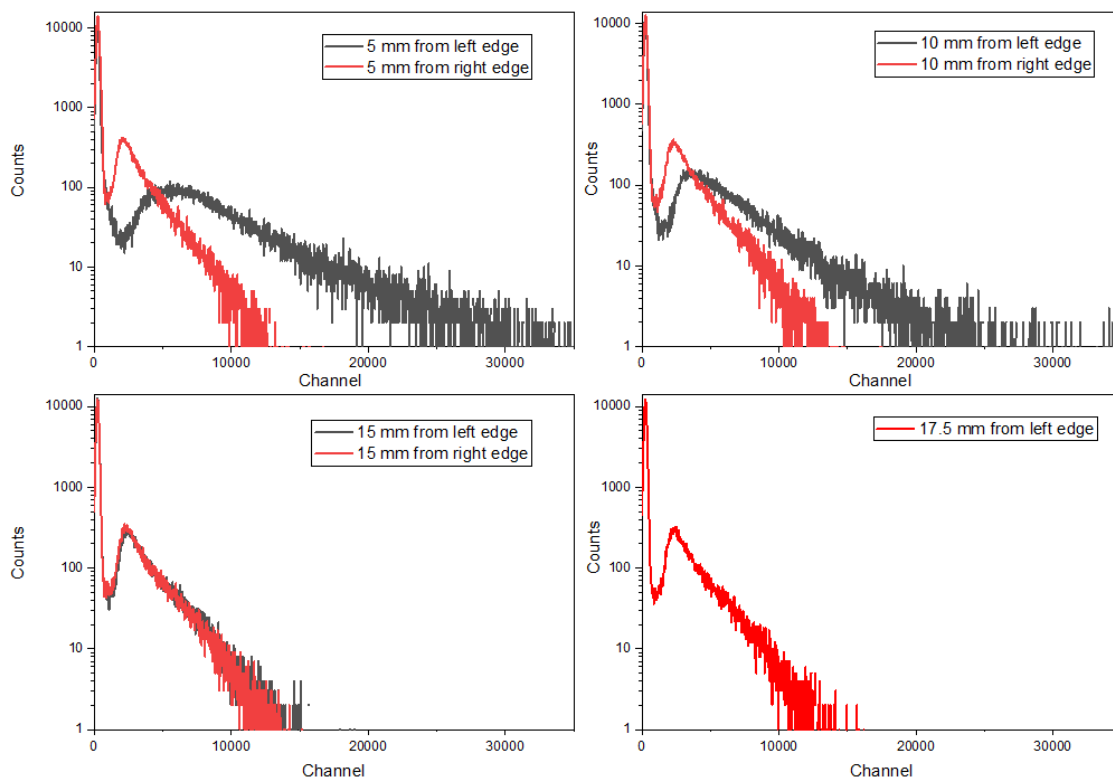


Figure 68. Position sensitivity measurements using collimated β for EJ-212 35 mm \times 1 mm plastic scintillator

8.3 Conclusions from the light collection efficiencies

The results may be summarised by that the light collection and thus the scintillator efficiency is not very uniform for any detector. It has to be however noted that the way to attach the SiPM to the scintillators is relatively crude. It could perhaps be improved using specifically designed light guides. In fact there is one common feature in all the light collection efficiency curves in figures 61, 62, 66, and 67. Light collection far from the SiPM seems to be quite constant and uniform. Close to the SiPM light collection efficiency increases exponentially but falls to the uniform level within 10 - 15 mm from the SiPM. The exception is 75×10 mm E detector where the exponential drop is slower.

The next step in the development of a telescope detector was however the choice of scintillator to be used in the prototype telescope. The main research questions of the first telescope test was:

- How well ΔE - E coincidences can distinguish between electrons and gamma rays?
- How well ΔE - E coincidences can distinguish between beta electrons from the sample and the background radiation from the environment?

Answering these questions requires building a telescope, but the test can also be performed with less uniform detector efficiency. The smaller 25×10 mm scintillator and the matching 35×1 mm ΔE detector were chosen. The main reason was that the signals from both 25 mm E and 35 mm ΔE detector were stronger than the comparable signals from the larger scintillators; in particular, the signals from everywhere in the 35 mm ΔE detector were clearly above the noise level.

8.4 Telescope detector and its energy calibration

The telescope detector prototype consisted of 25 mm diameter 10 mm thick EJ-200 scintillator plastic as E detector and 35 mm diameter 1 mm thick EJ-212 sheet as ΔE detector. The plastics were covered with M3 polymer film and attached to a holder frame made of black PMMA plastic. After the first tests an aluminium foil was added between the detectors as an additional light shield to ensure there is no cross-talk between the detectors. The SiPMs were attached in the center of the back face of the E detector and (exceptionally) on the front face of the ΔE detector.

Although in the final version the light collection will probably be on the back of the ΔE detector, the feasibility tests could be performed as well having the SiPM attached in this way, as illustrated in figure 56 right panel.

Since the light collection from ΔE and E detectors was not the same, the response of the detectors to the deposited energy was different. In the measurements, the beta particles can enter the detector in an oblique angle, which means that the energy deposit of the beta to the ΔE detector is not insignificant. The final identification of ^{90}Y decays is based on their high energy. To maximize the efficiency, the total energy deposited in both E and ΔE detectors need to be known. To be able to add up the energies, the detectors need to be energy calibrated.

8.4.1 Energy calibration of the E detector

The simplest approach from the energy calibration would have been with mono-energetic electrons. Since such a source was not easily available, the energy response was studied with radioactive sources. Two methods were applied

- Measuring the beta spectrum from a collimated source with energy degraders
- Measuring the position of the Compton edge of ^{137}Cs and ^{60}Co gamma ray source

In the first technique, the collimated beam of betas from the $^{90}\text{Sr}/^{90}\text{Y}$ source were impinged perpendicularly to the E detector. The perpendicular geometry was needed just because in the next step, 1.0 mm thick plastic sheets were added between the source and detector on by one. Having the degrader sheets perpendicular to the beam of beta particles minimises the variation of the energy loss. Figure 69 shows how the measured spectrum changes with adding the degraders. In the first spectrum there are no external degraders, it is measured however already with the telescope prototype (figure 56), so that the E detector has the 1.0 mm thick ΔE detector with the 3M polymer reflectors and a light shielding aluminium foil in between it and the collimated $^{90}\text{Sr}/^{90}\text{Y}$ sources. The highest energy electrons are estimated to be slowed down by ~ 230 keV in the ΔE detector and by ~ 230 keV in each degrader sheet. The calculated energies are listed in table 6.

The beta spectrum is continuous, but the lowering of endpoint energy could be used for energy calibration. The endpoint channel of the beta spectrum is not straight-forward to determine, since the beta spectrum approaches to zero gradually,

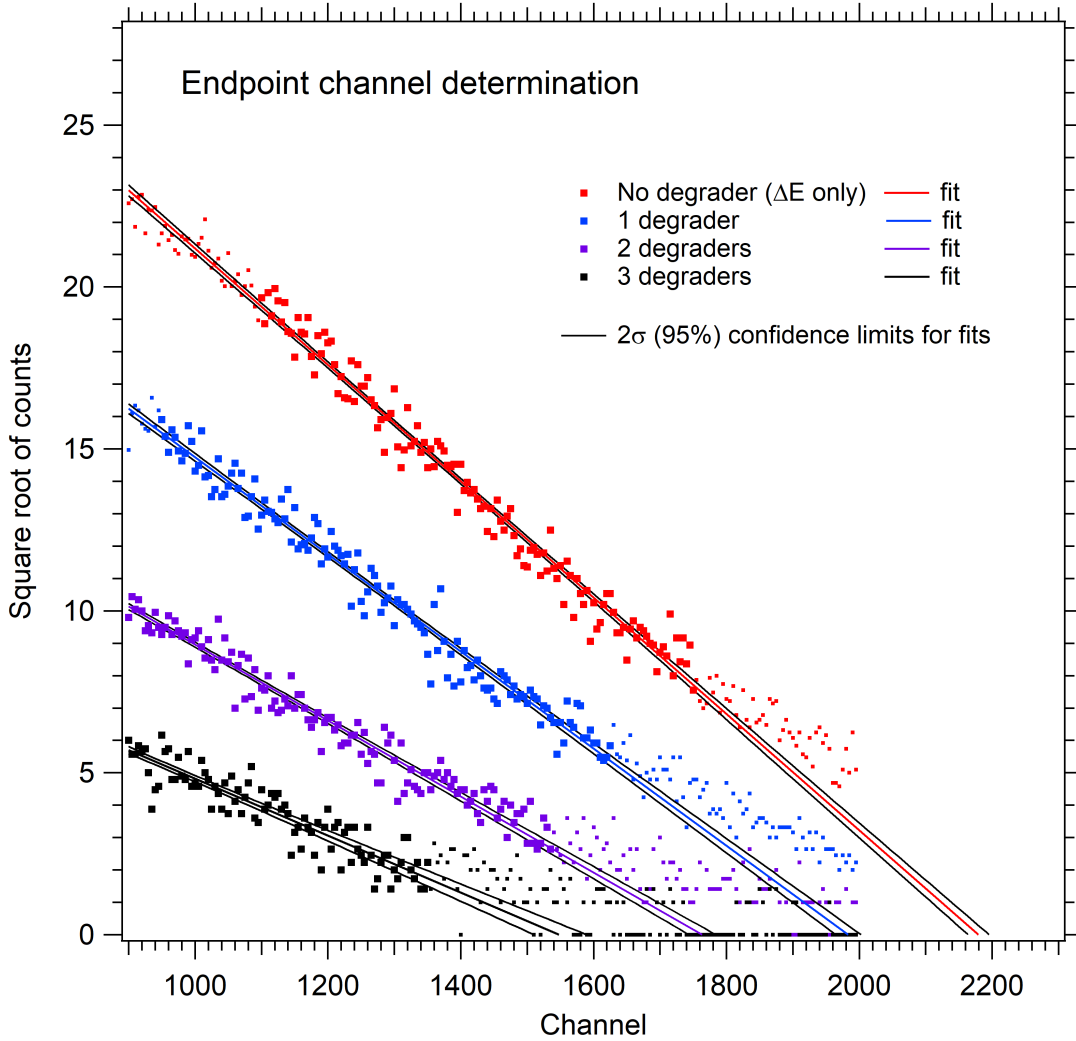


Figure 69. End point channel determination

Table 6. The both spectrum and endpoint channels of the spectra shown in figure 69 and the corresponding calculated endpoint energies. See text for calculation and endpoint channel determination details.

Number of degraders	Endpoint channel	Calculated endpoint energy (keV)
0	2180 ± 15	2050
1	1985 ± 20	1860
2	1765 ± 20	1670
3	1550 ± 40	1480

and there is always very little data close to the endpoint of the spectrum. There are techniques to determine the endpoint using the shape of spectrum, such as Fermi-Kurie plot [9] and shape fit [92] that was mentioned in the section 8.2.1.

Both these techniques utilise the shape of the beta spectrum. In principle, adding degraders changes the shape of the spectrum because the energy loss of beta electrons depends on their energy. Above 1 MeV the energy loss of electrons however depends only little on their initial energy. The shape fit technique could be otherwise applied, but there is no reference spectrum available. In the case of light collection, where only relative shape was of interest, any spectrum could have been chosen as the reference. Here, the actual end point channel of none of the spectra is known. This is why the shape stretching method runs in difficulties and can not be used.

Figure 69 shows a Fermi-Kurie plot applied on the data. The plots in the figure are not strictly Fermi-Kurie plots but square root of counts plotted against the channel number. A linear fit is then applied to the region that is estimated to be above 1 MeV, and extrapolated to zero. The uncertainty of endpoint channel is taken from the 2σ confidence of the fit. The fitting region is indicated in the figure by larger size data point symbols.

The data deviate from the fit in the high energy tail of the spectra. The data points start be above the fitted spectrum. These points are excluded from the fit because they deviate from the square root behavior. Unlike in the real Fermi-Kurie analysis, the endpoint of the analysed spectra is not because of the Q-value of the corresponding beta decay. Here the electron's energy is degraded from some higher value. There is staggering in the energy of the slowed down electrons. It is assumed that the electrons in the high energy tail of the spectrum represent those electrons whose energy has been reduced less than average. The average endpoint of the degraded electrons would be found better by extrapolating from the lower energies, where the data are more abundant and the behavior seemingly follows the square root of observed counts.

In addition, if the endpoint channel of all spectra is analysed in the same way, the possible bias is similar. At least when the data points are used to determine rather the gain (energy per channel) than the absolute energy calibration, the bias should for the most part cancel out.

Figure 70 displays the calculated endpoint energies versus endpoint channels and the linear fit through the data. According to the fit, the energy in the zero channel would be 65 ± 130 keV. Since the estimation of the energy of the endpoint of the degraded spectra is not super accurate either, this value comes satisfying close to zero and increases confidence that the way the endpoint channel has been determined

is not severely biased. The determined energy calibration with this technique is

$$E = 0.91 \times channel + 65 \text{ keV} \quad (41)$$

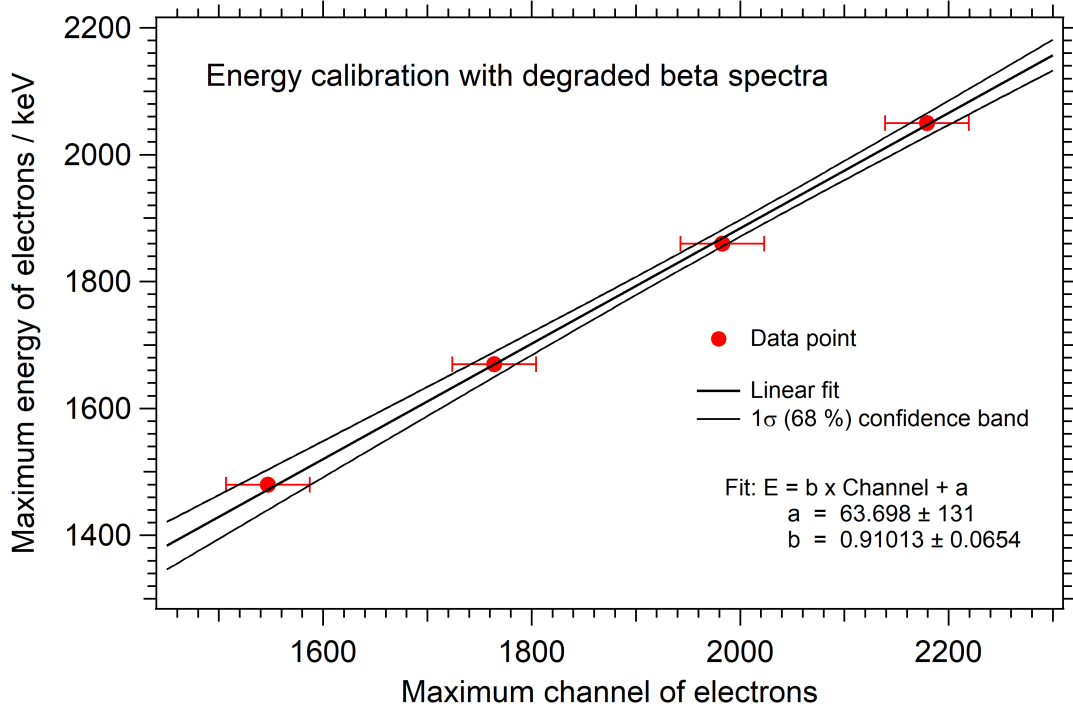


Figure 70. Energy calibration with degraded beta spectrum

Another method for energy calibration is calibration using the position of the Compton edge. The benefit of this technique is that the Compton electrons are generated inside the detector, so they do not lose their energy in any foils or other detectors. The figure 72 shows the E detector spectra of ^{137}Cs and ^{60}Co gamma ray sources. The well-known position of the ^{137}Cs Compton edge is 478 keV (see figure 71). Ideally, the edge would be sharp, but it is smeared due to limited resolution of the detector. As for ^{60}Co , it has two strong gamma rays and thus, ideally, two Compton edges. Limited detector resolution smears the edges together to one apparent Compton edges at 1041 keV [93]. The edge position was determined as shown in the figure 72. The position of the Compton edge is determined on the basis of references [94, 95] as the point where the slope of the Compton edge drops below 75 % of the top of the Compton peak, as shown in figure 72. The result is summarized in the table 7.

The energy calibration with the Compton edges is shown in figure 73. The energy

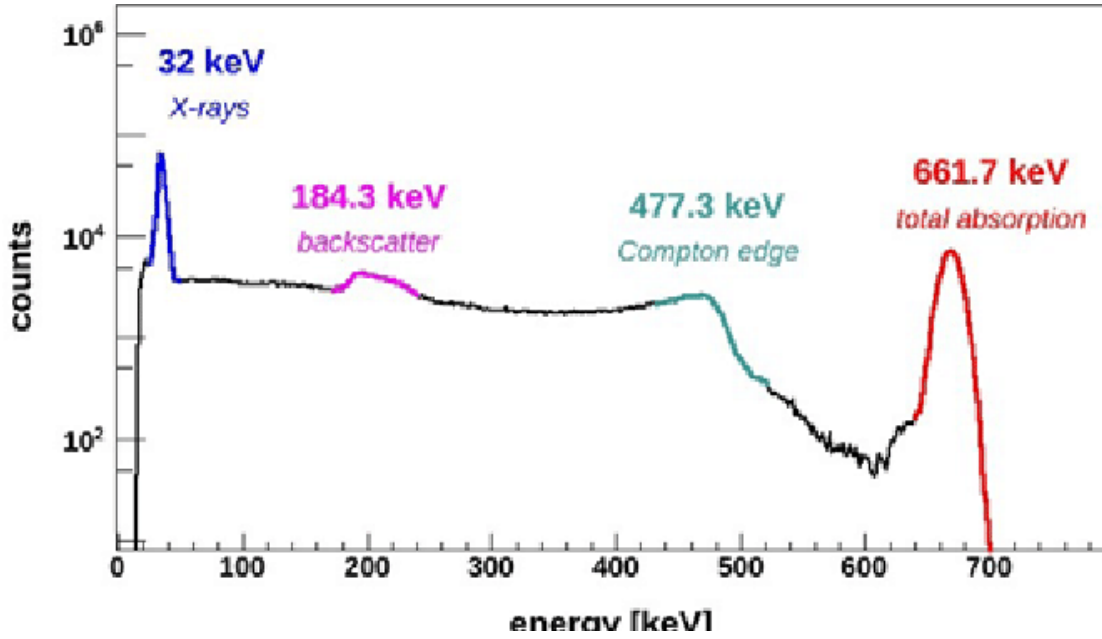


Figure 71. ^{137}Cs γ energy spectra

Table 7. The energies and positions of the Compton edges of ^{137}Cs and ^{60}Co

Nuclide	γ -ray (keV)	Compton edge (keV)	Channel
^{137}Cs	662	478	452 ± 4
^{60}Co	1173, 1332	1041	970 ± 5

calibrations of the E detector are thus

$$E = 0.91 \times \text{channel} + 65 \text{ keV} \quad (42)$$

$$E = 1.07 \times \text{channel} + 3 \text{ keV} \quad (43)$$

These two energy calibrations are sufficiently close to be combined by including all the data points in a linear fit. This is done in figure 74. The fit leaves just one data point, the one from Compton edge of ^{60}Co , off from the linear fit. The final energy calibration of the E detector becomes

$$E = 0.93 \times \text{channel} + 27 \text{ keV} \quad (44)$$

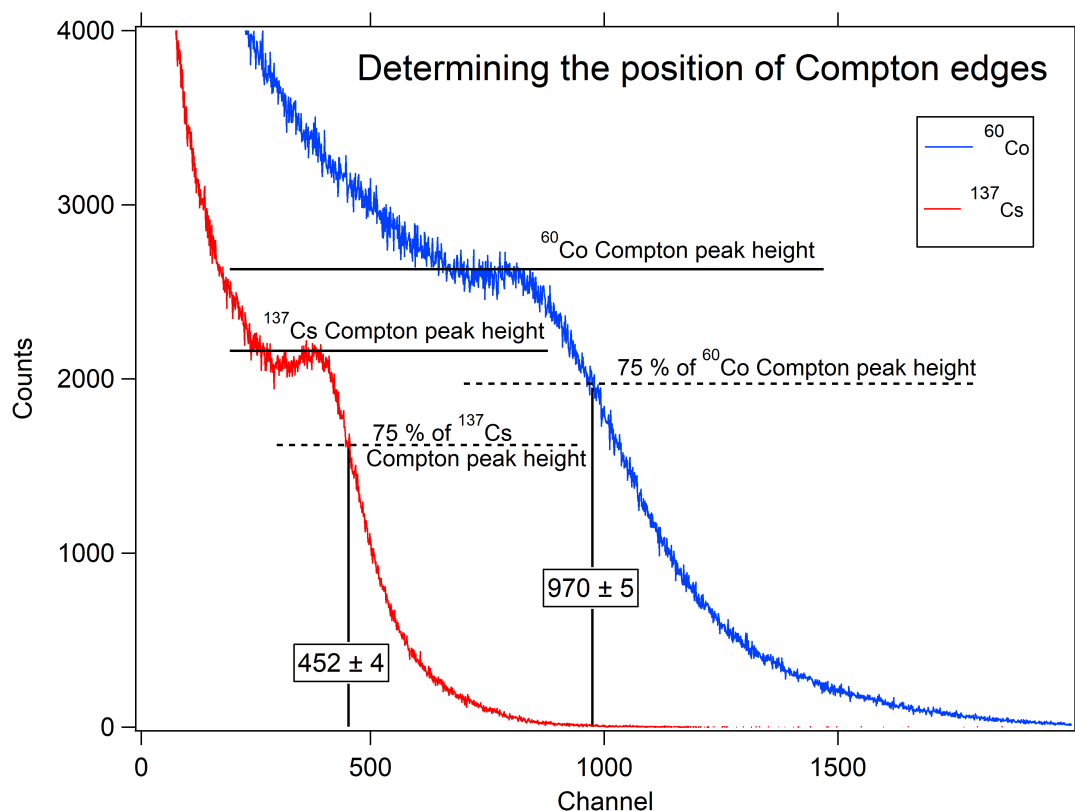


Figure 72. The position of the Compton edges is determined as the energy where the slope of the edges falls below 75 % of the level of the Compton peak. The corresponding levels and the crossing point are identified. The channel uncertainty comes mostly from the adjustment of the Compton peak height level.

8.4.2 The energy calibration of the ΔE detector

The energy calibration of the ΔE detector is based on the energy that is left in the detector by a passing electron. The electrons with more than 1 MeV leave approximately 190 keV in 1.0 mm of scintillation material. Under 600 keV the energy transfer to the detector starts rapidly increase, until electrons at 300 keV and under are entirely stopped. This low energy part of the beta spectrum produces the tail on the high energy side of the beta particle transmission peak, as well as real counts on the low energy side of the transmission peak. The peak itself is expected to locate at 190 keV for electrons that hit the detector in the right angle.

In principle the position of the transmission peak could be adjusted by allowing the collimated beta electron beam pass the detector in more oblique angle. The

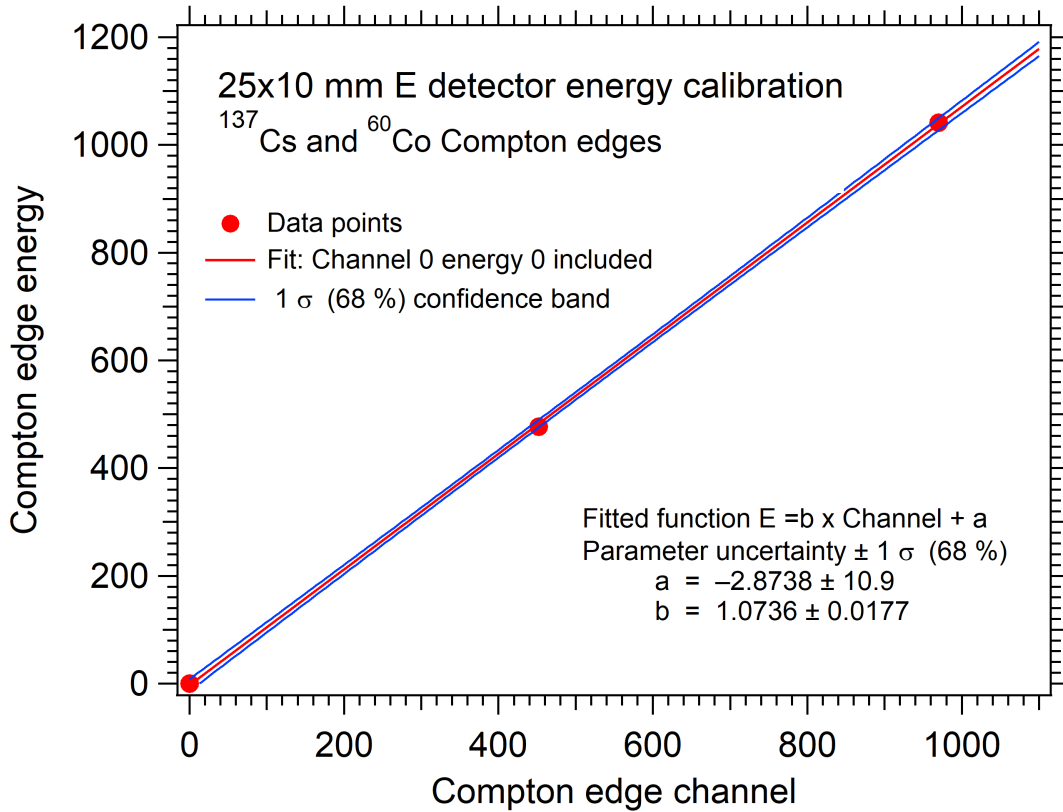


Figure 73. Energy calibration of the E detector using ⁶⁰Co and ¹³⁷Cs Compton edge positions. The origin (energy at channel 0 is zero) is included in the fit.

trajectory length L of the electron should follow

$$L = d / \cos\theta \quad (45)$$

where d is the thickness of the detector and θ is the inclination angle.

The transmission spectra of a collimated beta beam was measured at three angles, 0, 30 and 60 degrees with respect of the detector normal. The measured spectra are shown in figure 75. As explained, the transmission peak consists of a peak, and a tail on the high energy side. The position of the peak is determined as the maximum of each spectrum. The Gaussian fits shown in the figure are used as an aid to locate the maximum.

Using relation 45 it was calculated that the transmission peak would locate at 220 keV at 30 degrees and at 380 keV at 60 degrees. Assuming also that zero channel would correspond to zero keV, it was expected that the transmission peak would move to approximately 15 % higher channel at 30 degrees and 100 % higher at 60

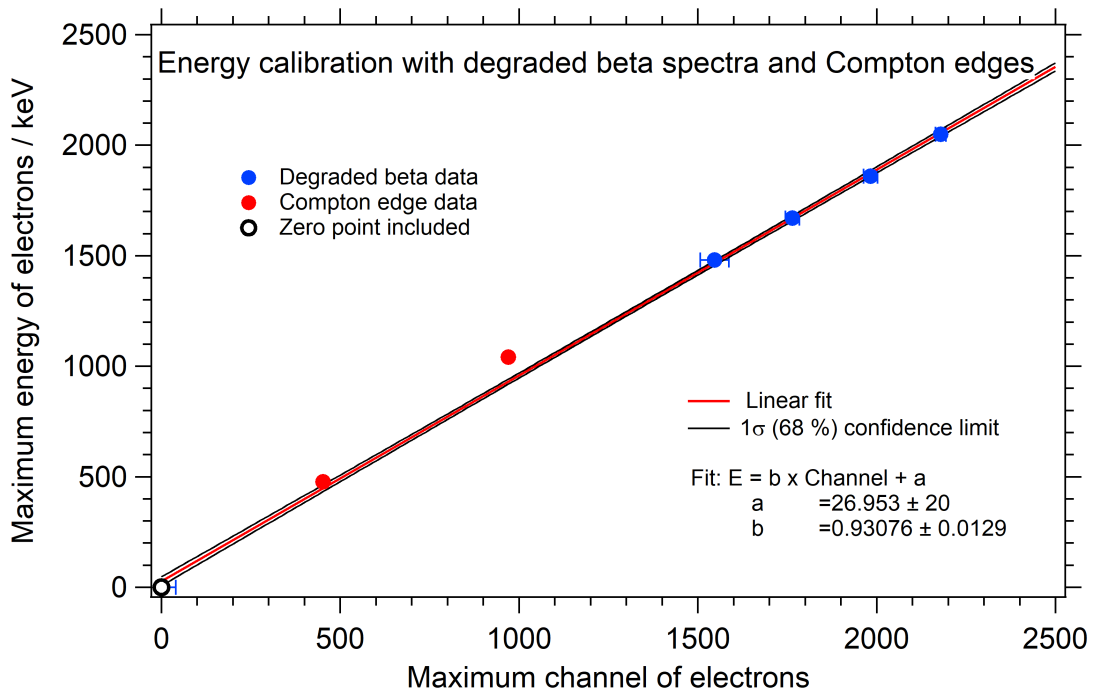


Figure 74. Energy calibration with degraded beta spectra and Compton edge

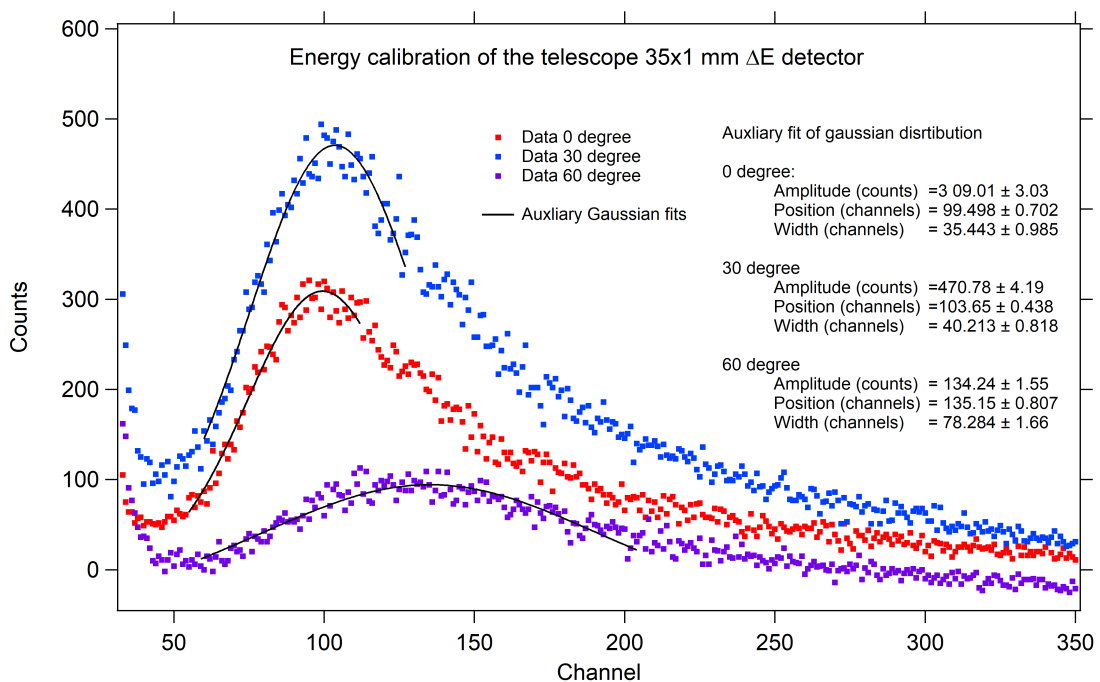


Figure 75. Fit of transmission peak positions.

degrees. The result of the analysis shown in figure 76 is not in agreement with this. Observed increase of the channel is only 4 % at 30 degree and 35 % at 60 degree.

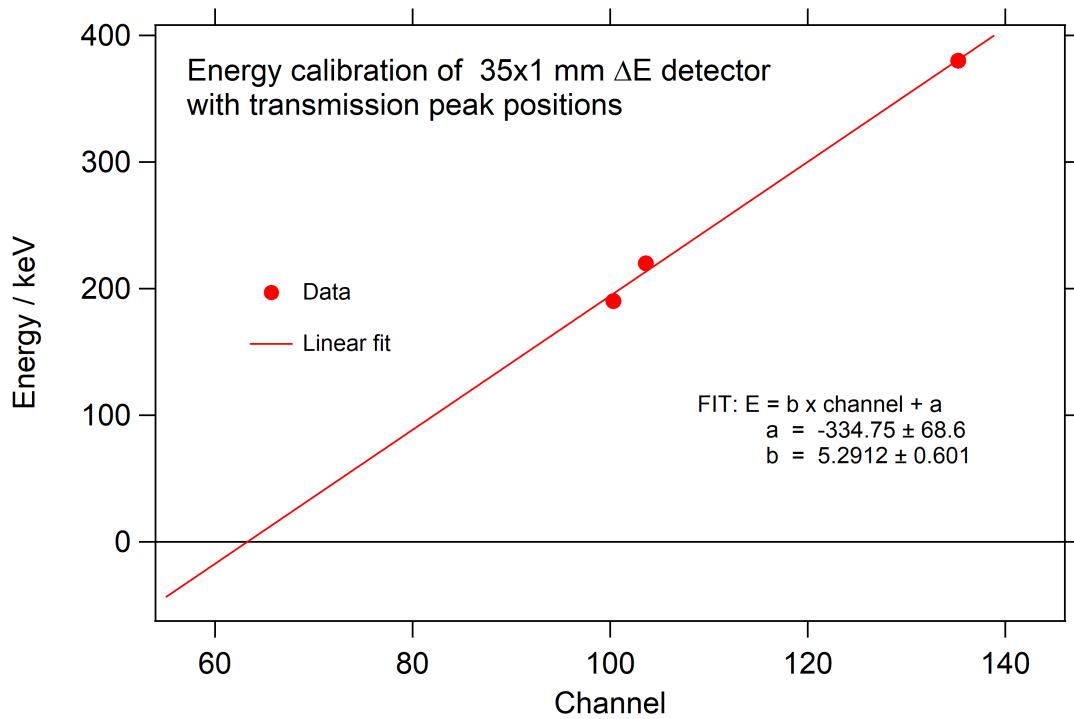


Figure 76. Energy calibration of 35×1 mm ΔE detector with transmission peak position

A linear fit to these data suggests zero energy locating at channel 60, and gain 5.3 keV/channel. This is clearly impossible, since then the tail of the transmission spectra would extend above 1.5 MeV.

It seems that assumption of approximately parallel collimated beta particle beam and straight-forward application of 45 are too simplifying. Since the calibration of the E detector strongly supported the zero energy being located close to zero channel, it is plausible this is the case for the ΔE detector as well. The energy calibration for the ΔE detector is therefore finally taken from the location of the perpendicular transmission peak. The adopted energy calibration for the ΔE becomes as

$$E = 2.0 \times \text{channel keV} \quad (46)$$

8.5 Two dimensional spectra

The data taken with the telescope detector can be visualised as a two-dimensional matrices. Such a matrix of is displayed in figure 77. On the horizontal axis is the energy of the ΔE detector and on the vertical axis the energy of the E detector. Energy calibration determined in the previous section 8.4 have been applied.

The requirement of having a coincidence condition between the detectors has first of all totally removed the ΔE detector noise from the spectrum (see for example figure 64). The projection of the ΔE - E matrix in figure 77 on the ΔE direction is shown in figure 78. The remnant of the strong noise peak is shown by an arrow. Note the logarithmic scale.

In the E spectrum the noise does not disappear. The red area in the matrix, the highest counts, represent a decent ΔE spectrum that is somehow in coincidence with E detector noise. It is not clear whether it is a weak signal really in coincidence, or a noise that is in random coincidence with the ΔE detector.

Since the ΔE detector clearly measures a large fraction of the electron energy, for the final analysis the ΔE and E detector signals need to be added up on event basis. The small E signals can however be excluded from this calculation without any effect on the high energy (more than 700 keV) end of the total beta energy spectrum. This is shown in figure 79. The energy of ΔE detector signals is not high enough to contribute to the total energy intensity above 500 keV.

8.5.1 Telescope efficiency

The telescope efficiency was determined from the total energy spectrum produced from the two-dimensional matrix. The total beta energy spectra of a $^{90}\text{Sr}/^{90}\text{Y}$ source was recorded at two distances, at 5 mm and and at 16 mm from the telescope. The generated total energy spectra are shown in figure 81. The accepted in the shaded area ($E_{tot} > 700$ keV). The low energy beta events are not of interest, thus the E energy threshold is set well above the noise (see figure 79).

The beta radiation exposure last 30 minutes or 1800 s for both spectra. From the known beta source activity 16.9 kBq (table 5, calibrated activity projected to August 2021) it can be calculated that the source emitted $N = 1800 \text{ s} \times 16900 \text{ 1/s} = 30420000$ ^{90}Y beta electrons during the measurement. 60 % of those, 18252000, has energy larger than 700 keV. The total efficiencies ϵ_{tot} for ^{90}Y detection becomes then

R396.dat Distance = 5mm, Time = 30 minutes Not collimated ^{90}Sr source

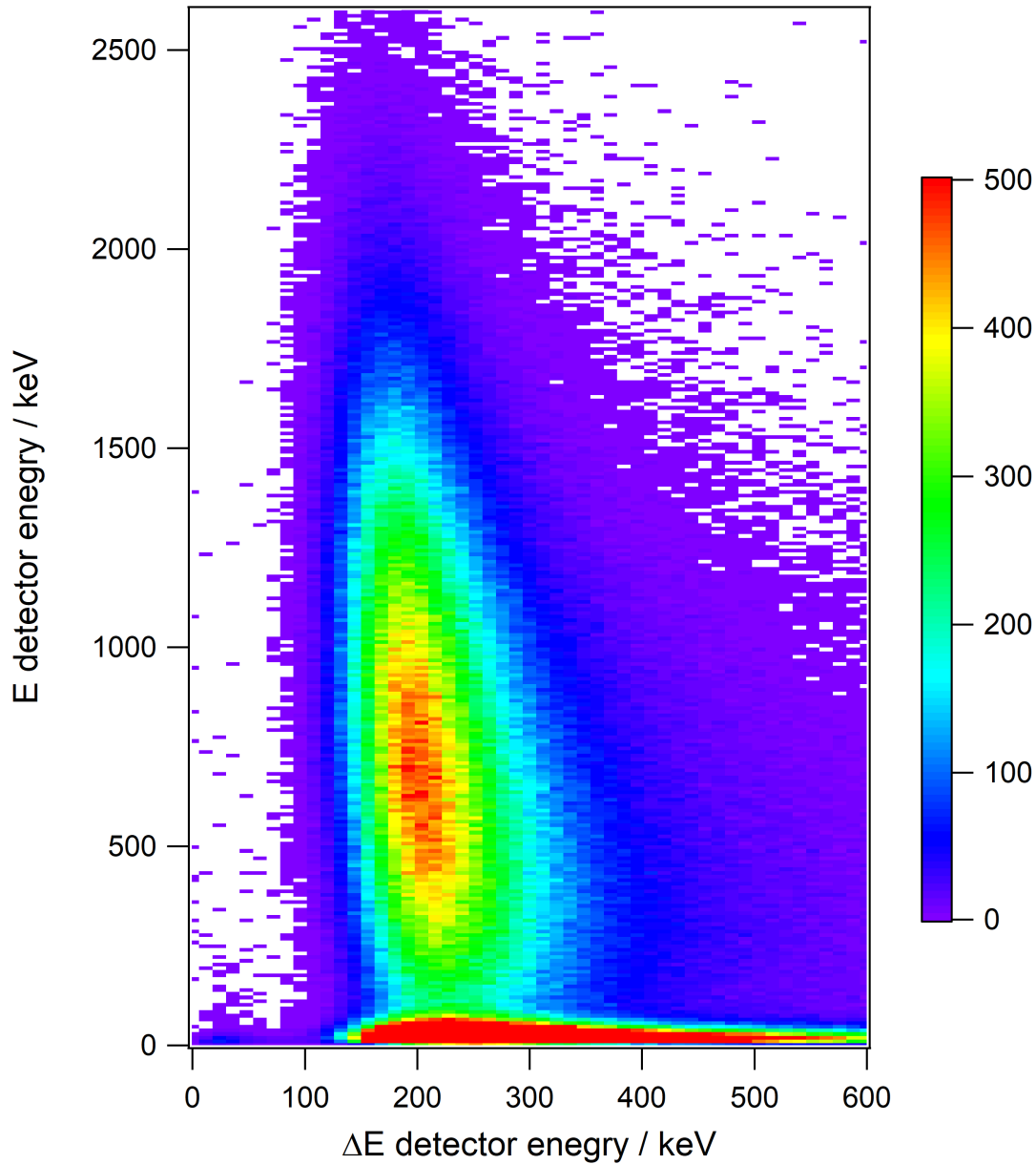


Figure 77. Two-dimensional matrix of the beta telescope prototype. The source is $^{90}\text{Sr}/^{90}\text{Y}$ without any collimation and located at 5 mm from the detector.

$\epsilon_{tot} = 2.33\%$ at 5 mm and 1.14% at 16 mm.

The measurements were made at 5 mm and 16 mm from the end of the source stick. The source itself is however about 3 mm deeper in a small well in the tip of the stick. For calculations of the geometrical efficiencies distances of 8 mm and

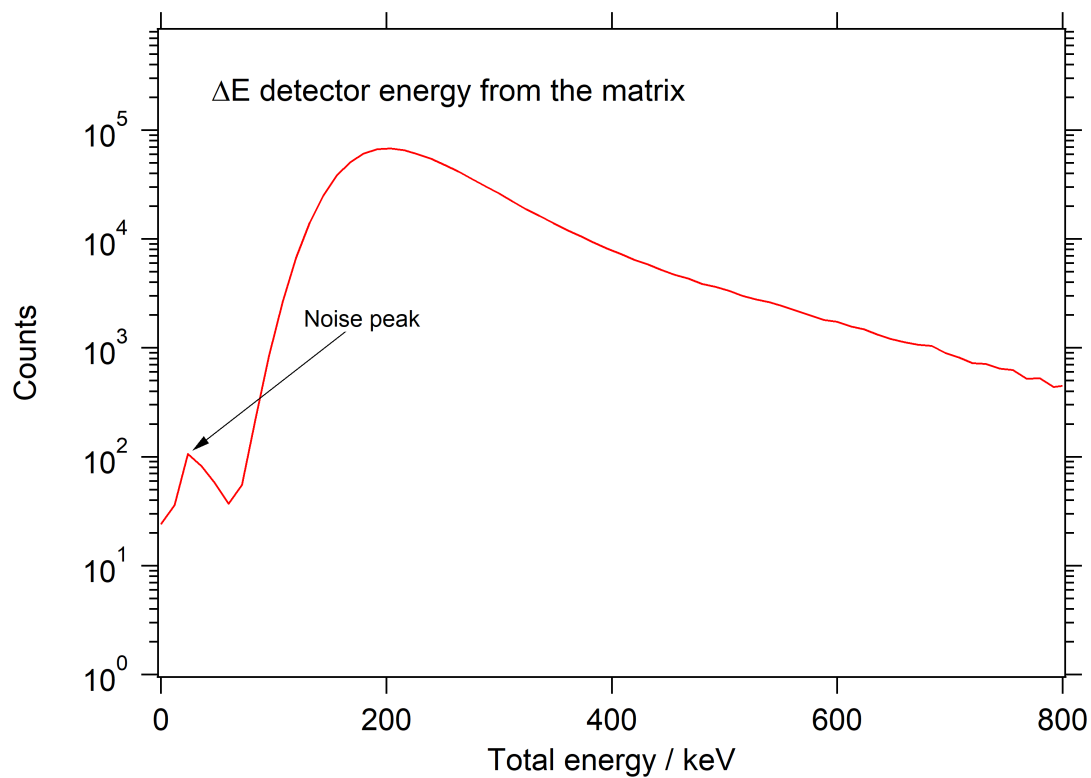


Figure 78. ΔE energy from the matrix

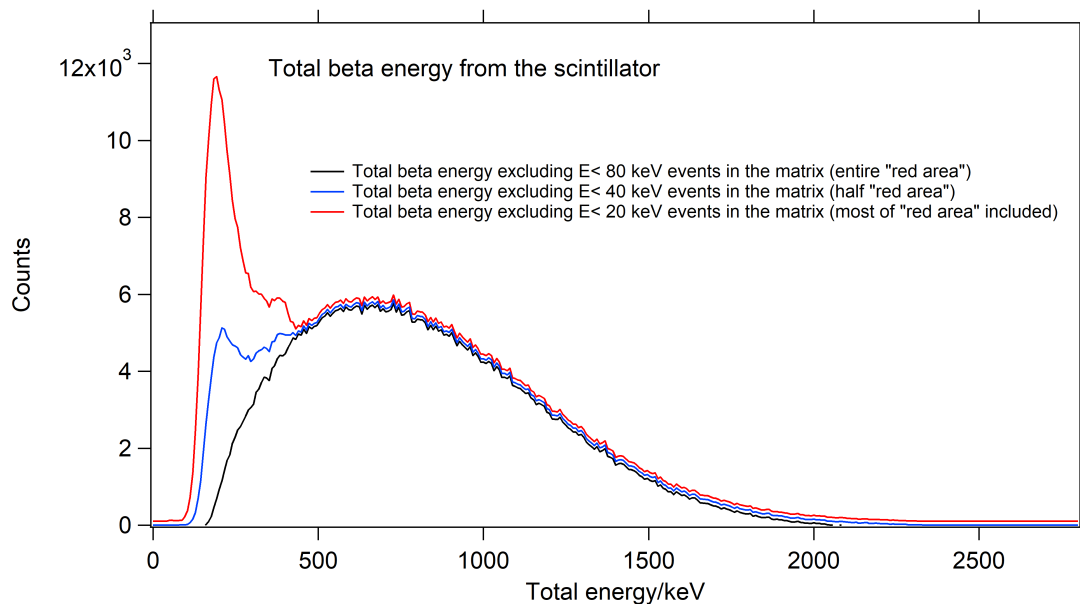


Figure 79. Summed up energy of E and ΔE detectors with different thresholds set in the E detector. The graphs are in reality on top of each other in region above 500 keV. They have been slightly offset for clarity.

R397.dat Distance = 16mm, Time = 30 minutes Not collimated ^{90}Sr source

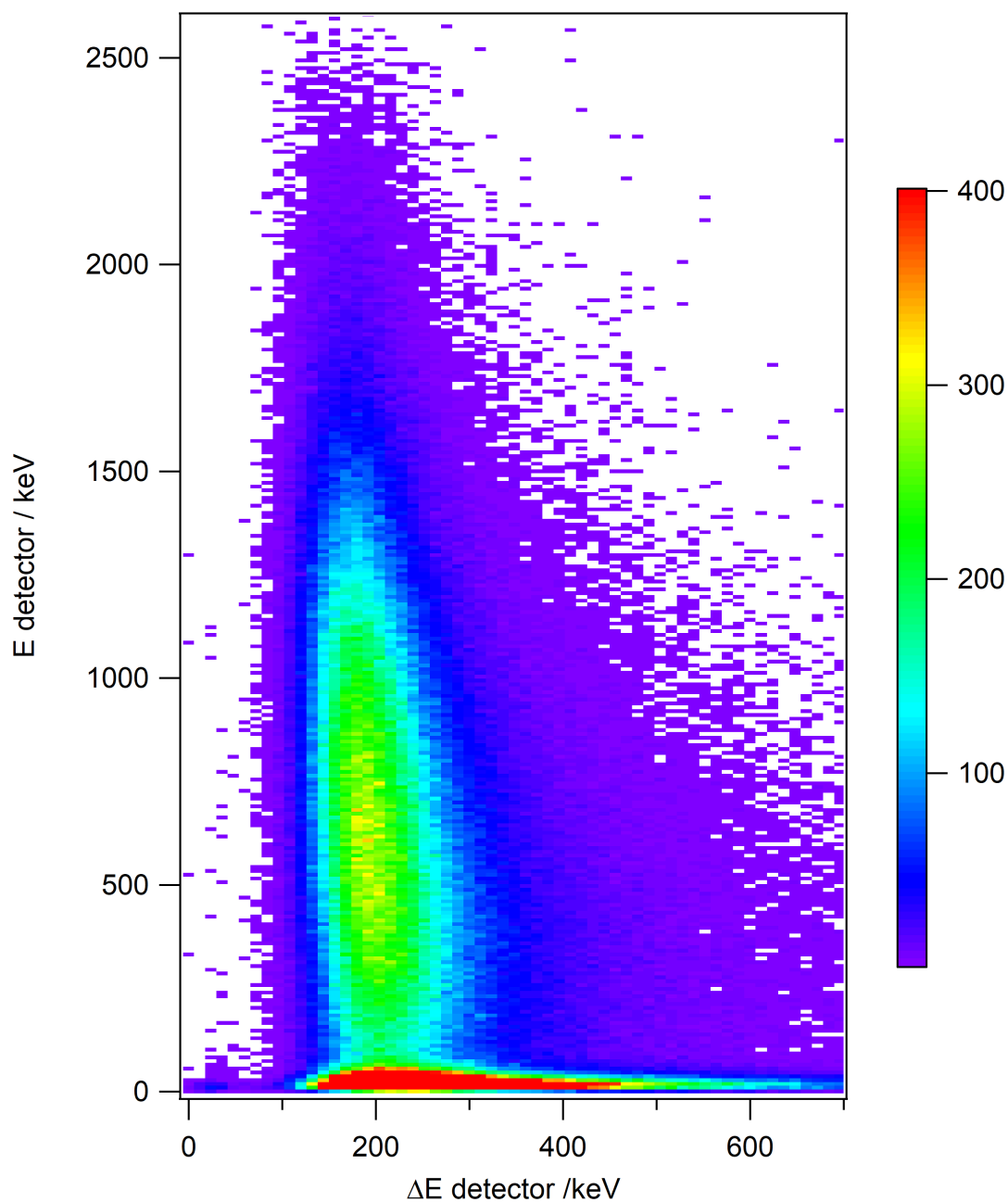


Figure 80. Two dimensional matrix of non-collimated ^{90}Sr source at 16 mm distance for 30 minutes irradiation.

19 mm were used. The geometrical efficiency for a point source at these distances from a 25 mm diameter detector are 23 % and 8.2 %, respectively. The detector intrinsic efficiency ϵ_{int} is

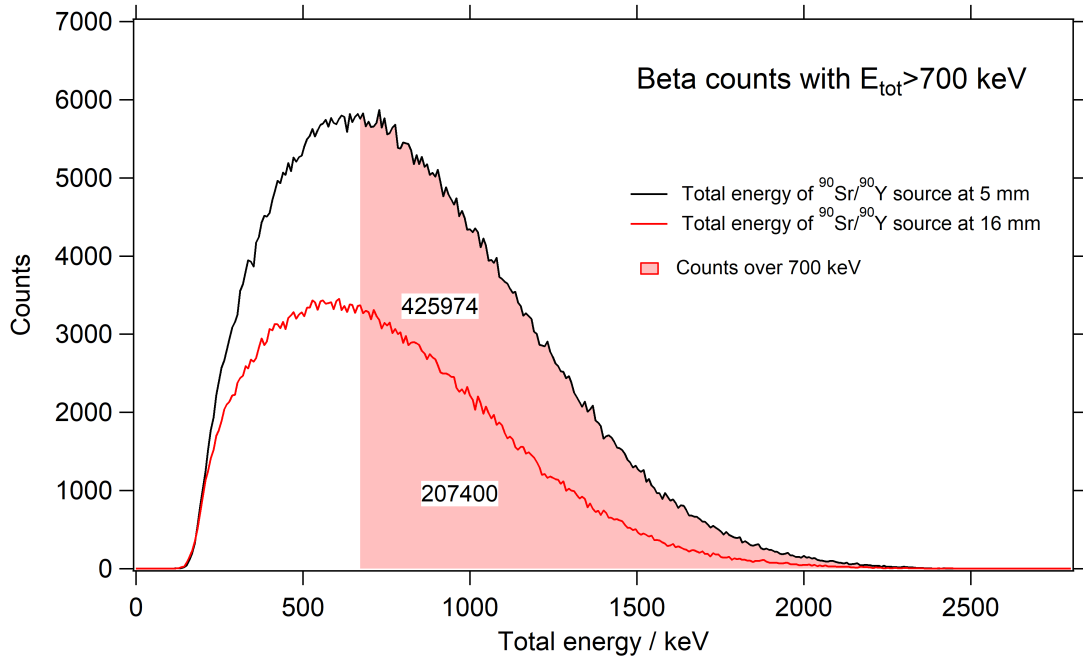


Figure 81. Total beta energy spectra extracted from ΔE - E matrices in figure 77 and 80. The number of beta events with $E_{tot} > 700$ keV is shown.

$$\epsilon_{int} = 2.33 \% / 0.23 = 10.1 \%$$

$$\epsilon_{int} = 1.14 \% / 0.082 = 13.9 \%$$

from the 5 mm and for the 16 mm measurements. The average value for the intrinsic efficiency is thus about 12 %.

8.5.2 Gamma ray discrimination

In figure 80 is shown the two-dimensional matrix of a measurement of ^{137}Cs source at 4 mm distance from the telescope. The gamma ray should not produce a signal in both detector simultaneously except in some special situations. In the ΔE - E matrix, there is however a structure that looks like a ^{137}Cs Compton continuum in coincidence with a ΔE detector signal. A closer look shows however that the ΔE detector signal can not come from an electron since its energy is clearly smaller than that of beta electron transmission peak. The projection of the matrix in figure 80 on the ΔE axis is shown in figure 83 with the projection of the matrix in figure 77 having a clear transmission peak.

It can be calculated that the used 175 kBq ^{137}Cs source emitted 89 million 662 keV gamma rays in 10 minutes. They have 26 % geometrical efficiency to hit the telescope

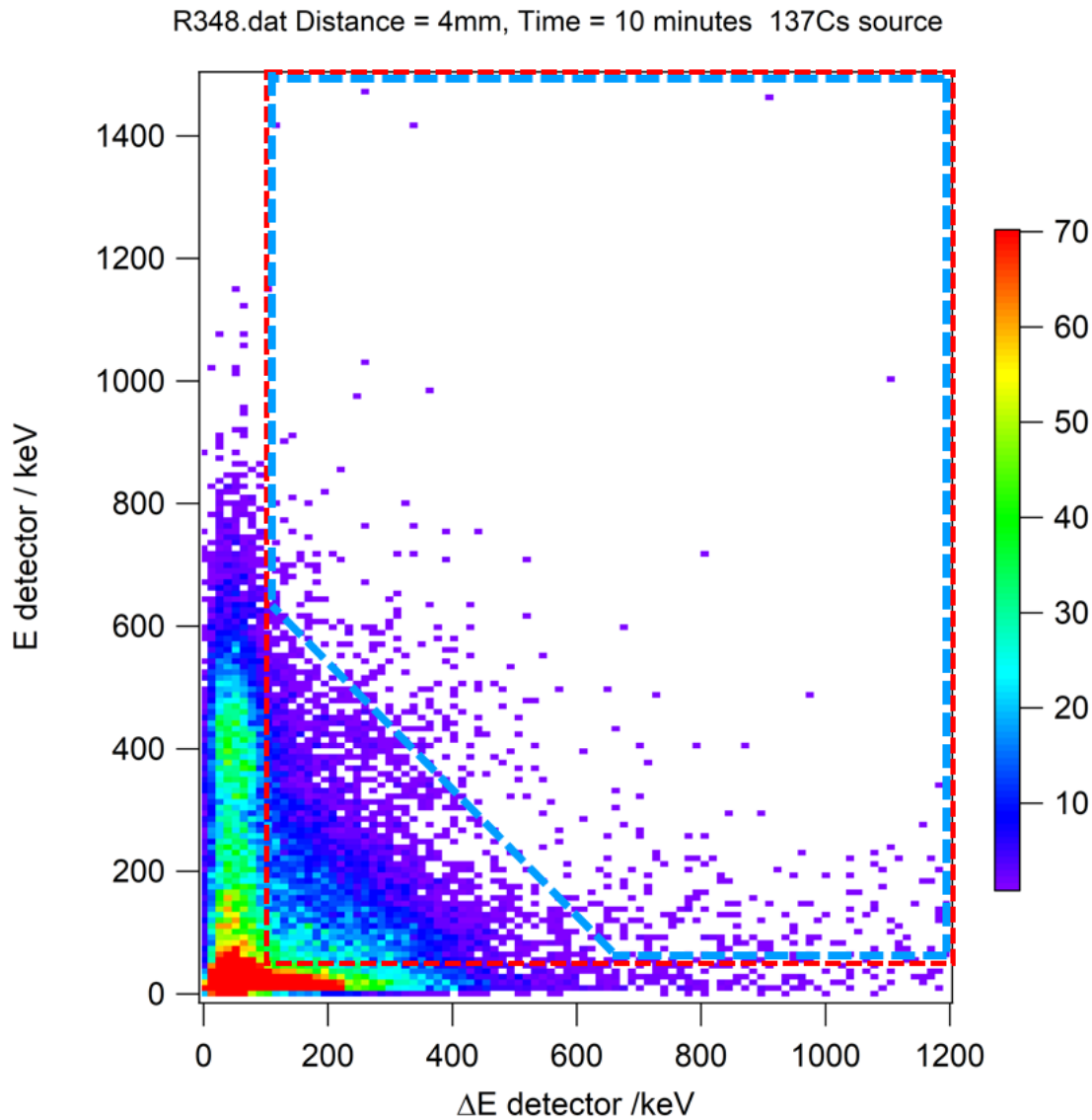


Figure 82. Two dimensional matrix of ^{137}Cs source at 4 mm distance for 10 minutes. The red rectangular indicates the area of proper beta particle events. The blue line surrounds the area of events with $E_{tot} > 700$ keV.

detector. When the ΔE and E thresholds were applied, of these 23 million gamma rays only 9000 produced a signal that could have been interpreted as a beta event. The region of proper beta events is indicated by the red rectangle in figure 80. The reduction factor was thus such that from the gamma rays hitting the detector one of 2500 gives a coincident signal. The amount of misleading signals is reduced even more, when the total energy threshold of 700 keV is set. The area surrounded by the

blue line in figure 80 show shows the area of acceptable events such as are counted in the figure 81. The amount of false events is reduced to ~ 200 out of 23 million. It is also worth of noticing that the gamma count rate was ~ 38 kHz; most of those ~ 200 false events must be random coincidences between pile-up events. These will not appear in low-level measurements. The combination of $\Delta E - E$ coincidence and total beta energy gating seems to very efficiently reject the gamma radiations.

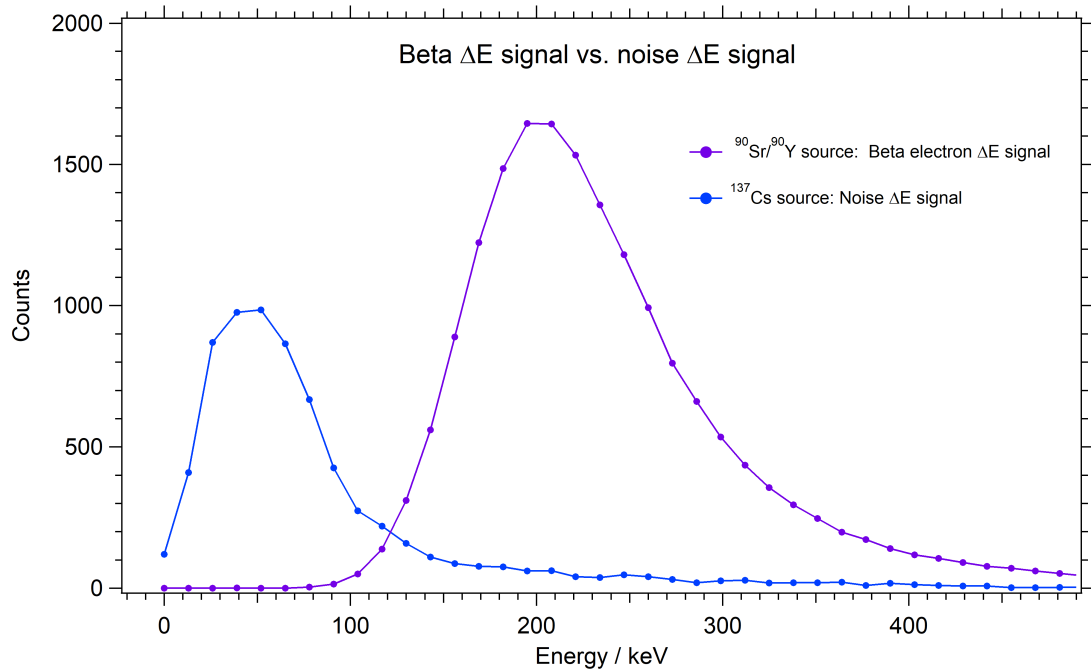


Figure 83. Beta ΔE signal projected from $\Delta E - E$ matrix shown in figure 77 versus noise ΔE signal projected respectively from figure 82

9 Conclusions and Discussion

A ΔE - E telescope detector was build and tested. It was found capable of discriminating gamma radiations from ^{90}Y . The discrimination against gamma rays was better than a factor of 1,000. Combined with total beta energy gating the gamma event rejection was found to be at the order of a factor of 10^5 .

The intrinsic efficiency of detector was about 12 %, which is a ratio between detected and incident radiation events. In the intrinsic efficiency calculation the shielding of the ΔE SiPM was not taken into account. SiPM was attached on the front face of the telescope in this first prototype.

The intrinsic efficiency was found to be smaller in the closer geometry. A physical explanation to this could be backscattering of electrons from the surface of the detector. Backscattering is more probable for oblique angles. This effect could be studied in more detail in the future.

The total efficiency depends on the geometry and geometrical efficiency. For ^{90}Y detection it was about 2.33 % at 5 mm and 1.14 % at 16 mm respectively. The detection limit with low intensity sources was not tested.

The main problem during the work was low energy noise that was only partly removed by the coincidence between the detectors. The reason might be that the light shielded box was not good enough or the dark count rate of SiPM was high.

The light collection efficiency was quite uneven in both detectors. A solution to this could be improving the light collection with light guides instead of attaching the SiPM directly on the detectors. In particular this could improve the light collection efficiency from the ΔE detector and possibly allow using larger area scintillators. It could however also make the light collection more even from different parts of the scintillator as well. With SiPM attached directly on scintillators, the signals from the immediate vicinity of the SiPM are too pronounced.

References

- [1] Y. Onda et al. “Radionuclides from the Fukushima Daiichi nuclear power plant in terrestrial systems”. In: *Nature Reviews Earth & Environment* 1.12 (2020), pp. 644–660. DOI: 10.1038/s43017-020-0099-x.
- [2] G. Steinhauser, A. Brandl, and T. E. Johnson. “Comparison of the Chernobyl and Fukushima nuclear accidents: a review of the environmental impacts”. In: *Science of the total environment* 470 (2014), pp. 800–817. DOI: <https://doi.org/10.1016/j.scitotenv.2013.10.029>.
- [3] A. V. Yablokov, V. B. Nesterenko, and A. V. Nesterenko. “Chapter III. Consequences of the Chernobyl catastrophe for the environment”. In: *Annals of the New York Academy of Sciences* 1181.1 (2009), pp. 221–286. DOI: 10.1111/j.1749-6632.2009.04830.x.
- [4] G. I. Dovbeshko et al. “FTIR spectroscopy studies of nucleic acid damage”. In: *Talanta* 53.1 (2000), pp. 233–246. DOI: 10.1016/S0039-9140(00)00462-8.
- [5] A. Erikson et al. “Preparation of animal tissue samples for the determination of ^{90}Sr and actinides”. In: *Journal of radioanalytical and nuclear chemistry* 131.1 (1989), pp. 89–94. DOI: 10.1007/BF02046612.
- [6] K. Sasa et al. “A sensitive method for Sr-90 analysis by accelerator mass spectrometry”. In: *Journal of Nuclear Science and Technology* 58.1 (2021), pp. 72–79. DOI: 10.1080/00223131.2020.1801530.
- [7] Y. Kameo et al. “Rapid determination of ^{89}Sr and ^{90}Sr in radioactive waste using Sr extraction disk and beta-ray spectrometer”. In: *Journal of radioanalytical and nuclear chemistry* 274.1 (2007), pp. 71–78. DOI: 10.1007/s10967-006-6905-1.
- [8] B. M. Coursey et al. “Liquid-scintillation counting techniques for the standardization of radionuclides used in therapy”. In: *Nuclear Instruments and Methods in Physics Research Section A: Accelerators, Spectrometers, De-*

- tectors and Associated Equipment* 339.1-2 (1994), pp. 26–30. DOI: [https://doi.org/10.1016/0168-9002\(94\)91773-6](https://doi.org/10.1016/0168-9002(94)91773-6).
- [9] G. F. Knoll. *Radiation detection and measurement*. John Wiley & Sons, 2010.
- [10] W. Crookes. “Certain properties of the emanations of radium”. In: *Chem. News* 87.2269 (1903), p. 241. URL: <https://www.bibsonomy.org/bibtex/2ac3785a8b15c5acbf6e51416a629c139/rwst>.
- [11] H. Gegier and E. Marsden. “On a diffuse reflection of the α -particles”. In: *Proceedings of the Royal Society of London. Series A, Containing Papers of a Mathematical and Physical Character* 82.557 (1909), pp. 495–500. URL: <https://doi.org/10.1098/rspa.1909.0054>.
- [12] E. Rutherford. “LXXIX. The scattering of α and β particles by matter and the structure of the atom”. In: *The London, Edinburgh, and Dublin Philosophical Magazine and Journal of Science* 21.125 (1911), pp. 669–688. DOI: 10.1080/14786440508637080.
- [13] A. Mapelli. “Scintillation Particle Detectors Based on Plastic Optical Fibres and Microfluidics”. PhD thesis. Ecole Polytechnique, Lausanne, 2011. URL: <https://infoscience.epfl.ch/record/164027?ln=en>.
- [14] S. Min et al. “Integrated and portable probe based on Functional plastic scintillator for detection of radioactive cesium”. In: *Applied Sciences* 11.11 (2021), p. 5210. DOI: 10.3390/app11115210.
- [15] *EPA Facts about Strontium-90*. URL: <https://semspub.epa.gov/work/HQ/175430.pdf>. (visited on 31/05/2022).
- [16] D. Malain and P. Kanchana. “Evaluation of radiation safety for ionization chamber smoke detectors containing Am-241”. In: *Journal of Physics: Conference Series*. Vol. 1285. 1. IOP Publishing, 2019, p. 012047. DOI: 10.1088/1742-6596/1285/1/012047.
- [17] *Attenuation length*. URL: https://en.wikipedia.org/wiki/Attenuation_length. (visited on 13/05/2022).
- [18] A. Wiczorek. “Development of novel plastic scintillators based on polyvinyl-toluene for the hybrid J-PET/MR tomograph”. In: *arXiv preprint arXiv:1710.08136* (2017). DOI: <https://doi.org/10.48550/arXiv.1710.08136>.

- [19] S. Tavernier. *Experimental techniques in nuclear and particle physics*. Springer Science & Business Media, 2010. DOI: 10.1007/978-3-642-00829-0.
- [20] C. Melcher. “Perspectives on the future development of new scintillators”. In: *Nuclear Instruments and Methods in Physics Research Section A: Accelerators, Spectrometers, Detectors and Associated Equipment* 537.1-2 (2005), pp. 6–14. DOI: <https://doi.org/10.1016/j.nima.2004.07.222>.
- [21] N. Tsoulfanidis and S. Landsberger. *Measurement & detection of radiation*. CRC press, 2021. ISBN: 9780429193880.
- [22] W. R. Leo. *Techniques for nuclear and particle physics experiments: a how-to approach*. Springer Science & Business Media, 2012. ISBN: 978-3-642-57920-2.
- [23] *ENERGY BANDS- Semiconductor Physics*. URL: <https://www.eeupdate.com/2018/10/energy-bands-semiconductor-physics.html>. (visited on 03/05/2022).
- [24] S. N. Ahmed. *Physics and engineering of radiation detection*. Academic Press, 2007. ISBN: 9780080569642.
- [25] *Benzene*. URL: <https://en.wikipedia.org/wiki/Benzene>. (visited on 03/05/2022).
- [26] J. B. Birks. *The theory and practice of scintillation counting: International series of monographs in electronics and instrumentation*. Vol. 27. Elsevier, 2013. ISBN: 9781483156064.
- [27] C. H. Lee et al. “Characteristics of plastic scintillators fabricated by a polymerization reaction”. In: *Nuclear Engineering and Technology* 49.3 (2017), pp. 592–597. DOI: <https://doi.org/10.1016/j.net.2016.10.001>.
- [28] S. Min et al. “A Review of Nanomaterial Based Scintillators”. In: *Energies* 14.22 (2021), p. 7701. DOI: 10.3390/en14227701.
- [29] J. R. Lakowicz. *Principles of fluorescence spectroscopy*. Springer, 2006. ISBN: 978-0-387-46312-4.
- [30] H. Bethe. “Bremsformel für elektronen relativistischer geschwindigkeit”. In: *Zeitschrift für Physik* 76.5 (1932), pp. 293–299. DOI: 10.1007/BF01342532.

- [31] S. M. Seltzer and M. J. Berger. “Bremsstrahlung spectra from electron interactions with screened atomic nuclei and orbital electrons”. In: *Nuclear Instruments and Methods in Physics Research Section B: Beam Interactions with Materials and Atoms* 12.1 (1985), pp. 95–134. DOI: [https://doi.org/10.1016/0168-583X\(85\)90707-4](https://doi.org/10.1016/0168-583X(85)90707-4).
- [32] *CHARGED PARTICLE IONIZATION AND RANGE*. URL: http://atlas.physics.arizona.edu/~shupe/Physics_Courses/Phys_586_S2015_S2016_S2017/Laboratories/lab6-IonizationRange.pdf. (visited on 31/05/2022).
- [33] *RANGE OF ATOMIC PARTICLES IN PLASTIC SCINTILLATOR*. URL: https://eljentechnology.com/images/technical_library/Response_Curves.pdf. (visited on 31/05/2022).
- [34] *GENERAL PURPOSE EJ-200, EJ-204, EJ-208, EJ-212*. URL: <https://eljentechnology.com/products/plastic-scintillators/ej-200-ej-204-ej-208-ej-212>. (visited on 18/05/2022).
- [35] *Compton scattering equation*. URL: <http://hyperphysics.phy-astr.gsu.edu/hbase/quantum/compeq.html>. (visited on 15/04/2022).
- [36] *Pair Production and Annihilation*. URL: <http://electrons.wikidot.com/pair-production-and-annihilation>. (visited on 31/05/2022).
- [37] R. Foord et al. “The use of photomultiplier tubes for photon counting”. In: *Applied optics* 8.10 (1969), pp. 1975–1989. DOI: <https://doi.org/10.1364/AO.8.001975>.
- [38] P. Tubes. “Principles and applications”. In: *Philips Photonics, Philips France* (1994).
- [39] M. Grodzicka-Kobylka, M. Moszyński, and T. Szcześniak. “Silicon photomultipliers in gamma spectroscopy with scintillators”. In: *Nuclear Instruments and Methods in Physics Research Section A: Accelerators, Spectrometers, Detectors and Associated Equipment* 926 (2019), pp. 129–147. DOI: <https://doi.org/10.1016/j.nima.2018.10.065>.
- [40] S. Gundacker and A. Heering. “The silicon photomultiplier: fundamentals and applications of a modern solid-state photon detector”. In: *Physics in Medicine & Biology* 65.17 (2020), 17TR01. DOI: [10.1088/1361-6560/ab7b2d](https://doi.org/10.1088/1361-6560/ab7b2d).

- [41] M. S. Nitschke. “Characterization of Silicon Photomultipliers Before and After Neutron Irradiation”. In: (1989). URL: https://www.physik.uni-hamburg.de/en/iexp/gruppe-garutti/publikationen/bachelor-master-theses/_files/2016-master-nitschke-michael.pdf.
- [42] W. Maes, K. De Meyer, and R. Van Overstraeten. “Impact ionization in silicon: A review and update”. In: *Solid-State Electronics* 33.6 (1990), pp. 705–718. DOI: 10.1016/0038-1101(90)90183-F.
- [43] C. Piemonte and A. Gola. “Overview on the main parameters and technology of modern Silicon Photomultipliers”. In: *Nuclear Instruments and Methods in Physics Research Section A: Accelerators, Spectrometers, Detectors and Associated Equipment* 926 (2019), pp. 2–15. DOI: <https://doi.org/10.1016/j.nima.2018.11.119>.
- [44] B. F. Aull et al. “Geiger-mode avalanche photodiodes for three-dimensional imaging”. In: *Lincoln laboratory journal* 13.2 (2002), pp. 335–349. URL: <http://citeseerx.ist.psu.edu/viewdoc/summary?doi=10.1.1.155.2750>.
- [45] S. Cova et al. “Avalanche photodiodes and quenching circuits for single-photon detection”. In: *Applied optics* 35.12 (1996), pp. 1956–1976. DOI: <https://doi.org/10.1364/AO.35.001956>.
- [46] *Silicon photomultipliers - Operation, performance and possible applications*. URL: https://www.hamamatsu.com/content/dam/hamamatsu-photonics/sites/static/hc/resources/W0003/sipm_webinar_1.10.pdf. (visited on 29/04/2022).
- [47] *MICROC-SERIES - Silicon Photomultipliers (SiPM), Low-Noise, Blue-Sensitive*. URL: <https://www.onsemi.com/pdf/datasheet/microc-series-d.pdf>. (visited on 29/04/2022).
- [48] *Introduction to the Silicon Photomultiplier (SiPM) - AND9770/D*. URL: <https://www.onsemi.com/pub/Collateral/AND9770-D.PDF>. (visited on 13/04/2022).
- [49] SensL. *An Introduction to the Silicon Photomultiplier*. 2011.

- [50] A. A. Wagadarikar et al. “Performance of low afterpulsing probability multipixel photon counters for time-of-flight positron emission tomography”. In: *2013 IEEE Nuclear Science Symposium and Medical Imaging Conference (2013 NSS/MIC)*. IEEE. 2013, pp. 1–5. DOI: 10.1109/NSSMIC.2013.6829595.
- [51] *MICROFC-60035-SMT-TR*. URL: <https://www.mouser.fi/ProductDetail/onsemi/MICROFC-60035-SMT-TR?qs=byeeYqUIhONL1tLUEc9yUw%3D%3D>. (visited on 29/04/2022).
- [52] *Silicon Photomultipliers (SiPM), Low-Noise, Blue-Sensitive C-Series SiPM Sensors*. URL: <https://www.onsemi.com/pdf/datasheet/microc-series-d.pdf>. (visited on 29/04/2022).
- [53] *An Introduction to the Silicon Photomultiplier - SETI Net*. URL: https://www.seti.net/cosmic-rays/SETIPixel/CosmicWatch-Desktop-Muon-Detector-v2-master/Datasheets/Intro_to_SiPMs.pdf. (visited on 13/04/2022).
- [54] S. D’Amato et al. “Characterization of silicon photomultiplier arrays in liquid xenon and development of dedicated read-out electronics”. PhD thesis. Universität Zürich, 2016.
- [55] *Physics and operation of the MPPC silicon photomultiplier*. URL: <https://hub.hamamatsu.com/us/en/technical-notes/mppc-sipms/physics-and-operation-of-the-MPPC-silicon-photomultiplier.html>. (visited on 29/04/2022).
- [56] C. Marentini. “Characterization of Novel VUV-silicon Photomultipliers and Their Application in Xenon-based Dual-phase TPCs”. PhD thesis. Universität Zürich, 2018. URL: https://www.physik.uzh.ch/dam/jcr:28bfab9b-88be-4b57-8ff4-4af0016168bc/master_marentini.pdf.
- [57] F. Liu et al. “Characterization of a Mass-Produced SiPM at Liquid Nitrogen Temperature for CsI Neutrino Coherent Detectors”. In: *Sensors* 22.3 (2022), p. 1099. DOI: 10.3390/s22031099.
- [58] C. Xu. *Study of the silicon photomultipliers and their applications in Positron Emission Tomography*. Tech. rep. Deutsches Elektronen-Synchrotron (DESY), 2014.

- [59] V. Ivanovs et al. “Temperature stabilization of SiPM based gamma-radiation scintillation detectors”. In: *rad-journal* 3 (2018), pp. 29–32. DOI: doi:10.21175/RadJ.2018.03.028.
- [60] A. Gil et al. “Programmable power supply system for SiPM bias”. In: *2011 IEEE Nuclear Science Symposium Conference Record*. IEEE. 2011, pp. 787–790. DOI: 10.1109/NSSMIC.2011.6154298.
- [61] P. Dorosz et al. “Silicon photomultiplier’s gain stabilization by bias correction for compensation of the temperature fluctuations”. In: *Nuclear Instruments and Methods in Physics Research Section A: Accelerators, Spectrometers, Detectors and Associated Equipment* 718 (2013), pp. 202–204. DOI: 10.1016/j.nima.2012.11.116.
- [62] H. S. Shim, H. Park, and J. S. Lee. “A temperature-dependent gain compensation technique for positron emission tomography detectors based on a silicon photomultiplier”. In: *Physics in Medicine & Biology* 66.20 (2021), p. 205015. DOI: 10.1088/1361-6560/ac2b81.
- [63] A. Ferri et al. “A comprehensive study of temperature stability of Silicon PhotoMultiplier”. In: *Journal of Instrumentation* 9.06 (2014), P06018. DOI: 10.1088/1748-0221/9/06/p06018.
- [64] S. Nieswand. “submitter: A Peltier cooling system for SiPM temperature stabilization”. PhD thesis. RWTH Aachen U., 2012.
- [65] F. Licciulli and C. Marzocca. “An active compensation system for the temperature dependence of SiPM gain”. In: *IEEE Transactions on Nuclear Science* 62.1 (2015), pp. 228–235. DOI: 10.1109/TNS.2015.2388580.
- [66] *Introduction to SiPMs*. URL: https://advansid.com/attachment/get/up_89_1411030571.pdf. (visited on 05/05/2022).
- [67] K. Hamamatsu Photonics. “Electron Tube Division”. In: *R7400U series photomultiplier data sheet* (2005). URL: https://ctf3-tbts.web.cern.ch/instr/pmt/r7400u_tpmh1204e07.pdf.
- [68] W. Spicer and F. Wooten. “Photoemission and photomultipliers”. In: *Proceedings of the IEEE* 51.8 (1963), pp. 1119–1126. DOI: 10.1109/PROC.1963.2447.

- [69] N. Otte. “The silicon photomultiplier—a new device for high energy physics, astroparticle physics, industrial and medical applications”. In: *Proceedings of the IX International Symposium on Detectors for Particle, Astroparticle and Synchrotron Radiation Experiments*. 2006, pp. 1–9. URL: <https://www.semanticscholar.org/paper/The-Silicon-Photomultiplier-A-new-device-for-High-Otte/ec7e503c0ee3ad5c231fa2f4f924bd8f06e5a0c4>.
- [70] K. Deiters et al. “Properties of the most recent avalanche photodiodes for the CMS electromagnetic calorimeter”. In: *Nuclear Instruments and Methods in Physics Research Section A: Accelerators, Spectrometers, Detectors and Associated Equipment* 442.1-3 (2000), pp. 193–197. DOI: [https://doi.org/10.1016/S0168-9002\(99\)01220-6](https://doi.org/10.1016/S0168-9002(99)01220-6).
- [71] J. B. McLaughlin et al. “Characterisation of SiPM photon emission in the dark”. In: *Sensors* 21.17 (2021), p. 5947. DOI: [10.3390/s21175947](https://doi.org/10.3390/s21175947).
- [72] E. Conca et al. “Large-area, fast-gated digital SiPM with integrated TDC for portable and wearable time-domain NIRS”. In: *IEEE Journal of Solid-State Circuits* 55.11 (2020), pp. 3097–3111. DOI: [10.1109/JSSC.2020.3006442](https://doi.org/10.1109/JSSC.2020.3006442).
- [73] F. Nolet et al. “Digital SiPM channel integrated in CMOS 65 nm with 17.5 ps FWHM single photon timing resolution”. In: *Nuclear Instruments and Methods in Physics Research Section A: Accelerators, Spectrometers, Detectors and Associated Equipment* 912 (2018), pp. 29–32. DOI: <https://doi.org/10.1016/j.nima.2017.10.022>.
- [74] C. Piemonte et al. “Characterization of the first FBK high-density cell silicon photomultiplier technology”. In: *IEEE Transactions on Electron Devices* 60.8 (2013), pp. 2567–2573. DOI: [10.1109/TED.2013.2266797](https://doi.org/10.1109/TED.2013.2266797).
- [75] *Introduction to silicon photomultipliers (SiPMs)*. URL: https://www.first-sensor.com/cms/upload/appnotes/AN_SiPM_Introduction_E.pdf. (visited on 12/04/2022).
- [76] E. Garutti. “Silicon photomultipliers for high energy physics detectors”. In: *Journal of Instrumentation* 6.10 (2011), p. C10003. DOI: [10.1088/1748-0221/6/10/c10003](https://doi.org/10.1088/1748-0221/6/10/c10003).

- [77] V. C. Spanoudaki and C. S. Levin. “Photo-detectors for time of flight positron emission tomography (ToF-PET)”. In: *Sensors* 10.11 (2010), pp. 10484–10505. DOI: 10.3390/s101110484.
- [78] *How to Evaluate and Compare Silicon Photomultiplier Sensors*. October 2015. URL: <https://hobbydocbox.com/Radio/72616881-How-to-evaluate-and-compare-silicon-photomultiplier-sensors-october-2015.html>. (visited on 29/04/2022).
- [79] A. Duara. “Characterisation of silicon photomultiplier detectors for their application in very-high-energy astrophysics”. PhD thesis. University of Leicester, 2021. URL: https://leicester.figshare.com/articles/thesis/Characterisation_of_Silicon_Photomultiplier_Detectors_for_their_Application_in_Very-High-Energy_Astrophysics_/17104727.
- [80] A. Vacheret et al. “Characterization and simulation of the response of Multi-Pixel Photon Counters to low light levels”. In: *Nuclear Instruments and Methods in Physics Research Section A: Accelerators, Spectrometers, Detectors and Associated Equipment* 656.1 (2011), pp. 69–83. DOI: <https://doi.org/10.1016/j.nima.2011.07.022>.
- [81] J. J. Csáthy et al. “Development of an anti-Compton veto for HPGe detectors operated in liquid argon using silicon photo-multipliers”. In: *Nuclear Instruments and Methods in Physics Research Section A: Accelerators, Spectrometers, Detectors and Associated Equipment* 654.1 (2011), pp. 225–232. DOI: <https://doi.org/10.1016/j.nima.2011.05.070>.
- [82] H. Chen. “A Silicon Photomultiplier Readout ASIC for the Mu3e Experiment”. PhD thesis. 2018. DOI: 10.11588/heidok.00024727.
- [83] D. McNally and V. Golovin. “Review of solid state photomultiplier developments by CPTA and photonique SA”. In: *Nuclear Instruments and Methods in Physics Research Section A: Accelerators, Spectrometers, Detectors and Associated Equipment* 610.1 (2009), pp. 150–153. DOI: <https://doi.org/10.1016/j.nima.2009.05.140>.
- [84] M. F. L’Annunziata. *Handbook of radioactivity analysis*. Academic press, 2012. ISBN: ISBN: 9780080495057.

- [85] T. J. Aucott et al. “Impact of detector efficiency and energy resolution on gamma-ray background rejection in mobile spectroscopy and imaging systems”. In: *Nuclear Instruments and Methods in Physics Research Section A: Accelerators, Spectrometers, Detectors and Associated Equipment* 789 (2015), pp. 128–133. ISSN: 0168-9002. DOI: <https://doi.org/10.1016/j.nima.2015.04.012>.
- [86] *M.J. Berger, J.S. Coursey, M.A. Zucker, J. Chang, 1974 - NIST standard reference database 124*. URL: <http://dx.doi.org/10.18434/T4NC7P>. (visited on 31/05/2022).
- [87] *POLY-VINYLTOLUENE Product Description*. URL: https://www.chemicalbook.com/ChemicalProductProperty_US_CB1168060.aspx. (visited on 31/05/2022).
- [88] *Homepage Scionix.nl Scionix*. URL: <https://scionix.nl/>. (visited on 18/05/2022).
- [89] *Eljen Technology*. URL: <https://eljentechnology.com/>. (visited on 18/05/2022).
- [90] *BK precision 9174 Dual channel DC Power Supply 0-35V, 3A/35-70V, 1.5A*. URL: <https://www.signaltestinc.com/BK-Precision-9174-Dual-Channel-DC-Power-Supply-p/9174.htm>. (visited on 18/05/2022).
- [91] *3M™ Enhanced Specular Reflector Films*. URL: <https://multimedia.3m.com/mws/media/12450890/3m-enhanced-specular-reflector-films-3m-esr-tech-data-sheet.pdf>. (visited on 31/05/2022).
- [92] C. N. Davids et al. “ β decay of ^{22}F ”. In: *Phys. Rev. C* 9 (1 Jan. 1974), pp. 216–226. DOI: 10.1103/PhysRevC.9.216.
- [93] H. Joukainen, J. Sarén, and P. Ruotsalainen. “Position sensitive plastic scintillator for beta particle detection”. In: *Nuclear Instruments and Methods in Physics Research Section A: Accelerators, Spectrometers, Detectors and Associated Equipment* 1027 (2022), p. 166253. ISSN: 0168-9002. DOI: <https://doi.org/10.1016/j.nima.2021.166253>.
- [94] L. Swiderski et al. “Measurement of Compton edge position in low-Z scintillators”. In: *Radiation Measurements* 45.3 (2010). Proceedings of the 7th European Conference on Luminescent Detectors and Transformers of Ionizing Radiation (LUMDETR 2009), pp. 605–607. ISSN: 1350-4487. DOI: <https://doi.org/10.1016/j.radmeas.2009.10.015>.

- [95] M. J. Safari, F. A. Davani, and H. Afarideh. *Differentiation method for localization of Compton edge in organic scintillation detectors*. 2016. DOI: 10.48550/ARXIV.1610.09185.
- [96] *Laser Range Finding and Imaging LIDAR with Silicon Photomultipliers*. URL: <https://pt.slideshare.net/jcjacks/b-sens-1-iwpc-automotive-lidar-v1p0?ref=>. (visited on 03/05/2022).
- [97] J. Smith. “Nuclear accidents”. In: *Nuclear power and the environment* (2011), p. 57. DOI: [DOIhttps://doi.org/10.1039/9781849732888-00057](https://doi.org/10.1039/9781849732888-00057).
- [98] D. Lochbaum, E. Lyman, S. Q. Stranahan, et al. *Fukushima: The story of a nuclear disaster*. New Press, The, 2014.
- [99] N. Takamura and S. Yamashita. “Lessons from Chernobyl”. In: *Fukushima journal of medical science* 57.2 (2012), pp. 81–85. DOI: <https://doi.org/10.5387/fms.57.81>.
- [100] A. Gektin and M. Korzhik. *Inorganic scintillators for detector systems: Physical Principles and Crystal Engineering*. Springer, 2017. ISBN: 978-3-540-27766-8.
- [101] P. Lindblom and O. Solin. “Atomic near-infrared noble gas scintillations I: Optical spectra”. In: *Nuclear Instruments and Methods in Physics Research Section A: Accelerators, Spectrometers, Detectors and Associated Equipment* 268.1 (1988), pp. 204–208. DOI: [https://doi.org/10.1016/0168-9002\(88\)90607-9](https://doi.org/10.1016/0168-9002(88)90607-9).
- [102] R. Stalter and D. Howarth. *Gamma Radiation*. IntechOpen, 2012. DOI: <https://doi.org/10.5772/34856>.
- [103] X. Li et al. “Energy calibration for plastic scintillation detectors based on Compton scatterings of gamma rays”. In: *Journal of Instrumentation* 12.12 (2017), pp. 12025–12025. DOI: 10.1088/1748-0221/12/12/p12025.
- [104] *Introduction to the Silicon Photomultiplier (SiPM)*. URL: <https://www.onsemi.com/pub/Collateral/AND9770-D.PDF>. (visited on 13/04/2022).
- [105] *Introduction to SiPM technology*. URL: <https://www.aptechnologies.co.uk/support/SiPMs/intro>. (visited on 29/04/2022).

- [106] C. Niclass, M. Sergio, and E. Charbon. “A single photon avalanche diode array fabricated in deep-submicron CMOS technology”. In: *Proceedings of the Design Automation & Test in Europe Conference*. Vol. 1. IEEE, 2006, pp. 1–6. DOI: 10.1109/DATE.2006.243987.
- [107] *The SiPM Physics and Technology - a Review*. URL: https://indico.cern.ch/event/164917/contributions/1417121/attachments/198512/278663/PhotoDet12_-_collazuol_-_v3.pdf. (visited on 29/04/2022).
- [108] V. P. Ghouschi. “Opto-Mechanical Design And Development of an Optodigital Confocal Microscope”. PhD thesis. Koç University, 2015. DOI: 10.13140/RG.2.2.33261.38884.
- [109] L. M. Ganea, A. I. Apostol, and A. Pantelica. “Non-destructive analysis of pure-beta emitters: applications in nuclear forensics”. In: *Journal of Radioanalytical and Nuclear Chemistry* 322.3 (2019), pp. 1641–1644. DOI: 10.1007/s10967-019-06814-0.
- [110] M. N. Wernick and J. N. Aarsvold. *Emission tomography: the fundamentals of PET and SPECT*. Elsevier, 2004, pp. 229–254. ISBN: 9780080521879.

A First appendix

Table 8. Some of the primary fluor used in plastic scintillators [18]

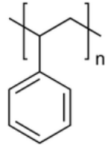
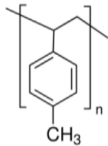
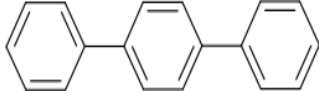
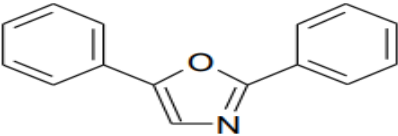
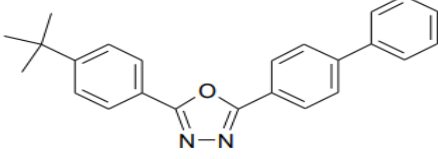
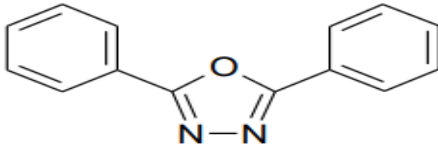
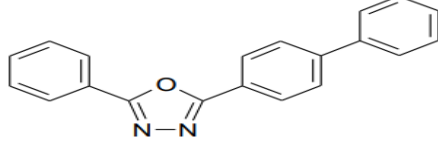
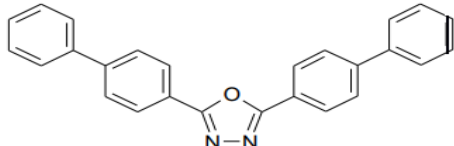
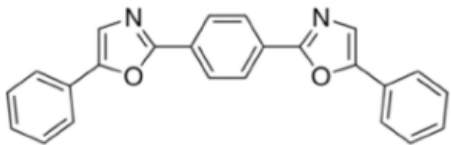
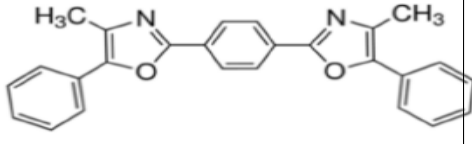
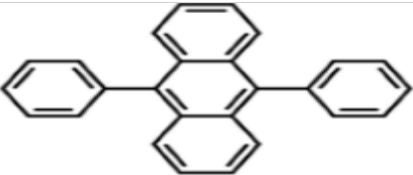
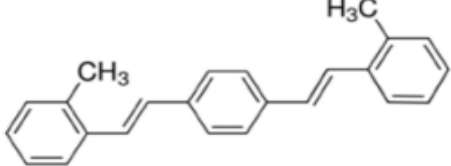
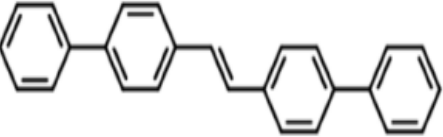
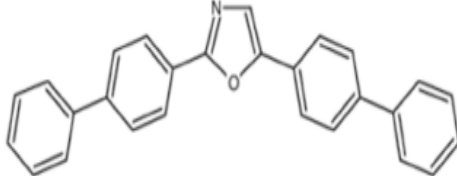
Name	Abbreviation	Chemical structure
Polystyrene	PS	
Polyvinyl toluene	PVT	
P-terphenyl	PTP	
2,5 - diphenyloxazole	PPO	
2-(4-tert-butylphenyl)-5-(4-biphenyl)-1,3,4-oxadiazole	BPBD	
2,5-diphenyl-1,3,4-oxadiazole	PPD	
2-phenyl-5(4-biphenyl)-1,3,4-oxadiazole	PBD	
2,5-bis(4-biphenyl)-1,3,4-oxadiazole	BBD	

Table 9. Commonly used wavelength shifter in plastic scintillator [18]

Name	Abbreviation	Chemical structure
1,4-bis(5-phenyl-2-oxazolyl)benzene	POPOP	
1,4-bis(4-methyl-5-phenyl-2-oxazolyl)benzene	DM-POPOP	
9,10-diphenylanthracene	DPA	
1,4-bis(2-methylstyryl)benzene	Bis-MSB	
Trans-4,4'-diphenylstilbene	DPS	
2,5-di(4-phenylo)oxazole	BBO	

B Second appendix

Maximum β particle range in EJ-200 plastic scintillator

$$\begin{aligned} \text{For, } E_\beta &= 0.546 \text{ MeV ; } \rho = 1.023 \text{ g/cm}^2 \\ R_{max} [g/cm^2] &= 0.412 E_\beta^{1.265-0.0954 \cdot \ln(E_\beta)} \\ R_{max} [g/cm^2] &= 0.412(0.546)^{1.265-0.0954 \cdot \ln(0.546)} = 0.1845 \text{ g/cm}^2 \\ t = \frac{R_{max}}{\rho} &= \frac{0.1845 \text{ g/cm}^2}{1.023 \text{ g/cm}^2} = 0.1804 \text{ cm} = 1.804 \text{ mm} \end{aligned}$$

$$\begin{aligned} \text{For, } E_\beta &= 2.28 \text{ MeV ; } \rho = 1.023 \text{ g/cm}^2 \\ R_{max} [g/cm^2] &= 0.412 E_\beta^{1.265-0.0954 \cdot \ln(E_\beta)} \\ R_{max} [g/cm^2] &= 0.412(2.28)^{1.265-0.0954 \cdot \ln(2.28)} = 1.0953 \text{ g/cm}^2 \\ t = \frac{R_{max}}{\rho} &= \frac{1.0953 \text{ g/cm}^2}{1.023 \text{ g/cm}^2} = 1.07067 \text{ cm} = 10.707 \text{ mm} \end{aligned}$$

C Third appendix

Table 10. Properties comparison between photomultiplier tube (PMT) and silicon photomultiplier (SiPM) [96]

Properties	Photomultiplier Tube (PMT)	Silicon Photomultiplier (SiPM)
Sensitivity	Single photon	Single photon
Gain	$\sim (10^5 - 10^7)$	$\sim (10^5 - 10^6)$
Operating voltage	800V - 2000V	30V - 100V
Temperature sensitivity	Low	Medium
Mechanical Robustness	Low	High
Damage by stray light	Yes	No
Spectral range	Blue/UV	UV - VIS - NIR
Form factor	Bulky	Small
Photon-counting resolution	Good	Excellent
Response time	Fast	Fastest
Uniformity	Good	Excellent
Dark noise	Low	Middle
Immune to ambient light	No	Yes
Immune to magnetic field	No	Yes
Compact and lightweight	No	Yes
System cost	High	Lowest
Scalable technology	No	Yes

D Fourth appendix

List of abbreviations

DNA = Deoxyribonucleic acid
PMT = Photomultiplier tubes
SiPM = Silicon photomultiplier
ZnS = Zinc sulphide
DAQ = Data Acquisition
NaI = Sodium Iodide
ZnO = Zinc oxide
PVT = Polyvinyl Toluene
APD = Avalanche Photodiode
SPAD = Single photon avalanche photodiode
GM-APD = Geiger-mode avalanche photodiode
SSPM = Solid-state photomultiplier
MPPC = Multipixel photon counter
MPAD = Multipixel avalanche photodiode
QE = Quantum efficiency
PDE = Photon detection efficiency
DCR = Dark count rate
FWHM = Full width at half maximum
JYFL = Jyväskylän Yliopiston Fysiikan Laitos
LCD = Liquid crystal display
PMMA = Polymethyl methacrylate